UC Berkeley
UC Berkeley Electronic Theses and Dissertations

Title
Challenges on Decarbonization of Electric Power Systems

Permalink
https://escholarship.org/uc/item/52s2h0sv

Author
Henriquez Auba, Rodrigo Marti

Publication Date
2022

Peer reviewed|Thesis/dissertation

Challenges on Decarbonization of Electric Power Systems

by

Rodrigo Marti Henriquez Auba

A dissertation submitted in partial satisfaction of the

requirements for the degree of

Doctor of Philosophy

in

Engineering – Electrical Engineering and Computer Sciences

in the

Graduate Division

of the

University of California, Berkeley

Committee in charge:

Professor Duncan S. Callaway, Co-chair
Professor Kameshwar Poolla, Co-chair
Professor Robert Pilawa-Podgurski

Fall 2022

Challenges on Decarbonization of Electric Power Systems

Abstract

Challenges on Decarbonization of Electric Power Systems

by

Rodrigo Marti Henriquez Auba

Doctor of Philosophy in Engineering – Electrical Engineering and Computer Sciences

University of California, Berkeley

Professor Duncan S. Callaway, Co-chair

Professor Kameshwar Poolla, Co-chair

Electric power systems are one of the fundamental pillars of modern society. Power systems require careful planning to ensure enough capacity for future electric demand, and simultaneously requiring meticulous operation to maintain a continuous supply-demand balance, which ensures a reliable and stable system. In this complex context, our electric systems are being decarbonized, moving away from fossil fuel based systems into more renewable ones, with larger contribution from wind and solar energy sources, reducing emissions of greenhouse gases which negatively contribute to climate change.

The consequences of this transition to renewable systems are multi-fold. First, renewable sources, like wind and solar, are variable and face uncertainty that complicates future planning of these energy systems. Second, the integration of Distributed Energy Resources (DERs), like rooftop photovoltaic systems, changes the paradigm of how our electric system operates, where power was once only generated in large generating units, and delivered via high-voltage transmission lines to the demand hubs—commonly large cities. Traditional energy sources, such as coal or gas, inject power via synchronous generators, however renewable resources are mostly interfaced into the grid using power electronics, that creates a fundamental difference in how electricity is produced. All of these changes are affecting our understanding of the grid, in multiple aspects and with different problems, which force us to reevaluate the tools and techniques used to study power systems.

This work focus on understanding the different challenges that are occurring in power systems due to the integration of variable Renewable Energy Sources (RESs), both in planning studies and day-to-day system operation. Thus, the main goal of this thesis is to study and analyze the changes in power systems with increasing shares of RESs, across multiple time- and space- scales.

The first part of this dissertation investigates dynamic simulations that are necessary for analyzing power system stability and dynamic response in the presence of Inverter-based Resources (IBRs). We introduce the Julia package `PowerSimulationDynamics.jl` to study the effects of load and line modeling when grid-forming and grid-following inverters. A dis-

cussion is presented between phasor-type and electromagnetic transient-type simulations. Results confirm that rooted assumptions in transient simulations may not be valid in systems with large presence of IBRs. By enabling `PowerSimulationDynamics.jl` as a flexible software tool, we discover that more detailed network and load models are becoming more necessary to properly assess stability of future power systems, as the integration of IBRs increases.

The second part focuses on DERs investment in peer-to-peer and sharing economy setups. In particular, we propose an optimization model for distributed rooftop Photovoltaic (PV) investment to analyze how PV investment decisions can vary when consumers are subjected to different tariff schemes. Our results showcase how peer-to-peer tariff schemes, rather than traditional net-metering or feed-in-tariffs, can promote investment in rooftop PV.

Finally, the third part of this dissertation discuss the Switch expansion planning model, and specifically the effects of Electric Vehicles (EVs) flexibility in the future Western Electricity Coordinating Council (WECC) grid. Motivated by future decarbonization scenarios in California, we added a new EV module to the Switch model to study the influence of EV flexibility in installed capacity in WECC by 2050. Our results confirms that demand flexibility can reduce system's peak load to defer large investment decisions, achieving savings in both planning and operation costs.

To Gabriela Bravo-Illanes, my brother, my parents and my friends.

Contents

List of Figures

List of Tables

List of Source Code

List of Acronyms

AD Automatic Differentiation
AVR Automatic Voltage Regulator
BEAM Behavior, Energy, Autonomy, and Mobility
CPL Constant Power Load
CCL Constant Current Load
CIL Constant Impedance Load
CCL Constant Current Load
CIL Constant Impedance Load
DAE Differential Algebraic Equation
DER Distributed Energy Resource
DR Demand Response
DG Distributed Generation
dVOC dispatchable Virtual Oscillator Control
EIA Environmental Information Agency
EMT Electro-magnetic Transient
EV Electric Vehicle
FACTS Flexible AC Transmission System
FERC Federal Energy Regulatory Commission
FFR Fast-Frequency Response
GFM Grid-Forming
GFL Grid-Following
HVDC High-Voltage Direct Current
IBR Inverter-based Resource
IPCC Intergovernmental Panel on Climate Change
IM Induction Machine
JIT Just-in-Time
LDV Light Duty Electric Vehicle
LLVM Low-Level Virtual Machine
LTI Linear Time Invariant
NREL National Renewable Energy Laboratory
ODE Ordinary Differential Equation
PV Photovoltaic

RES Renewable Energy Source
RoCoF Rate of Change of Frequency
PEV Plug-in Electric Vehicle
PLL Phase-locked Loop
PWM Pulse-Width Modulation
QSP Quasi-Static Phasor
SCR Short Circuit Ratio
SPT Singular Perturbation Theory
SIB Singularity-Induced Bifurcation
SM Synchronous Machine
SPT Singular Perturbation Theory
SRF Synchronous Reference Frame
VSC Voltage Source Converter
VSM Virtual Synchronous Machine
WT Wind Turbine
WECC Western Electricity Coordinating Council

Acknowledgments

Chapter 1

Introduction

1.1 Background and Motivation

It is well known that climate change is having an impact the way we live. Many impacts, such as biodiversity loss [49, 11], food availability [138], wildfire risk [121], water availability [1], increase in global temperature [81], among others, are happening and will continue to worsen if we do not take actions to tackle climate change. In 2015, the 21st Session of the Conference of the Parties of the United Nations Framework Convention on Climate Change (COP 21) took place in Paris, confirming efforts to limit global temperature increase to below 2°C as discussed in the Intergovernmental Panel on Climate Change (IPCC) in 2007 [119, 3]. It even went further, urging countries to increase their efforts to limit the increase to 1.5°C.

In this aspect, decarbonizing our electric system is a fundamental effort to achieve our climate goals. We have seen, since the early 2000s, an increase in the adoption of RES in different power systems across the world. Starting as pilot technologies, technological advances in PV panels and Wind Turbines (WTs) have made renewable energy an economically viable way to generate electric power. One of the fundamental goals for our society to tackle climate change is to achieve a decouple electricity generation from CO2 emissions. This is something that is already in progress, as depicted in Figure 1.1. From an economical perspective, RES are able to compete with fossil fuels. However, the crucial challenge is integrating these renewable sources into a power system that is not built and designed to adapt to the changes that RES are imposing on our grid. In the next paragraphs we describe these challenges.

The RESs integration challenges are happening in multiple space- and time-scales, and are changing our understanding of how a power system has to be planned and operated. Historically, power systems were designed to operate using controllable thermal generation, with only minor variability due to load demand in the short term [123]. However, the inherent variability of RES affects the techniques used to model, operate and plan future power systems in both technical and economic aspects. And, although curtailment or
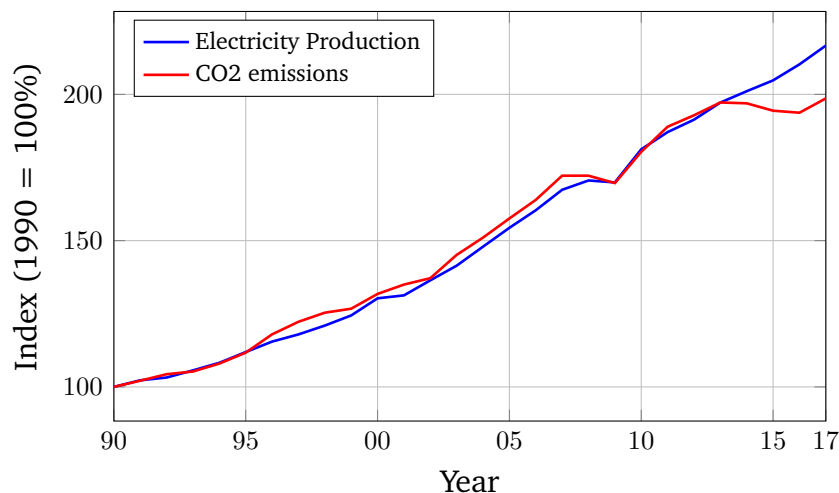
Figure 1.1: Observed decoupling of global electricity production with CO2 emissions.

energy storage can be used to address short-time variability and intermittency, it is still an expensive solution for most grids. In addition, solar PV, WTs and energy storage are changing the underlying physics of how we operate power grids. We are moving from systems powered by fuel-based resources interfaced with Synchronous Machines (SMs) to power electronics-based electric systems. These IBRs power electronics-based resources do not commonly provide the same level of grid support, such as frequency or voltage regulation, that is typically provided by SMs.

Thus, it becomes fundamental to figure out which technical and economic approaches are still valid due to the integration of RESs. To study and analyze power systems we rely on a set of tools and techniques that allow us to understand what will happen in the future and how our power system will behave under changing conditions. These tools differ depending on what types of phenomena or problems we want to study. Essentially, tools and techniques that we commonly rely on to study power systems may not work in this new scenario that we are facing. For example, we used to run a system expansion planning study using traditional optimization models with load duration curves. But, with the inclusion of renewables and storage in the grid, this approach was not suitable, so we moved to the use of representative days in an attempt to capture these new operational effects in our planning models. As a result, optimization problems become more computationally complex [108].

Figure 1.2 summarizes the different tools and techniques used to study multiple phenomena in power systems depending on the specific timescale. How these change depends on multiple aspects. In operational tools, such as economic dispatch or unit commitment, we need stochastic or robust optimization to deal with the uncertainty of renewables [75]. We may need to run these problems with more granularity, because intertemporal issues that are not commonly captured are creating issues [107]. Similar issues arise in dynamic

Decision criteria	Technical		Technical-Economical			Policy
Time Scale	Less than 1s	Seconds	Seconds to Minutes	Minutes to hours	Days to one year	Years to decades

Phenomena or problem	Lightning propagation	Voltage and frequency regulation		Generation Dispatch		T&G planning
	Switching studies	Voltage stability		Reserves management	Integration of generation resources	
	Stator transients and subsynchronous resonance		Automatic Generation Control		Hydro Storage Management Maintenance Scheduling	
		Transient stability and contingency studies Governor and load frequency control				

Tools to use	Waveform Simulations (EMTP)	Transient Simulation (RMS)		Economic Dispatch, Optimal Power Flow and Unit Commitment		Planning models
		$dq0$ modeling	Quasi-Dynamic Simulations		Investment decision models	

Figure 1.2: Power system analysis tools and phenomena at different timescales. Phenomena studied in this dissertation is highlighted in magenta, and tools used in cyan.

analyses and transient stability studies. Inverters have significantly faster dynamics than synchronous machines, which are the backbone of our power system. Naively incorporating these models in existing tools may not work, since our solution methods may fail, or may not provide accurate results with respect to what we are observing in reality [36, 43]. It is important to note that the techniques and tools used to study and analyze these issues can be completely different depending on the specific problem being studied. In this sense, the approach to understanding a specific phenomenon occurring in power systems can vary significantly, although the root cause, such as the integration of RESs, is the same. The fundamental challenges can be classified by time scope as follows:

- **Seconds:** In this time scope, the key changes are related to new physics and dynamics, due to the integration of power electronics. In particular, as electric grids replace synchronous generators with inverters, the system's inertia decreases making it more variable over time, which can challenge frequency stability under current control implementations [131]. In addition, these resources have faster dynamics that can interact with existing infrastructure, creating new stability problems that will require additional approaches to tackle them [40]. Figure 1.3 highlights the wide range of time-scales of inverter-based controls.

- **Minutes to hours:** One of the critical tasks in this time scope relates to the optimal dispatch of generation, in an hourly or sub-hourly resolution, while satisfying the demand, with sufficient reliability, at a minimum cost. In the past, there was only a small degree of uncertainty in estimating future demand, but it was not critical given that fuel-based generation was sufficient to address such changes. However, with
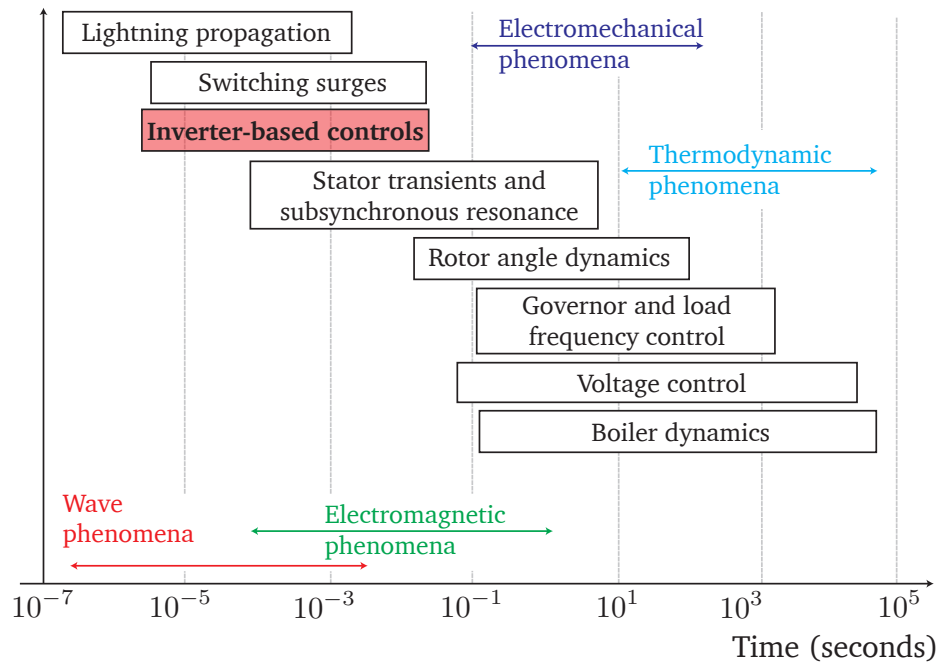
Figure 1.3: Time scales for power systems dynamic behaviour. Figure adapted from [40].

the integration of RESs, generation is not necessarily controllable, and their power injection will have underlying uncertainty given the availability of the renewable resource (typically wind or solar). This new probabilistic scenario, with the non-convexity associated with power flow equations [88] and discrete behavior of turning on and off devices [59], requires advanced mathematical approaches to tackle these challenges.

- **Years to decades:** Crucial challenges in integrating RESs relate to properly capturing the variability in a power system capacity expansion optimization problem [41, 35]. Optimizing how the transmission and generation will expand while capturing the availability and variability of renewable resources is a highly complex problem. Furthermore, with the unexpected changes due to climate change, the necessary input data for grid expansion, such as future scenarios of water availability, wind speeds, solar irradiance, fuel prices, and demand growth, among others, may not be reliable, requiring analysis of an increasing amount of study cases to handle such challenges.

The goal of this dissertation is to explore and improve different aspects of power system analyses in the process of decarbonizing our electric grids. In the first part of the thesis, we look at how to improve the modeling and interactions between SMs and IBRs, and how the integration of these new renewable sources is affecting the stability and reliability of future power systems. There is a significant focus on how GFM technologies, and their

system-level control, can affect and enhance grid stability. In the second part, different market structures are studied to understand their effect on the investment of distributed PV. Finally, the third part presents how demand flexibility can be incorporated in long-term expansion planning models, and its effects in a study case for California in 2050.

1.2 Contributions

This dissertation is focused on exploring multiple power system aspects that are changing, in the process of system decarbonization, by integrating more RES. Specifically, the main contributions of this thesis are:

- In Section 2.1 we present a summary of GFM technologies and their importance in future power system reliability. In particular, we focus on how mathematical modeling and model order reduction can be used to study power system stability.

- In Section 2.2 we review scientific computing aspects and their relation to power system dynamic simulations. We present our development of the Julia package `PowerSimulationsDynamics.jl` in Section 2.3 to address part of these aspects.

- We demonstrate that AC-side dynamics approximations can significantly alter regions of small signal stability for GFM inverter models. In particular, in Section 2.4, we examine how model order reduction affects GFM parameter tuning.

- We examine how different load models affect small signal stability of both SMs and GFM inverters. Specifically, in Section 2.5, we analyze zones of small-signal stability in Power-Voltage (nose) curves across different GFM models and load models.

- Additionally, in Section 2.5 we also analyze the type of bifurcations observed by increasing load demand across multiple load models and GFM and SM models.

- In Section 3.1 we present a solar investment decision optimization problem under various pricing and market schemes, that considers uncertainty arising from behind-the-meter energy consumption and solar production.

- We show that solar investment decisions in a peer-to-peer sharing economy model can be cast as a game that admits a unique, social welfare supporting, Nash equilibrium. In particular, in Section 3.3, we provide a convergent algorithm to compute this Nash equilibrium.

- In Section 3.5 we present a thorough analysis of different numerical simulations, using real data on load profiles and solar irradiance, that showcase the main drivers of rooftop PV investment, such as cost, retail prices, electric consumption, and solar production.

- We present a review of the computational trade-offs in expansion planning models in Chapter 4. In Section 4.1 we introduce the Switch Power System Planning model and its core modularity to address which relevant aspects will be considered depending on the specific study case.

- In Section 4.2 we implement two new DR and EV modules in the Switch model to capture its flexibility in expansion planning studies.

- Finally, in Section 4.3 we analyze the value of DR and EV flexibility in a future WECC and California 2050 scenario by using the Switch model.

1.3 Thesis Outline

The thesis is organized into three parts:

1. The first part, **Chapter 2**, focuses on dynamic modeling, stability, and control in IBRs dominated power systems. The chapter presents computational aspects related to time domain simulation and how such simulations are used to analyze power system dynamic behavior. The thin line between modeling and simulations is explored for IBRs, line and load models. The effects on small signal stability are investigated and simulations showcase how dynamic behavior can alter significantly depending on the detail of models used.

2. The second part, **Chapter 3**, focuses on optimization models for rooftop PV investment. In particular, we emphasize how market structures, such as standalone models or peer-to-peer structures, can significantly affect private decisions. Results showcase how some standalone customers will over-invest and others will under-invest, relative to social-welfare maximizing decisions.

3. The third part, **Chapter 4**, presents an implementation of load shifting and electric vehicle flexibility in future expansion planning models for power systems. In particular, we leverage the Switch Power System Planning Model to study how this flexibility can be used in a study of low-carbon energy scenarios for California and WECC in 2050.

Finally, **Chapter 5** summarizes the main findings of this dissertation and discusses directions for future work.

Chapter 2

Effects of Inverter-Based Resources in Dynamic Power Systems Simulations

Current trends in energy systems point to renewable energy sources (RES) and battery energy storage systems (BESS) becoming prevalent in power system operations. As of this writing, the U.S. has over 60 GW of utility-scale solar capacity and an additional 130 GW of wind power [130]. With the rapidly declining capital costs of many of these technologies, we can expect significant deployment in the coming years.

The change in the primary energy supply mix is not the only large-scale shift happening in power systems. Integrating massive numbers of generators interfaced through power electronics is also updating our basic understanding of system stability and control. One example of such advancement is the displacement of traditional rotating generation, which reduces system inertia. This results in higher rates of change of frequency (ROCOF), a lower frequency nadir following disturbances, and complex interactions between dynamics of power electronics converters and other power systems components [131].

Over many decades the power system community has developed standards to model and study synchronous machines and controls. These standards include IEEE 1110 and IEEE 421, which provide guidelines for the modeling practices required to adequately assess system stability and performance [50, 51]. But the introduction of RES and BESS renders the study of these relationships more challenging because many of the assumptions, upon which existing standards are based, may no longer be valid [86, 78]. Indeed, it is agreed that new dynamics associated with IBRs are changing the modeling requirements for time-domain simulations for system studies [102, 40].

Due to the complexity and scale of power system analysis, researchers rely on computational tools and simulations to explore and understand new phenomena that might emerge in future systems characterized by widespread RES and BESS. Indeed, determining the level of modeling details to properly capture phenomena of interest is a crucial challenge in future power system time-domain simulations. In 2021, U.S. National Academy of Sciences recognized the importance of understanding how the grid of the future will behave, and how operators and policy makers can ensure its continued reliability [93]. The
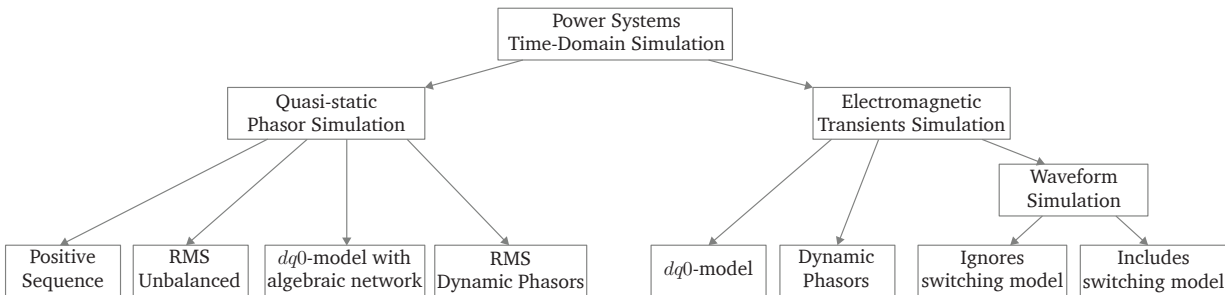
Figure 2.1: Taxonomy of power systems time-domain simulation models [68].

capacity to do this rests on improving the simulation capabilities necessary to build and
test the integration of new devices and components with different levels of assumptions
and complexity.

In addition, depending on the assumptions used to model devices and networks, their
mathematical algorithms to numerically integrate the system and interface multiple devices
can be significantly different. Thus, a simulation taxonomy was proposed in [68], in order
to classify time-domain simulations. Figure 2.1 presents such classification in roughly
two groups: 1) *QSP Simulations* in which the transmission system circuits dynamics are
represented algebraically as discrete changes between steady-state operating points, and 2)
EMT Simulations, which include sufficient detail to capture fast dynamic phenomena. QSPs
are used for the study of low-frequency phenomena that range from inertial response to
frequency regulation. On the other hand, EMT simulations are used in settings where one
wishes to capture the impact of line dynamics, converter switching, machine fluxes, and/or
lightning surges. In particular, we will analyze the effects on stability of considering circuit
dynamics in IBRs stability. In specific, the main contributions of this chapter are:

- A review of GFM and GFL technology to highlight their importance in future power
  systems' operations. Their control structure and fundamental characteristics will be
  presented in relevance to system level performance.

- A review and analysis of how scientific computing aspects can be leveraged for power
  system time-domain simulations. The Julia package `PowerSimulationsDynamics.jl`
  will be introduced to capture these aspects.

- An analysis of how AC-side dynamics of voltage and network can modify regions of
  stability of GFM inverter technology.

- An examination of how load models play a crucial role in understanding stability
  and performance of GFM inverter models. This will include a bifurcation analysis on
  different generation sources and load models.

The aim of this chapter is to study the different aspects and consequences of IBR integration in power systems.

First, in Section 2.1 we present a review of IBRs technology, with a focus on how GFM inverter technology can be important to push our electric systems to a 100% share of renewable energy. Second, Section 2.2 discusses scientific computing aspects related to time-domain simulations. The objective is to highlight how modern computational approaches can be used to develop power system simulations to assess dynamic performance and stability of future power grids with IBRs and SMs. Third, in Section 2.3, we introduce a new modeling platform, `PowerSimulationsDynamics.jl` (PSID.jl) based on the Julia computing language. A study case is presented to highlight how the flexibility of the package can provide insights on the stability of systems with IBRs. Fourth, Section 2.4 presents a study case on how the voltage and line dynamics of the network can influence the stability regions of GFM inverters. We extend the analysis in Section 2.5 to the importance of load dynamics for assessing inverter stability. Finally, section 2.6 presents the conclusions and provides directions of future work.

2.1 Review of Grid Forming and Grid Following Inverter Technology

The transition away from synchronous generators is accompanied by a general trend in the migration of IBRs from those which synchronized and followed the grid GFL to more advance variants that support a range of essential grid services: a technology now commonly known as GFM. Put simply, GFL IBRs *follow* an external grid and perform poorly (if at all) in the absence of stiff voltages; on the other hand, GFM IBRs hold the potential to innately *form* grids.

In [114] it is established that GFM is a converter control strategy that can represent the device as a voltage source with low series impedance, while a Grid Following (GFL) converter can be approximated via a representation of a current source with high parallel impedance. The key emphasis of these representations is that GFL converters achieve the goal of power injection via the control of injected currents, while GFM converters achieve the same goal by controlling directly the voltage at its output terminals [115]. This is showcased in Figure 2.2.

In most applications, GFL converters have their frequency and phase imposed by a stiff AC grid. The network frequency and angle are obtained via a PLL, which locks them on the existing grid to inject the specified active and reactive power. On the other hand, GFM converters can operate in a non-stiff grid or in a grid with complete absence of synchronous generators, and do not require the PLL to operate (although it may still have one for ancillary services, or even synchronization, purposes) [124].

Under steady-state conditions, both GFM and GFL, converters control active and reactive power injection while respecting the limits of internal converter operation. Also, both con-
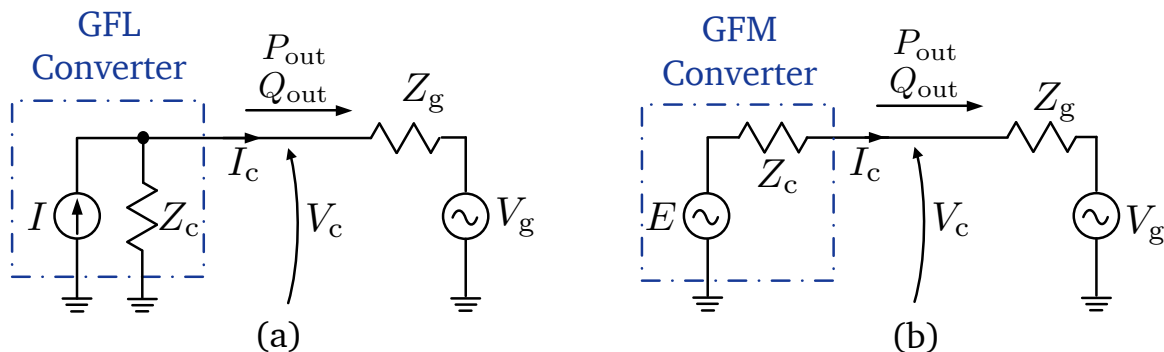
Figure 2.2: (a) GFL inverter representation as a current source. (b) GFM inverter representation as a voltage source. Figure adapted from [115].

verters can provide voltage and/or frequency regulation by using additional outer control layers. The fundamental differences between the converters lie in the dynamical reaction to a grid event and their small-signal behavior under weak or stiff grid conditions [115]. When a disturbance occurs that modifies the grid voltage, in a transient time frame, a GFL converter will attempt maintain the current phasor (or active and reactive power) and the converter voltage phasor will respond accordingly to keep that current. On the other hand, a GFM converter will maintain the voltage phasor, and the converter current will respond accordingly. This latter response is superior to the GFL converters, but depending on the magnitude of the disturbance, it can cause a large increase of the converter currents, jeopardizing converter hardware, which will likely require to add additional current limiting layers for disturbance operation. Both of these behaviors are depicted in Figure 2.3 when a change in the voltage grid V_g occurs. It is important to note that the interpretation of GFM control via voltage-phasor manipulation is indeed true only for slower time scales. For time scales faster than control bandwidths, it is worth noting that both GFL and GFM inverters (that employ voltage-source topologies and Pulse-Width Modulation (PWM)) can be modeled as voltage sources [133]. The presence of inverter's primary-control loops to explicitly govern the dynamics of voltage and frequency (or phase) such that the inverter is able to generate a voltage signal at its output, even in the absence of external grid voltage or load, marks a key distinction between GFL and GFM.

Indeed, while a majority of IBR installations across scales today are of the GFL type, there is a growing consensus around the need to transition future IBR technology to GFM to ensure grid reliability, stability, and resilience [115, 90, 133, 73, 134]. An underpinning feature of GFM IBRs—the ability to operate without external forcing voltage—is a longstanding attribute of standalone inverters meant for islanded small-footprint microgrids and mission-critical backup-power applications. Such standalone inverters, however, were neither designed nor intended to operate in parallel with other independent inverters or power sources. Consequently, these technologies could not be readily deployed in

(a) GFL converter   (b) GFM converter
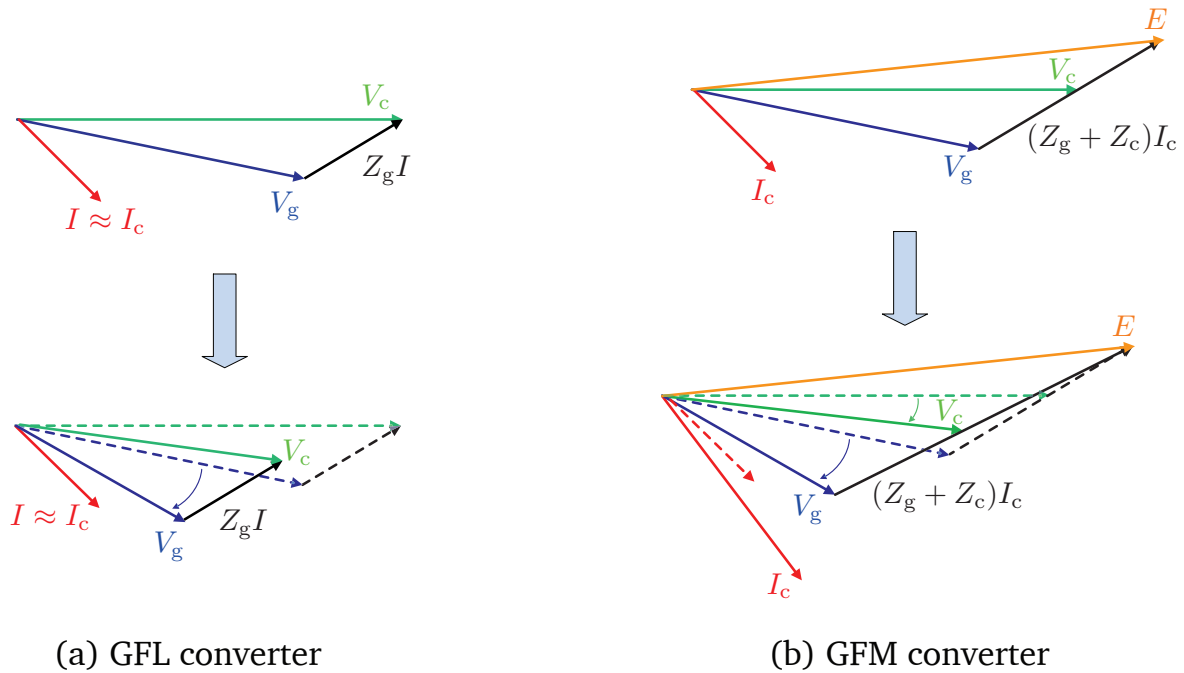
Figure 2.3: Phasor behavior under a voltage grid V_g change. Figure adapted from [115].

bulk power systems that are subjected to a variety of operating conditions and oftentimes require additional grid services. The GFM paradigm, as understood today, applies to grid-interfaced applications, micro and bulk grids; inverters are anticipated to synchronize and interoperate with several other power sources.

Control structures of GFL converters

Although there exists a myriad of control structures for achieving the injection of AC power via power electronics, Figure 2.4 presents a high-level control structure for achieving the aforementioned objective (for both GFL and GFM converters). The system level controls ensure a desired system response, such as ensuring power output and/or achieving system synchronization, while device level controls ensure that the inverter is generating the proper commands to open/close the transistor switches that achieve the desired system level response. Although there are multiple configurations for how to achieve a desired system response, Figure 2.5 provides a summary of the fundamental blocks for a GFL converter that are described next.
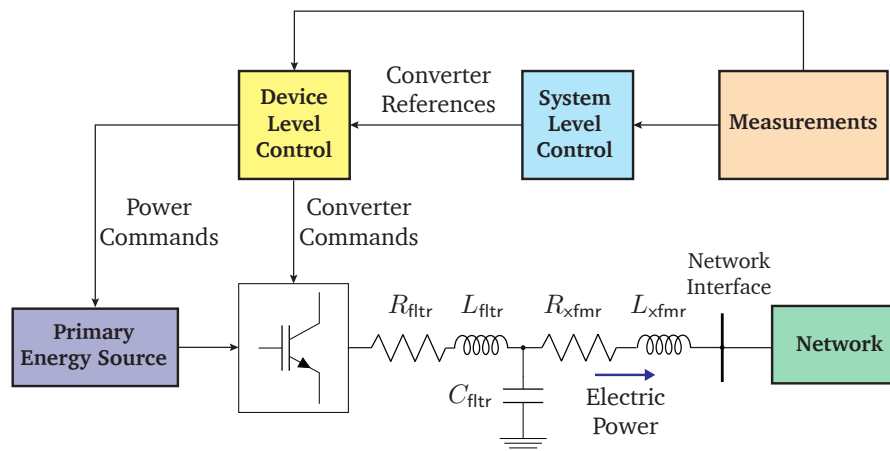
Figure 2.4: Simplified converter control block implementation [68].
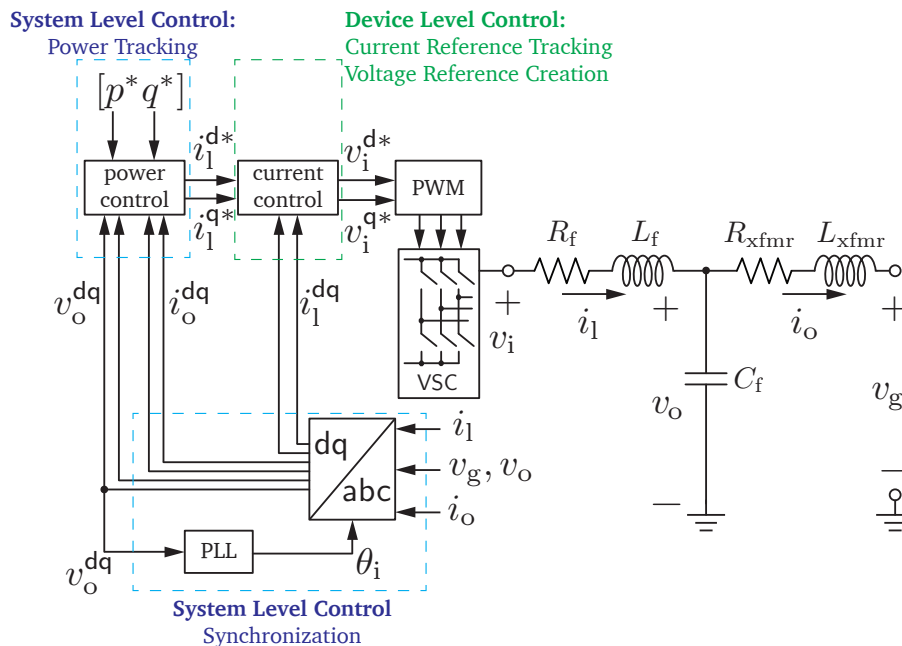
Figure 2.5: Typical GFL converter control block implementation. Figure adapted from [74].

System-Level Synchronization

Most GFL converters connected to the grid achieve synchronization via a PLL using the
network voltage. In Figure 2.5 this is done using the capacitor voltage v_o^{dq} to generate
the angle θ_i. One of the most common implementations, the so-called type-2 SRF PLL,
achieves synchronization by steering the q-axis of the voltage to zero, and hence aligns the

d-axis with the capacitor voltage v_o^d. This block, with an additional low-pass filter for the
measurement of the q-axis (also known as Lag-PLL) of the voltage is presented in Figure
2.6.
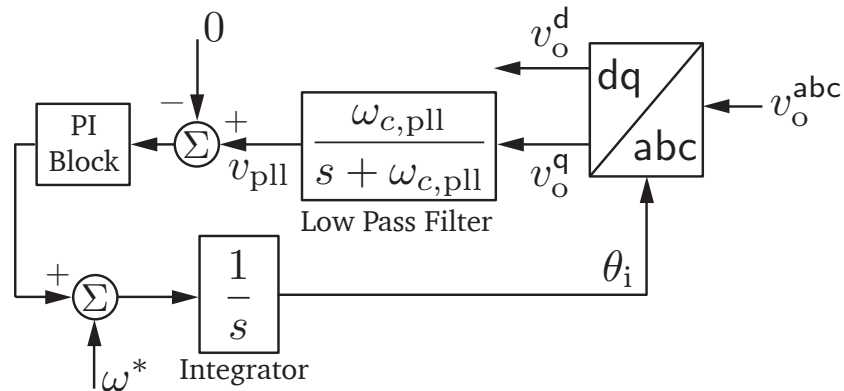
Figure 2.6: Type-2 SRF PLL (Lag-PLL) block diagram.

A detailed discussion of different PLL implementations in simulation studies is presented
in [101].

System-Level Control: Power Tracking

Most system level control for GFL converters tracks active and reactive power references to
generate the current references to the device level control. A common implementation of
such controllers is presented in Figure 2.7:
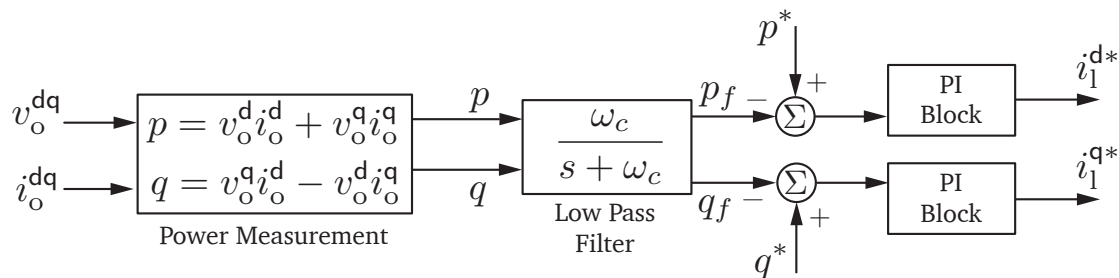
Figure 2.7: Typical system-level power control block diagram.

Here, filtered measurements of active and reactive power are compared and tracked
using PI controllers against reference set-points. The generated current set-points are then
fed into the device-level controller. Grid support can be added to this model by adding
p-ω droop to the active power and adding q-v droop to the reactive power measurements.

Simpler power tracking methods to generate current references can be directly obtained by
dividing by the voltage, as presented in [114]:

$$i_1^{\mathsf{d}*} = \frac{p^*}{v_o^{\mathsf{d}}}, \qquad i_1^{\mathsf{q}*} = \frac{q^*}{v_o^{\mathsf{d}}} \qquad (2.1)$$

that assumes perfect tracking since $v_o^{\mathsf{q}} = 0$.

Device Level Control: Current Controller

The current controller attempts to track the converter current i_1 to the reference provided by
the system-level control. To achieve this a PI control block is used. In addition, decoupling
terms are included due to the coupling effect in a dq-framework. This is depicted in Figure
2.8.
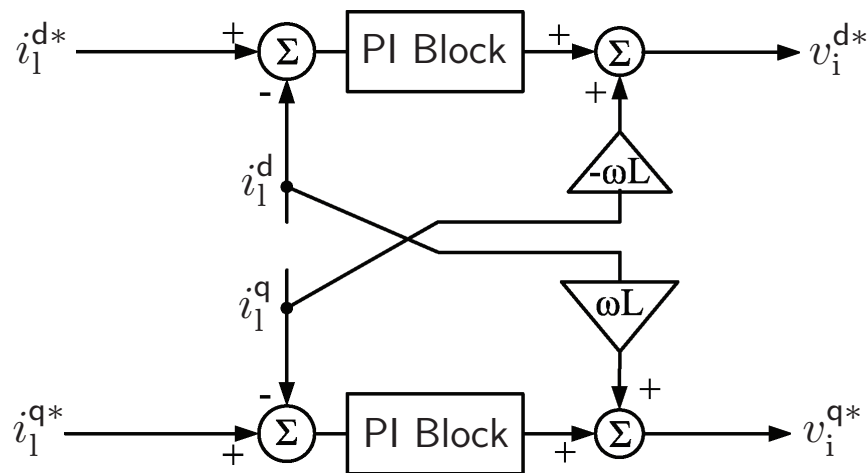
Figure 2.8: Typical device-level current controller block diagram.

Additional feed-forward and active damping terms can be included to generate the
voltage reference that is used for PWM switching.

Modulation Aspects and Average Model

Once there is a reference signal for generating the sinusoidal voltage waveform in the dq
reference frame, this is transformed into the network abc reference frame by using the PLL
angle. These reference signals $v_i^{a*}, v_i^{b*}, v_i^{c*}$ are then compared to a carrier wave, typically a
triangular one with magnitude V_T and larger frequency than the sinusoidal waveform, to
generate the PWM signal that is used to drive the switches s_a, s_b, s_c that produce the AC
waveforms. Figure 2.9 showcases this approach for different cases of modulation signals:
$m = V_M/V_T$.
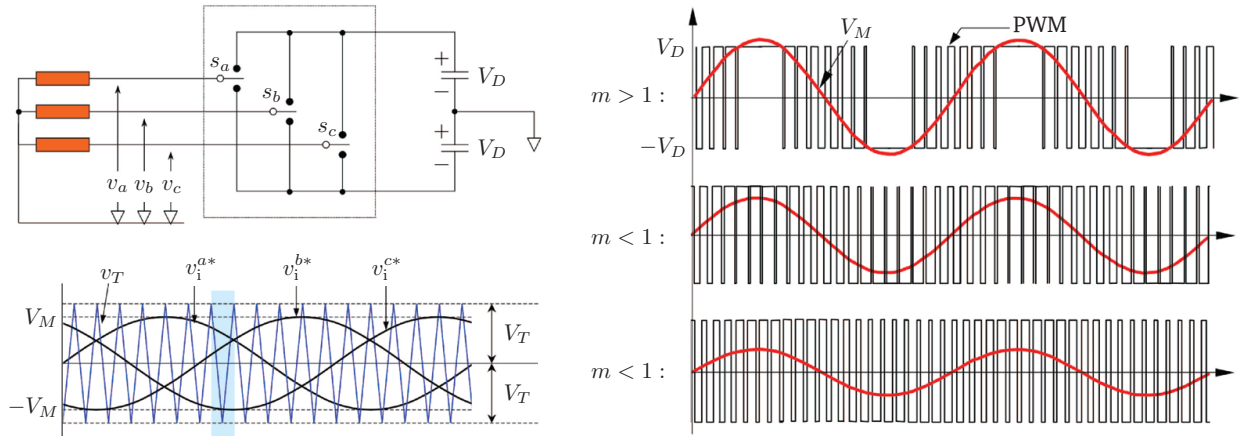
Figure 2.9: Common modulation approach to generating the AC waveforms using an inverter.

A typical approach is to use the magnitude of the triangular carrier to be equal to the DC magnitude $V_T = V_D$, then, as described in [139], the average model (that describes the fundamental frequency of the AC waveform generated), will be:

$$\bar{v}_{\mathrm{i}}^a = m(t) \cdot V_D = \frac{v_{\mathrm{i}}^{a*}}{V_D} \cdot V_D = v_{\mathrm{i}}^{a*} \tag{2.2}$$

that yields the common result for power systems studies, on which the reference signal generated in the current controller is the voltage source created from the inverter. For the remaining of this chapter, all inverter models will be considered as average models and no saturation or cases when $m > 1$ are considered.

Once v_{i} is determined, AC filter dynamics are used to interface with the grid voltage v_{g}. Later in this chapter we will explore how neglecting some of these filter dynamics can have significant effects in stability regions for inverter controllers.

Control structures of GFM converters

Figure 2.10 depicts a typical GFM converter control block implementation. The largest difference is that a GFM implementation does not require a PLL block to ensure synchronization to the grid, which is done via different approaches in the Outer Control. The most common approach (mentioned in Figure 2.10) is the so-called droop control.

A common aspect with the GFL control block presented in Figure 2.5 is the current controller, which is the same as presented in Figure 2.8.
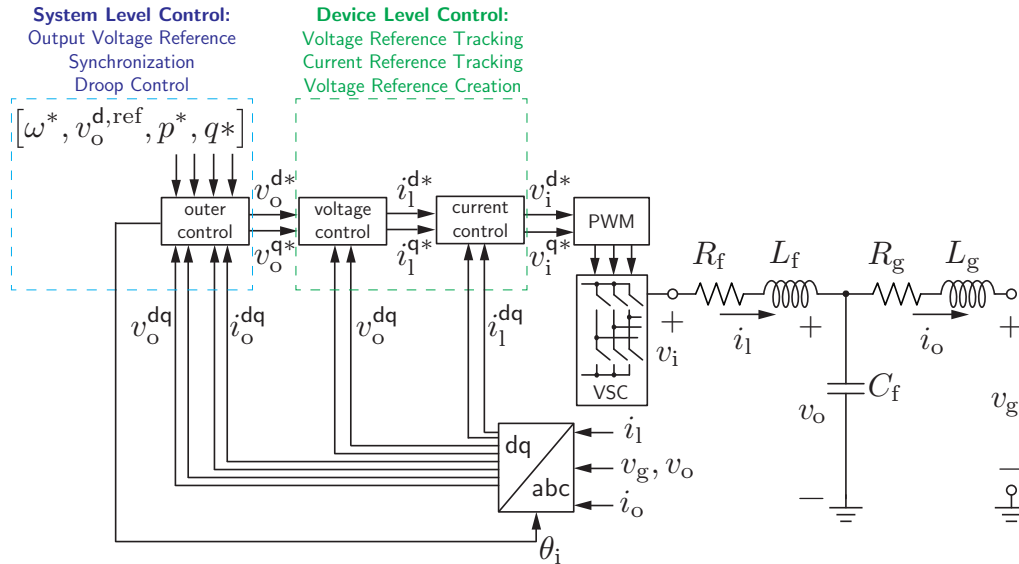
Figure 2.10: Typical GFM converter control block implementation. Figure adapted from [74].
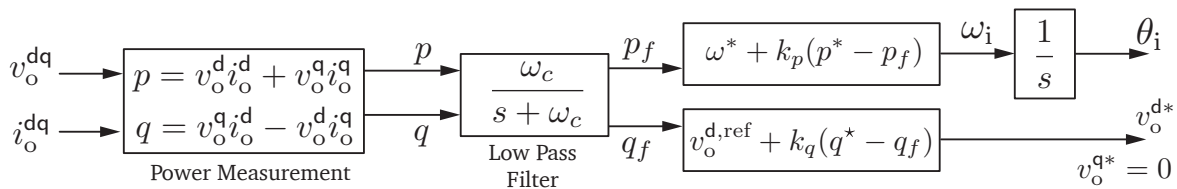
Figure 2.11: Typical system-level droop control block diagram.

System Level Control: Droop Control

Droop control is one of the most prevalent control schemes for parallel GFM converters. Synchronization is achieved through measuring power imbalance, inspired by the traditional governor frequency control of an SM. Adjusting the individual droop factors, k_p, k_q, enables self-synchronization using only local measurements through the power grid and power sharing between multiple generating units. Figure 2.11 presents a block diagram for p-f and q-v droop control. Filtered measurements of both active p_f and reactive power q_f are compared to reference values p^* and q^*, respectively. The error terms are used in two independent proportional controllers to generate the inverter frequency ω_i, and voltage reference $v_\mathrm{o}^{\mathsf{d}*}$ in the d-axis.
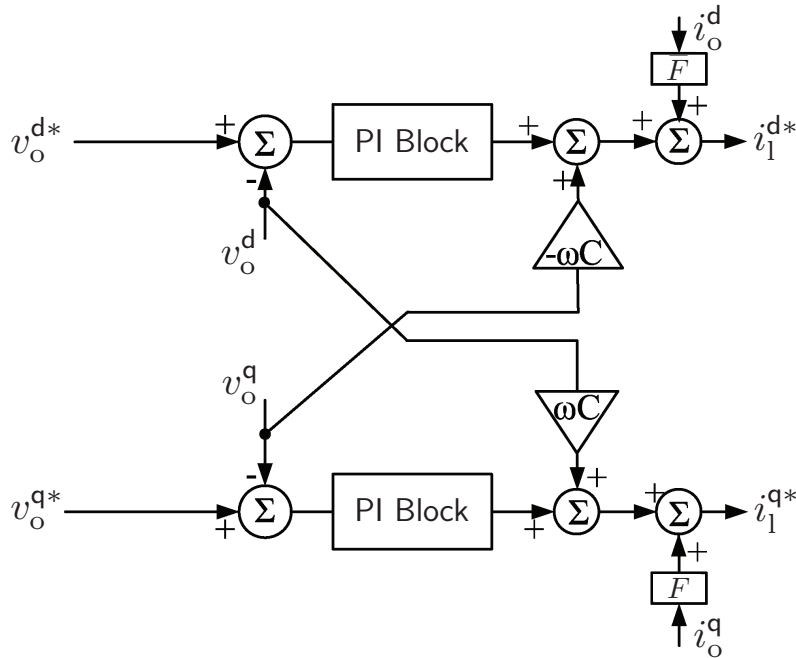
Figure 2.12: Typical device-level voltage controller block diagram.

Device Level Control: Voltage Controller

The voltage controller attempts to track the voltage reference at the capacitor v_o to the reference provided by the system-level control v_o^*. This is achieved using a PI control block. Similarly to the current controller, decoupling terms $j\omega C v_o$ are included due to the coupling effect in a dq-framework. This controller is depicted in Figure 2.12. Additional feed-forward terms in the controller can be included if the parameter F is set to a non-zero value.

Desired System Level Functionality for IBRs

Departing from the specific control block structure of IBRs, we now discuss desired functionalities of these resources. In this section, we will focus on system-level attributes and in the following section we will consider specific unit-level capabilities. By *system-level functionality*, we refer to desired grid attributes that can only be articulated completely for networked connections of multiple GFL or GFM IBRs (and other grid assets). The most common system-level functionalities highlighted in the literature, and technical reports such as [73, 7, 13, 47], include four major attributes: frequency response, voltage support, stability, and system protection and restoration.

Frequency Response

Power system frequency is a network-wide quantity, i.e., it is a common constant across a connected network under steady-state conditions. Moreover, for grids dominated by rotating machines, it is a natural proxy for demand-generation balance. In particular, any imbalance between the power supply and load demand manifests as a deviation from a nominal steady-state value. The need for frequency response/regulation following a disturbance event (e.g., loss of generation / large loads) is multi-fold. Following an event, the objective is to keep the system frequency within specified limits, limit the Rate of Change of Frequency (RoCoF), and ensure subsequent return to nominal value. These can be achieved through active-power injection at slower/faster time scales translating to either typical primary and secondary frequency response or the so-called Fast-Frequency Response (FFR), respectively. In this regard, there is a distinction between inertia and FFR. The former is ascribed as an inherent quality of an IBR device for reducing rapid frequency changes by instantaneous power adjustment without requiring any measurement or controlled response; FFR, on the contrary, is a deliberate, controlled capability via measured frequency changes [7].

By and large, frequency-response functionality can be achieved via implementation of a suitably designed inverter active power control that responds to a frequency deviation. However, the IBRs' capability to provide frequency response is limited by two major factors: the peak current capability of the inverter and the characteristics of the energy source behind the inverter (that includes headroom in energy reserve and limitations imposed by source-side dynamics). The IBR controller will respond naturally to changes in system frequency [95]; however, not all primary controllers can be expected to exhibit similar behavior. Nevertheless, some IBR devices (GFM and/or GFL) are anticipated to rapidly modify their active power injection when the system is in an emergency scenario of over- or under-frequency operation [126].

There is consensus across the literature regarding frequency-response service anticipated from IBRs. However, the natural impulse for GFM technology is to emulate pertinent characteristics of synchronous machines. For instance, [95] introduces new active-power component definitions such as *active inertia power* and *active RoCoF response power* as a desired capability for GFM IBRs. This can be problematic since inertia—as referenced in the context of electromechanics—is not directly applicable to all GFM IBRs given the variety of primary controls that could be employed. Moreover, analytical formulations for RoCoF are typically tied to machine inertia constants. This raises the question of whether such anticipated functionality is indeed drafted in a forward-looking manner, or is merely a comforting crutch grounded in practices of the past.

Voltage Support

In contrast to frequency, voltage is a local quantity as its magnitude varies across the geography of the power system (i.e., transmission/distribution levels) even in steady state.

It is mandatory to keep the voltage magnitude, as well as its harmonic contents, within acceptable limits for safe operation of all connected equipment.

IBRs are expected to provide voltage support (within operational constraints) during voltage sag/swell and phase jumps caused by disturbance events such as short circuits and line disconnections. Some efforts have attempted to crystallize requirements to contend with such conditions; for instance, [95] indicates capabilities such as *active phase jump power* and *voltage jump reactive power* are required to provide necessary voltage support in a timely manner.

A GFM plant has to inject or absorb necessary reactive power in attempting to maintain the voltage within stipulated limits at the inverter terminals (this implies that inverters need to ride through low-voltage events). Additionally, a GFM plant has to inject or absorb active power following an occurrence of a phase jump in the voltage. Notably, these responses are constrained by the peak current-provisioning capability of the inverter. This limitation implies that the frequency and voltage responses need to be coordinated during a disturbance event to ensure safe operation of the inverter.

Stability

System stability is referenced in a majority of the literature to include: i) transient stability and capability to recover after large-signal disturbances, e.g., line faults, and ii) ability to withstand disturbances and maintain small-signal stability during steady-state operation [7, 99, 126]. Grid disturbances include those seen in voltage, frequency, and phase; it is essential to reject these disturbances to maintain network synchronism. In the context of system with high IBR shares, key issues with frequency stability are the introduction of new oscillatory modes via negative control interactions and reduced system damping [40]. The following are some aspects mentioned in the literature in the context of stability:

- System loads and dynamic behavior of sources in terms of active and reactive power injections are noted to be critical for *voltage stability* [73, 126]. Classically, voltage stability focuses on the ability of a power system to maintain voltages close to the nominal value at all network buses after occurrence of a disturbance [40]. The aspects to be considered for voltage stability critically depend on the considered magnitude of disturbances (small/large) and analysis timescale (short-term/long-term). Furthermore, voltage stability, is a joint attribute of the network, operating conditions, and dynamic behavior of loads/generators. Hence, an isolated emphasis on loads and generators may be limiting, as representation of network dynamics and interactions is also necessary.

- RoCoF is highlighted as a key index for stability and the increase in RoCoF in light of increased IBR shares is brought up as a major power-system stability challenge [126].

- The terms *weak grids* and *(low) system strength* generously accompany references to stability and the ability to maintain network synchronism [7, 126]. Unfortunately,

given its multiple aspects and their subjective characteristic depending on the specific system, a precise notion on system strength, such as large- or small-signal stability, can be problematic. In some cases, a large Short Circuit Ratio (SCR) is used as a term of grid strength, and with the inclusion of larger shares of IBRs, is expected to this system characteristic to decrease given the hardware limitation for output current on IBRs. However, the specific impacts of such changes in stability remain to be properly precised, and is an interesting direction of future research.

System Protection and Restoration

Prevailing protection systems that defend the grid against short-circuit faults consist of protective relays and circuit breakers that were designed to detect, locate, and isolate large fault currents expected from synchronous generators. While various methods may be utilized to detect and locate overcurrents flowing from generators, these protective relays and breakers are ubiquitous across the electrical grid. To avoid the high costs of redesigning or replacing the present protection equipment that were tuned to the predictable behavior of synchronous generators, [73] and [13] emphasize the importance of the compatibility of IBRs with established protection protocols. However, protection system philosophy needs to be reevaluated in the future so that it responds to the behaviour of IBRs.

Challenges with IBRs can occur at the distribution and transmission level. In the distribution system, higher risk of incorrect operation of existing protection schemes, which were designed with one-way power flow in mind, is a problem. While IBRs can be designed to provide fault currents that match that of synchronous generators, they are typically not due to the cost of components. Usually, IBRs are programmed to limit fault current to 1.1-1.5 times the nominal value, so that current ratings of the switches are not breached during operation.

At the transmission level, some protection systems rely on synchronous generators injecting large negative-sequence currents to identify unbalanced faults. Hence, [73, 99, 95, 126, 7] seek similar fault current contributions from GFM IBRs to maintain the utility of traditional protection schemes. In addition, [73] notes that protection systems are also in place to detect out-of-step events and power swings caused by changes to the system state. Broadly, there is agreement across the reviewed literature that further research is needed to understand how IBRs (particularly GFM) interact with existing protection systems.

In addition, for GFM IBRs, it is crucial that they stay connected to the bulk power system to support synchronization and contribute to restoration if needed. Currently, synchronous generators underpin black-start procedures that are initiated after major outages. A fraction of future GFM inverters may be required to self-start to establish a voltage and synchronize with other generators/inverters to black start a system. Fundamental necessities are also the ability to maintain the system voltage and frequency while load and network segments are being connected to the restored system. Finally, GFM IBRs must be able to operate in islanded operation until they are able to synchronize with adjacent areas to form the larger

grid [54, 16].

Each system level function can be achieved through a number of unit-level capabilities which are also highlighted as bullet points alongside the system-level function. We discuss these next.

Unit-level Capabilities

By *unit-level capability*, we mean the functions that can be engineered into individual IBRs (extending to plants and aggregations as appropriate) to meet the system-level functions mentioned previously. In general, both GFM and GFL IBRs are anticipated to provide individual features, such as voltage control and variable power factor operation, to unlock their full potential. Additional capabilities such as operation, in which inverters modify their active power injection in response to system frequency variations, may be expected from IBRs in general. However, it is expected that GFMs ought to deliver these services faster, and in a more stable and reliable fashion, compared to GFLs [73].

Figure 2.13 summarizes system-level functionalities (as described earlier) and ties them to unit-level capabilities that will be discussed in detail subsequently. Notably, we will identify fault ride-through as an essential feature for every system-level functionality. For example, [126] features a categorization of IBR types into three equipment *classes* based on type of grid-support features and the ability to operate in grids approaching 100% IBR shares. Classes 1 and 2 reflecting respectively, the early renditions with basic functionalities (e.g., GFLs with no grid support) and the recent advanced versions (e.g., GFLs with grid support); Class 3 is conceived as a future class of IBRs that incorporates GFM attributes at the unit level to support power system operation under normal, abnormal, and emergency conditions. The inverters in this class are envisioned to operate seamlessly in grids with 100% IBR penetration, without relying on services from synchronous generators. Furthermore, towards achieving system-level functionalities, the sought unit-level capabilities are conceived to be provided in a shared manner by individual IBR units, e.g., while some IBRs create system voltage and contribute to fault level in the positive sequence, other IBRs in the power system could serve as sinks for unbalance [126].

Ride-through and Fast Fault-current Injection

Ride-through refers to the capability of IBRs to remain connected to the grid during a disturbance. In general, for voltage ride-through, predetermined levels of high- and low-voltage limits exist which dictate disconnection of inverters from the grid. Specific limits will depend on specific grid codes of each individual power system. Both [95] and [126] recognise that reactive current injection is required during voltage sags. To prevent disconnection of assets present in the network during a voltage sag, they specify a fast reaction time (from IBRs) of less than one quarter cycle for terminal voltage dips below below 90% of nominal value.
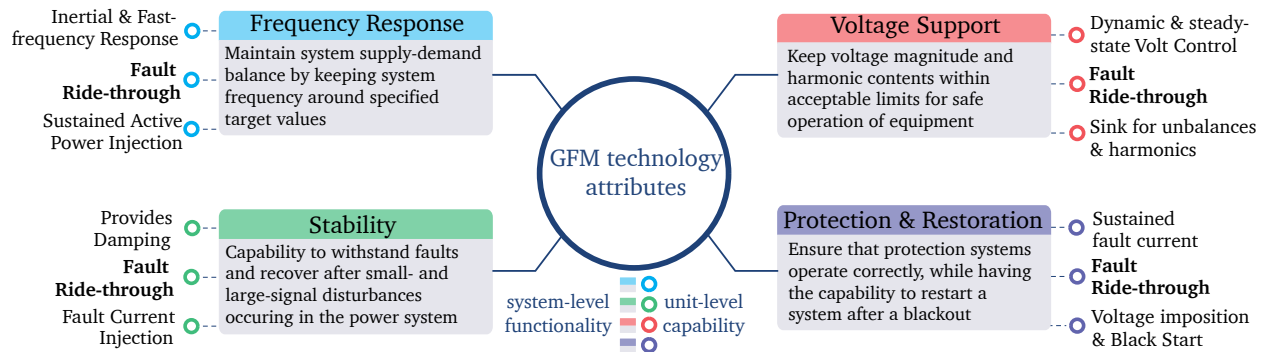
Figure 2.13: Summary of system-level functionality linked to associated unit-level capability.

For faults, fast fault-current injection capability of the IBR is recognized as vital in the literature. This refers to the inverter's ability to inject current instantaneously into the system during faults at the point of interconnection. While a synchronous machine provides this type of response inherently, due to its electromagnetic physics, a GFM inverter can provide this functionality as a result of its fast control action. Given the specific fault, IBRs will be required to inject current with specific characteristics, e.g., active and/or reactive current, to sustain the voltage for an extended period.

The fundamental issues here are twofold: i) in case of GFLs, the unit-level controller relies on the external voltage source (i.e., grid) for synchronization. During, or after, a disturbance, the source voltage quality may be severely affected, which makes synchronization and power injection challenging for GFLs. Since GFMs do not rely on an explicit external signal for synchronization, they offer greater potential to tackle disturbances and ensure desired power injection; ii) Inverters cannot handle currents exceeding the ratings, and hence, even in case of GFM, they cannot allow large currents to be injected during faults and maintain the imposed voltage phasor magnitude and frequency (unlike a synchronous generator that can typically support up to six times the full rated current during faults.). Inverter current-limiting approaches need to trade off inverter hardware limits, and its economic cost, with system stability concerns.

Additionally, unbalanced faults are of particular concern as they are difficult to handle by IBRs as compared to balanced ones. In this regard, both GFL and GFM controls are required to be capable of injecting negative-sequence currents to achieve reduction in voltage imbalance across the network. This may require the usage of alternate control structures (moving away from the conventional direct-quadrature-zero dq0 frame) and more expensive hardware (with four instead of three wires) as recognized by [73].

Inertia and Damping

With the retirement of SMs, there is concern over the loss of inertial energy injection in the electric network and thus the grid-supporting functions along with it. Inertia, in the context of power systems, has extended beyond its original concept as the physical property of the rotating masses of SMs to describe an inherent resistance to frequency and phase angle changes. Indeed, power electronics do not possess physical inertia but can offer a similar function as synchronous generators of responding to and arresting system-frequency changes. In the literature, *frequency control* [73], *frequency regulation* [13], *active inertia power* [47], and *inertial response* [99] can capture such intended functionality. In essence, IBRs should be able to dynamically adjust their active power injections in response to changes in system frequency and restore it to its nominal value when equipped with the appropriate controls.

The frequency regulation capability of IBRs is determined based on the available power and energy headroom, and the current ratings. Requirements at the system level, should, therefore, be cognizant of what can be accomplished at the unit level. However, there are some examples of system-agnostic unit-level requirements; for instance, [13] requires a response within 5 ms of the onset of changes to system frequency, and [99] recommends fast responses that match or are quicker than that of the inertial time-frames of the primary controls of synchronous generators. In addition, IBRs will be expected to dampen active power oscillations and stabilize system frequency and power flows after disturbances. With adequate headroom in power, energy, and current, control strategies can be implemented that harness such damping from IBRs. For example, [47] mentions that GFM plants are required to possess active damping power capability and adhere to an operating bandwidth limit of 0-5 Hz. Damping factors in the range of 0.2-5 Hz are also prescribed.

Finally, we note that damping serves are generally in place to protect the mechanical equipment of synchronous generators from damage and fatigue. For IBRs, focus is placed on eliminating high-frequency oscillations that may be introduced by adverse interactions among electronic components and caused by fast control loops. Moreover, the implementation of GFM controls should not produce any unwanted oscillations through unnecessary mode excitation. If oscillations do arise, GFM IBRs should be capable of mitigating them.

Power Quality

The issue of power quality, with respect to individual IBR units, is recognized in the literature [126]. This is described as quality covering two aspects: i) sink for harmonics, ii) sink for unbalance. i) relates to the ability to maintain high voltage quality at the point of connection while providing damping response in the harmonic frequency range by permitting harmonic current flow up to a certain frequency range. In terms of damping performance, in view of the inherent control flexibility in IBRs, it is also recognized that GFM IBRs can provide enhanced damping by mimicking inductive-resistive impedance behavior virtually. Finally, attribute ii) pertains to the ability of the IBR to handle unbalanced grid conditions

and provide appropriate negative sequence impedance paths to allow (and limit) negative sequence currents, much like the traditional synchronous generators.

Realizing future power systems with high shares of renewable resources will require that IBRs provide grid services that are nowadays provided by synchronous generators. In specific, grid-forming technologies show a promising pathway for achieving this goal. In this section we have highlighted the fundamental control blocks of IBRs and several system needs and unit-level functionality in order to understand requirements of both inverter manufacturers and system operators. Unifying both aspects is recognized as one of the fundamental challenges to be addressed for a sustainable future. In the following sections we will discuss additional challenges and opportunities in the numerical simulation aspects for integration of IBRs in future power systems.

2.2 Scientific Computing Challenges and Opportunities for Transient Simulations with Presence of IBRs

As mentioned earlier, due to the complexity of power systems, research in this area heavily relies on computational tools and simulation. With the increasing integration of IBRs (and displacement of SMs) results in a reduction of the network short circuit strength at multiple points of connection of IBRs. Under these conditions, state-of-the-art positive QSP platforms and models can have difficulties maintaining numerical stability and/or providing an accurate numerical representation of IBR dynamic behavior [111].

Fortunately, the array of software tools available for researchers to conduct large scale studies has also grown significantly. Progress in numerical solver algorithms, model order reduction techniques, automatic differentiation, and symbolic and numerical computation, among other areas, are advances essential to the development of the new analysis techniques demanded by the realities of a modernizing grid. The power systems field is ripe with current and future opportunities to exploit these techniques for novel modeling and control methods. However, critical obstacles remain and, among these, researchers must develop the capacity to surmount dramatic increases in modeling complexity.

This section in this dissertation focuses on the importance of scientific computing principles and showcases the modern software developments that enable large-scale power system studies. We stress that computer-aided simulation research has to be replicable. Results must be validated, and systems should be scalable such that they are of realistic proportions and make a significant contribution to our understanding. We discuss how the Julia programming language can be used to tackle these challenges, and outline the ways that "The Scalable Integrated Infrastructure Planning" (https://www.nrel.gov/analysis/siip.html) initiative at the National Renewable Energy Laboratory (NREL) is capturing these opportunities in power systems analyses [43].
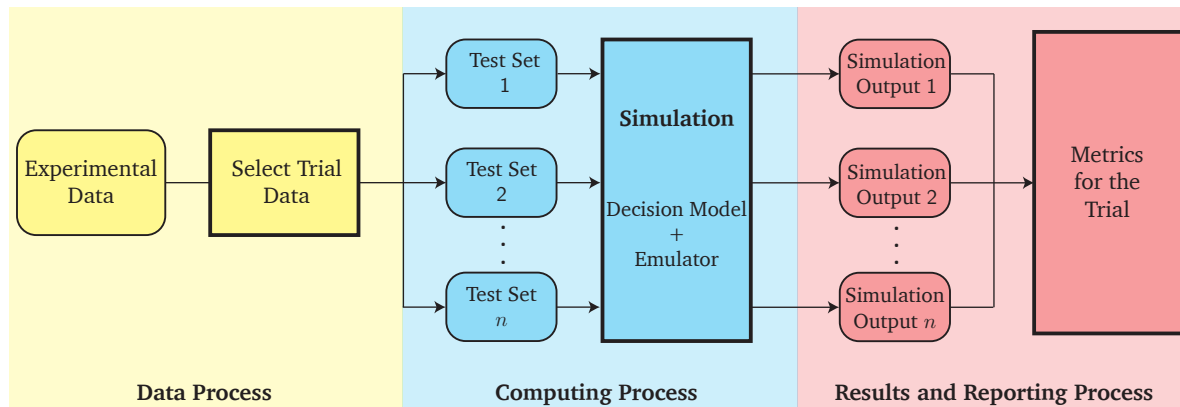
Figure 2.14: Computing steps for conducting a single trial [43].

Scientific Computing Practices

There is no single definition of Scientific Computing, as the field has evolved from purely computational issues to the general use of computers and software to answer scientific questions. However, all Scientific Computing definitions share the objective of enabling (1) the *reproducibility* of the experiments and (2) mechanisms to verify the *validity* of conclusions derived. [67] provides a detailed discussion of these definitions for power system operational studies. Figure 2.14 summarizes the three steps required to perform a simulation experiment that follows best practices in Scientific Computing: data, computational modeling, and results sub-processes.

In practical terms, achieving reproducibility and validation requires that two major components are kept in mind: the *environment* and the *experimental workflow*.

- *Environment:* The hardware components, the configuration of all the software used to implement a computational experiment. The environment may include elements such as cloud-services, third-party software, file management scripts, and external tests.

- *Workflow:* The full process of data intake, computation and results. The development and provision of a workflow is a requirement for validation and reproducibility.

In this respect, open-source tools provide the required capabilities to facilitate Scientific Computing for power systems research. Despite challenges, several open-source efforts have grown to become successful in the community and reduce the barrier to entry for those seeking to perform high quality research and reliable analysis. MATPOWER [141] (https://matpower.org) is a MATLAB-based tool that is widely used to perform steady-state analyses such as power flow, continuation power flow, and optimal power flow. OpenDSS [30] (https://smartgrid.epri.com/SimulationTool.aspx) is used for
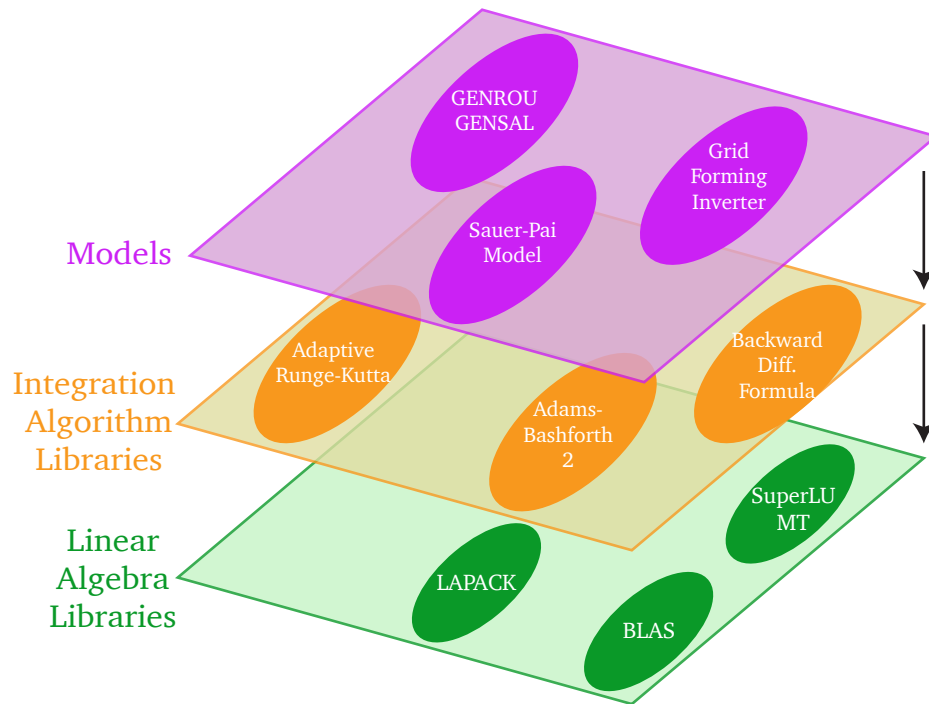
Figure 2.15: Time-domain simulation software stack [43].

multiple distribution systems analysis. In the field of transient simulations, the MATLAB-based tool PSAT [84] (http://faraday1.ucd.ie/psat.html) provides electro-mechanical simulations with multiple models. More recently the Python-based tool ANDES [25] (https://docs.andes.app/en/stable/) has become available for power system simula-tion. It uses a hybrid symbolic-numeric framework for numerical analysis.

However, there is a high setup cost associated with developing dynamic simulation applications that can run large-scale experiments. For this reason, researchers resort to using industrial tools once their systems of interest grow larger than hundreds of buses. However, these proprietary models and algorithms are not openly available; this means that both using them and replicating the results obtained by other researchers who use them requires large sums of money for license acquisition. This common practice reduces the capacity for innovation in the power systems field for researchers who must, rather than use industrial tools, re-implement these well-established models, develop their own data sets, and handle the integration libraries. This reality translates to the fact that scientific reproducibility is often either not achieved or limited to "code sharing".

Simulation reproducibility requires the separation of models and algorithms when de-veloping modeling libraries. Figure 2.15 shows the software stack of a dynamic modeling application:

1. The modeling layer: All the code representation of the system behavior in differential

and/or algebraic equations. For instance, charging and discharging capacitors or PID controllers.

2. The integration algorithms: The libraries that implement an integration scheme and are used to obtain the numerical solution of the models' differential equations. For instance, Euler, Backwards Differentiation Formula, Runge-Kutta, among others.

3. Linear Algebra libraries: Low level algorithms to perform numerical linear algebra calculations for system solutions, LU decomposition or eigenvalue calculations.

Novel research needs improvements at all levels of the software stack. However, progress requires that the computational experiments be replicated under many conditions. Free and open-source validated models that provide a benchmark for the development of algorithms are a critical step that currently isn't available. Stable and reliable implementations of integration algorithms usually require tremendous development efforts and limit the scope of the models to small systems.

More tools are appearing to address each of these modeling needs, thanks to the advent of code-sharing repositories (such as Github or Gitlab), broad access to software development tools, and the popularity of open-source programming languages like R, Julia, and Python. However, without a deliberate effort to develop a platform that can be reused by many researchers, we risk limiting the scope and scale of power system research or duplicating efforts. In this context, the programming language Julia offers a host of unique features that significantly reduce the effort to implement scientific computing practices to simulate low-inertia power systems.

Computational Challenges of Systems with Significant Shares of IBRs

Dynamic analysis of power systems resorts to mainly two computational numerical methods: (1) Time-domain simulations and (2) small-signal stability analysis. For many decades, there has been a focus on reducing time-domain simulations' computational complexity through model order reductions. Some of the modeling practices and analytical assumptions currently in use derive from singular perturbation theory in the 1980s. The seminal papers showed that a simplified model is still a valid representation of certain system dynamics under the premise of time scale separation [18, 117].

Traditionally, time-domain simulations assume that the fundamental frequency of the system dominates current and voltage wave-forms. As a result, the network can be simplified to a voltage and current phasor representation, known as the QSP modeling approach. Additionally, synchronous generator stator fluxes relationships reduce to algebraic equations, further simplifying the QSP modeling approaches. However, this representation cannot capture some of the converters' high-frequency dynamics.

Modeling and Timescale Aspects

In power systems dominated by synchronous machines, the source of dynamics is physical phenomena with a behavior described by physics laws. The parameters of the logical controls like PIDs determine the dynamics of converters. These two dynamic behavior sources can interact unexpectedly, and the guidance of time-scale separation may not apply. Hence, when studying massive integration of power electronics interfaced sources, it is impossible to know a priori if and at which time scales interactions may occur and requiring dynamic simulations to capture fast EMT at a large-scale introduces computational challenges. IBR controls consider multiple models such as PWM representation, PLL, voltage and current controllers, outer-loop controllers, that have wide timescale ranges, that complicates the determination of which level of model complexity has to be used.

From the analytical perspective, QSP and EMT modeling approaches are similar. They use DAEs to represent the system dynamics. The dynamic models used in the power industry tend to be stiff since they represent phenomena at multiple rates. Depending on the model's time constants, the required integrator time steps can impose substantial computational requirements. In QSP models, the maximum time-step is around 1 to 10 ms. Simultaneously, EMT time-step usually is about 1 to 50 μs. As a result, QSP simulations are typical when modeling large interconnected areas like continental Europe or the Eastern Interconnection in the United States. They are usually used to study the transient response of different disturbances and require significant simplifications. On the other hand, EMT simulations have a smaller scope. They are commonly used to analyze a single device's dynamic behavior against infinite buses.

The difference in modeling complexity also means that the QSP and EMT simulations' solution methods are also very distinct. Commercial tools for QSP modeling typically implement Adams-Bashforth-2 and use explicit formulation through mass matrix representations. On the other hand, EMT software tools use the trapezoidal rule (Adams-Moulton-2) and directly model the electromagnetic differential equations (also known as the Dommel method) in the solution process.

Jacobian Computation

In large systems with detailed models, the calculation of Jacobian matrices and eigenvalues can require significant computational effort. There are multiple opportunities to recent advances in automatic-differentiation (AD) from the machine learning community to obtain exact Jacobians in this area. Exact Jacobians have myriad uses in dynamic modeling, from algorithmic design to parameter evaluation.

Calculating the system eigenvalues for multiple operating conditions and parameter values is standard practice to study power systems' stability. Fast and exact Jacobian matrix calculation and sparse linear algebra are two basic capabilities that will improve studies on systems with large shares of IBRs.

The new demand for larger scales and more details in modeling require changing how we approach developing simulation experiments. To do this, we need innovative approaches to obtain reliable system assessments better computational tools. The power system sector needs to accelerate the adoption of recent improvements in algorithms and hardware. To this end, adopting scientific computing practices is critical to reducing development and deployment barriers. We now discuss how the Julia Programming Language can help on these aspects.

The Julia Programming Language

Choosing a programming language to develop a simulation tool can seem like a marginally relevant decision. However, the choice can have significant impacts on reproducibility and scalability. Scripted programming languages usually do not implement high-performance code natively. High-performance applications require low-level compiled languages to handle large-scale computations. For instance, there are many API identical but distinct implementations of NumPy for linear algebra in Python. The same applies to many other large-scale numerical libraries like LSODA, Sundials, or PETSc. These well-established high-performance numerical libraries are hard to extend. Usually, they have dependencies on other compiled libraries like BLAS, LAPACK, or SuiteSparse, as shown in Figure 2.15 adding additional complexity.

Julia is a dynamically typed programming language developed by Jeff Bezanson, Stefan Karpinski, Alan Edelman, Viral B. Shah, and other contributors, intending to bridge the gap between scripting languages like Python or MATLAB and high-performance languages like C++ or Fortran [12]. Julia uses a Low-Level Virtual Machine (LLVM)-based Just-in-Time (JIT) compiler and incorporates some essential features from the beginning of its design, such as excellent support for parallelism and GPU programming, and features a practical, functional programming orientation. Julia can generate the same assembly code as C/C++ with the convenience of the scripted languages.

Besides the language's computational capabilities, the Julia environment itself provides several features that facilitate the development of large-scale dynamic models following scientific computing practices. Importantly, it addresses the shortcomings of other scripted languages, such as dependency handling. These capabilities make Julia an excellent match to tackle Scientific Computing challenges in the power systems community. Critical examples of Julia's good environment include:

- A comprehensive package manager that easily enable reproducibility between researchers by setting up the exact package and binary versions. Integrating "Artifacts" into the package manager, Julia can include information that is not related to Julia packages that includes platform-specific binaries or datasets. This allows researchers to pack all the experiment requirements in a reproducible environment that can be executed in multiple platforms. This mechanism is also used to provide reproducible binary dependencies for packages built with `BinaryBuilder.jl`.

- A suite of packages for scientific machine learning (`SciML`), with multiple differential equation solvers (`DifferentialEquations.jl`) and automated model discovery (`DiffEqFlux.jl`). `DifferentialEquations.jl` offers over 30 different numerical solvers for Ordinary Differential Equation (ODE)/DAE systems including both explicit (via mass matrices) and implicit representation. Some solvers, including classic algorithms and novel ones from recent research, can outperform the "standard" C/-Fortran methods. In addition, `DifferentialEquations.jl` provides a wrapper for those C/Fortran methods, allowing to use them when its necessary. In a nutshell, `DifferentialEquations.jl` allows solving differential equations using different algorithms (even from other packages or languages) by providing a common interface. Effectively, it allows exchanging the algorithm layer with a single line of code. This feature allows benchmarking and testing different solution methods according to the specific problem.

- Small signal stability analyses such as eigenvalue location, root locus or bode plots rely on computing the Jacobian of the non-linear DAE system. Usually, derivatives are computed via a finite differences approach, that is inefficient due to the high number of evaluations of the system function, and only approximates its result due to the usage of the finite small value of the step h. Automatic Differentiation (AD) is a method to compute exact derivatives given only the function itself. `ForwardDiff.jl` and `ReverseDiff.jl` are the most common established packages to perform AD to compute derivatives in Julia. Both of these methods generally outperform non-AD algorithms in both speed and accuracy.

2.3 Implementation and Usage of PowerSimulationsDynamics.jl

The features and capabilities mentioned in Section 2.2 are used extensively as part of "The Scalable Integrated Infrastructure Planning" (NREL-SIIP) to provide tools that implement the scientific computing workflow in Fig. 2.14. In this section we discuss first `PowerSystems.jl` as the NREL-SIIP tool for data modeling and `PowerSimulationsDynamics.jl` for performing time domain simulations.

PowerSystems.jl

`PowerSystems.jl` provides a consistent and high-performance data model and modular modeling platform for power systems across multiple timescales. Along with the data containers, `PowerSystems.jl` furnishes parsing capabilities from commonly used text-based data files (MATPOWER, *.raw and *.dyr). Once the system is loaded, users can make modifications, add custom models and serialize to disk. The serialization/deserialization
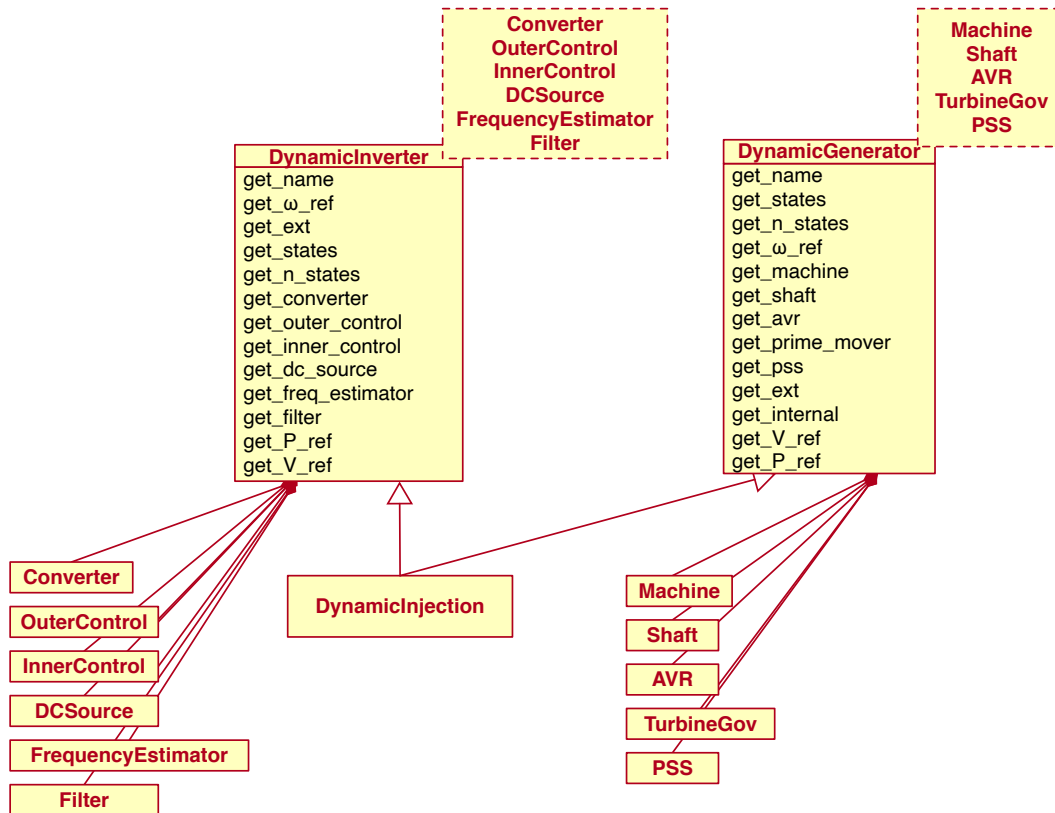
Figure 2.16: Dynamic data structures implemented in `PowerSystems.jl` [43].

of custom data sets is one of the key enablers of the Julia ecosystem to support scientific computing practices for power systems modeling [69].

For developers, `PowerSystems.jl` provides a generic, reusable, and customizable data model agnostic to the implementation details of the mathematical models and applicable to multiple software strategies. It also provides extension capabilities by design that make it easier to integrate into other initiatives.

Figure 2.16 shows the implementation of the `DynamicInjection` data containers in `PowerSystems.jl`. Each device is composed of the corresponding dynamic components that define the model. As a result, it is possible to flexibly define dynamic data models and methods according to the analysis requirements. `DynamicInjection` components use a parametric type pattern to materialize the full specification of the dynamic injection model with parameters. This design enable a modular implementation of the mathematical model implemented in `PowerSimulationDynamics.jl` for each dynamic component separately.

Gen 1

Machine: Classic
$$\begin{bmatrix} i_d \\ i_q \end{bmatrix} = \begin{bmatrix} r_a & -x'_d \\ x'_d & r_a \end{bmatrix}^{-1} \begin{bmatrix} -v_d \\ e_q - v_q \end{bmatrix}$$
$$P_e = (v_q + r_a i_q)i_q + (v_d + r_a i_d)i_d$$

Shaft: SingleMass
$$\dot{\delta} = \Omega_b(\omega - \omega_s)$$
$$\dot{\omega} = \frac{1}{2H}(\tau_m - \tau_e - D(\omega - \omega_s))$$

AVR: FixedAVR

TurbineGovernor: FixedTG

PSS: NoPSS

Gen 2

Machine: One d- One q-
$$\dot{e}'_q = (-e'_q - (x_d - x'_d)i_d + v_f)/T'_{d0}$$
$$\dot{e}'_d = (-e'_d + (x_q - x'_q)i_q)/T'_{q0}$$
$$\begin{bmatrix} i_d \\ i_q \end{bmatrix} = \begin{bmatrix} r_a & -x'_q \\ x'_d & r_a \end{bmatrix}^{-1} \begin{bmatrix} e'_d - v_d \\ e'_q - v_q \end{bmatrix}$$
$$P_e = (v_q + r_a i_q)i_q + (v_d + r_a i_d)i_d$$

Shaft: SingleMass
$$\dot{\delta} = \Omega_b(\omega - \omega_s)$$
$$\dot{\omega} = \frac{1}{2H}(\tau_m - \tau_e - D(\omega - \omega_s))$$

AVR: SEXS
$$T_e \dot{V}_f = V_r + \frac{T_a}{T_b}V_{\text{in}} - V_f$$
$$T_b \dot{V}_r = \left(1 - \frac{T_a}{T_b}\right)V_{\text{in}} - V_r$$
$$V_{\text{in}} = V_{\text{ref}} + V_{\text{pss}} - V_h$$

TurbineGovernor: FixedTG

PSS: NoPSS

Figure 2.17: Mix and match different components for generators and their respective DAEs.
Figure adapted from [44].

PowerSimulationsDynamics.jl

The mathematical models and equations are implemented in `PowerSimulationsDynam-ics.jl` (PSID) and uses `PowerSystems.jl` data structures to define power system dynamic devices and their corresponding components and data. The modeling layer is designed to mix and match different component models with a small number of script modifications. The flexibility of model specification enables precise control when specifying the complexity of each power system device.

Figure 2.17 provides an example of the modularity capabilities when defining a generator model. As depicted, it is possible to exchange generator components to study the effects of different complexity levels. In this particular case, it is possible to exchange the generator's machine model between the classic algebraic representation in the two-state machine with the 2-state transient model of the 4-state machine (one-d one-q), while also adding an excitation system (SEXS model). This flexibility is key to studying under-explored and emerging challenges in future systems with large shares of IBRs. For example, including

multi-mass shaft dynamics can be used to study torsional interaction between generators
and IBR power sources and their controllers, an issue that has been reported in systems with
High-Voltage Direct Current (HVDC) lines and Flexible AC Transmission System (FACTS)
[63]. In addition, this enables the analysis of controller architecture upgrades to enhance
the resilience of the system as the adoption of IBR sources increases.

PowerSimulationsDynamics.jl Multiple Dispatch

Julia's multiple dispatch lies at the core of `PowerSimulationsDynamics.jl` power as a
scientific scripting and computing library for dynamic models. It uses the compiler to
determine which method to call based solely on the types of argument passed into a generic
function. This is a way to enable code reuse, and the implementation of generic interfaces
for custom models, without requiring modifications to the main source code.

The flexibility in PowerSimulationsDynamics.jl originates from the use of *polymorphism*
and encapsulation in the device model definition, which enables treating objects of different
types similarly if they provide common interfaces. Generators and inverters are defined as
a composition of components as shown in Fig. 2.16; the functionalities of the component
instances determine the device model providing a flat interface to the complex object.
This design enables the interoperability of components within a generic device definition.
As a result, it is possible to implement custom component models and interface them
with other existing models with minimal effort. As an example, Code 2.1 and Code 2.2
present the implementation of the method of `mdl_machine_ode` for the classic machine
(`BaseMachine`) model and One d- Oneq- machine model (`OneDOneQMachine`) respectively.
The core implementation of machine models reads bus voltage and machine parameters
to compute the electromagnetic differential equations (`output_ode`) of specific model and
output the current to the system (`current_r` and `current_i`).

Code 2.1 `mdl_machine_ode` dispatch function for Classic Machine.

```
1   function mdl_machine_ode!(
2       device_states::AbstractArray{<:ACCEPTED_REAL_TYPES},
3       output_ode::AbstractArray{<:ACCEPTED_REAL_TYPES},
4       inner_vars::AbstractArray{<:ACCEPTED_REAL_TYPES},
5       current_r::AbstractArray{<:ACCEPTED_REAL_TYPES},
6       current_i::AbstractArray{<:ACCEPTED_REAL_TYPES},
7       dynamic_device::DynamicWrapper{PSY.DynamicGenerator{PSY.BaseMachine, S, A, TG, P}},
8   ) where {S <: PSY.Shaft, A <: PSY.AVR, TG <: PSY.TurbineGov, P <: PSY.PSS}
9       Sbase = get_system_base_power(dynamic_device)
10      #Obtain external states inputs for component
11      external_ix = get_input_port_ix(dynamic_device, PSY.BaseMachine)
12      δ = device_states[external_ix[1]]
13
14      #Obtain inner variables for component
15      V_tR = inner_vars[VR_gen_var]
16      V_tI = inner_vars[VI_gen_var]
17
18      #Get parameters
19      machine = PSY.get_machine(dynamic_device)
20      R = PSY.get_R(machine)
21      Xd_p = PSY.get_Xd_p(machine)
22      eq_p = PSY.get_eq_p(machine)
23      basepower = PSY.get_base_power(dynamic_device)
24
25      #RI to dq transformation
26      V_dq = ri_dq(δ) * [V_tR; V_tI]
27
28      #Obtain electric variables
29      i_d = (1.0 / (R^2 + Xd_p^2)) * (Xd_p * (eq_p - V_dq[2]) - R * V_dq[1])   #15.36
30      i_q = (1.0 / (R^2 + Xd_p^2)) * (Xd_p * V_dq[1] + R * (eq_p - V_dq[2])) #15.36
31      Pe = (V_dq[1] + R * i_d) * i_d + (V_dq[2] + R * i_q) * i_q       #15.35
32
33      #Update inner_vars
34      inner_vars[τe_var] = Pe #Model assume ω approx 1.0
35
36      #Compute current from the generator to the grid
37      I_RI = (basepower / Sbase) * dq_ri(δ) * [i_d; i_q]
38
39      #Update current
40      current_r[1] += I_RI[1]
41      current_i[1] += I_RI[2]
42
43      return
44  end
```

Code 2.2 `mdl_machine_ode` dispatch function for One d- One q- Machine.

```julia
function mdl_machine_ode!(
    device_states::AbstractArray{<:ACCEPTED_REAL_TYPES},
    output_ode::AbstractArray{<:ACCEPTED_REAL_TYPES},
    inner_vars::AbstractArray{<:ACCEPTED_REAL_TYPES},
    current_r::AbstractArray{<:ACCEPTED_REAL_TYPES},
    current_i::AbstractArray{<:ACCEPTED_REAL_TYPES},
    dynamic_device::DynamicWrapper{PSY.DynamicGenerator{PSY.OneDOneQMachine, S, A, TG, P}},
) where {S <: PSY.Shaft, A <: PSY.AVR, TG <: PSY.TurbineGov, P <: PSY.PSS}
    Sbase = get_system_base_power(dynamic_device)

    #Obtain indices for component w/r to device
    local_ix = get_local_state_ix(dynamic_device, PSY.OneDOneQMachine)
    #Define internal states for component
    internal_states = @view device_states[local_ix]
    eq_p = internal_states[1]
    ed_p = internal_states[2]

    #Obtain external states inputs for component
    external_ix = get_input_port_ix(dynamic_device, PSY.OneDOneQMachine)
    δ = device_states[external_ix[1]]
    #Obtain inner variables for component
    V_tR = inner_vars[VR_gen_var]
    V_tI = inner_vars[VI_gen_var]
    Vf = inner_vars[Vf_var]

    #Get parameters
    machine = PSY.get_machine(dynamic_device)
    R = PSY.get_R(machine)
    Xd = PSY.get_Xd(machine)
    Xq = PSY.get_Xq(machine)
    Xd_p = PSY.get_Xd_p(machine)
    Xq_p = PSY.get_Xq_p(machine)
    Td0_p = PSY.get_Td0_p(machine)
    Tq0_p = PSY.get_Tq0_p(machine)
    basepower = PSY.get_base_power(dynamic_device)
    #RI to dq transformation
    V_dq = ri_dq(δ) * [V_tR; V_tI]

    #Obtain electric variables
    i_d = (1.0 / (R^2 + Xd_p * Xq_p)) * (Xq_p * (eq_p - V_dq[2]) + R * (ed_p - V_dq[1]))
    i_q = (1.0 / (R^2 + Xd_p * Xq_p)) * (-Xd_p * (ed_p - V_dq[1]) + R * (eq_p - V_dq[2]))
    Pe = (V_dq[1] + R * i_d) * i_d + (V_dq[2] + R * i_q) * i_q
    #Compute ODEs
    output_ode[local_ix[1]] = (1.0 / Td0_p) * (-eq_p - (Xd - Xd_p) * i_d + Vf)   #15.29 eq_p
    output_ode[local_ix[2]] = (1.0 / Tq0_p) * (-ed_p + (Xq - Xq_p) * i_q)        #15.30 ed_p

    #Update inner_vars
    inner_vars[τe_var] = Pe #Model assume ω approx 1.0
    #Compute current from the generator to the grid
    I_RI = (basepower / Sbase) * dq_ri(δ) * [i_d; i_q]
    #Update current
    current_r[1] += I_RI[1]
    current_i[1] += I_RI[2]
    return
end
```

PowerSimulationsDynamics.jl Software Architecture

Figure 2.18 shows the dependencies between `PowerSimulationsDynamics.jl` and the `DifferentialEquations.jl` libraries. The architecture of PSID is such that the power system models are all self-contained and return the model function evaluations. The Jacobian is calculated through a common-interface with `ForwardDiff.jl` [113] enabling the use of any solver available in Julia through `DifferentialEquations.jl` or any other following the common interface specification. such as Sundials [110, 48].
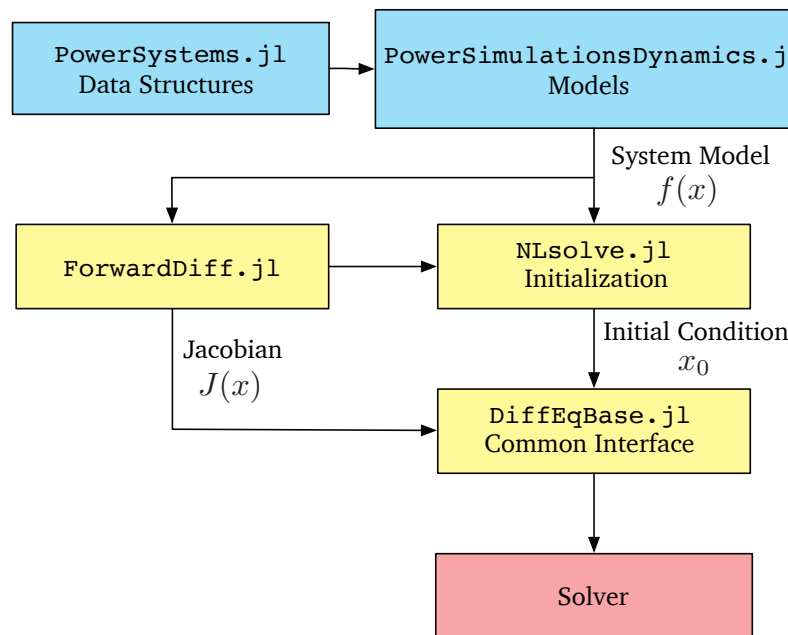
Figure 2.18: Information flow in PSID.

`PowerSimulationsDynamics.jl` provides mechanisms to handle commonly required routines when developing dynamic modeling libraries such as:

- Robust system-wide initialization of the model: Finding valid initial conditions is notoriously tricky in large-scale non-linear dynamic models. `PowerSimulationsDynamics.jl` uses routines based on the dynamic model structure to provide reliable initial points.

- Addition of perturbation through callbacks: Classically, the study of perturbations in dynamic systems requires a series of steps to obtain valid system conditions post-perturbation. `PowerSimulationsDynamics.jl` implements perturbation through callbacks, allowing the solver's algorithm to perform the reinitialization in a compatible fashion.

- Small-signal analysis: Performing small-signal analysis requires providing the Jacobian matrix or estimating through numerical methods. `PowerSimulationsDynamics.jl` uses `ForwardDiff.jl` to calculate the exact Jacobians of the models and enable small-signal analysis at no additional development cost.

`PowerSimulationsDynamics.jl` exploits the Julia programming language and its ecosystem to facilitate the computational exploration of power systems with inverter-based generation.

Example Case A: Machine, Inverter and network model interactions

As discussed so far, exploring the interactions between inverter models and other dynamics in the system is one of the critical tasks in the development of analytical techniques to study modern power systems. One of the capabilities of PSID is to mix and match different levels of model complexities to study how these can change the conclusions.

This example simulation presents a time-domain simulation of an inverter and compares the results using three different generator models and two distinct network models in a 3 bus system. The simulations use a 19-state grid-supporting virtual synchronous machine (VSM) inverter with average PWM dynamics. The example code is available in the SIIP Examples repository (https://github.com/NREL-SIIP/SIIPExamples.jl) and PSID's documentation.

Figure 2.19 depicts the evolution of the generator's voltage magnitude at bus 2 after a circuit trip connecting the inverter and the infinite bus at $t = 1$s. PSID enables the exploration of several assumptions in the study of the dynamics of the system, for instance:

- In the *Static Lines* network model the relationship between the voltages and currents phasors is algebraic via the admittance matrix $\boldsymbol{i} = Y\boldsymbol{v}$. In the *Dynamic Lines* network model, the relationship is via differential equations, commonly known as dynamic phasor, that allows capture of electromagnetic dynamics:

$$\frac{l}{\Omega_b}\frac{d\boldsymbol{i}_\ell}{dt} = (\boldsymbol{v}_{\text{from}} - \boldsymbol{v}_{\text{to}}) - (r + jl)\boldsymbol{i}_\ell \tag{2.3}$$

$$\frac{c_{\text{from}}}{\Omega_b}\frac{d\boldsymbol{v}_{\text{from}}}{dt} = (i_{\text{in}}^{\text{from}} - i_{\text{out}}^{\text{from}}) - jc_{\text{from}}\boldsymbol{v}_{\text{from}} \tag{2.4}$$

$$\frac{c_{\text{to}}}{\Omega_b}\frac{d\boldsymbol{v}_{\text{to}}}{dt} = (i_{\text{in}}^{\text{to}} - i_{\text{out}}^{\text{to}}) - jc_{\text{to}}\boldsymbol{v}_{\text{to}} \tag{2.5}$$

  where $r, l, c_{\text{from}}, c_{\text{to}}$ are the equivalent π-model line parameters and $\Omega_b = 2\pi f_b$ is the base frequency of the network.

- The 4th-order model is a simplified model with only transient electromotive forces (emfs). The 6th-order model, commonly known as GENROU model (Round Rotor Generator), considers both transient and subtransient emfs, but the stator fluxes dynamics are approximated via algebraic representations. Finally the 8th-order model,
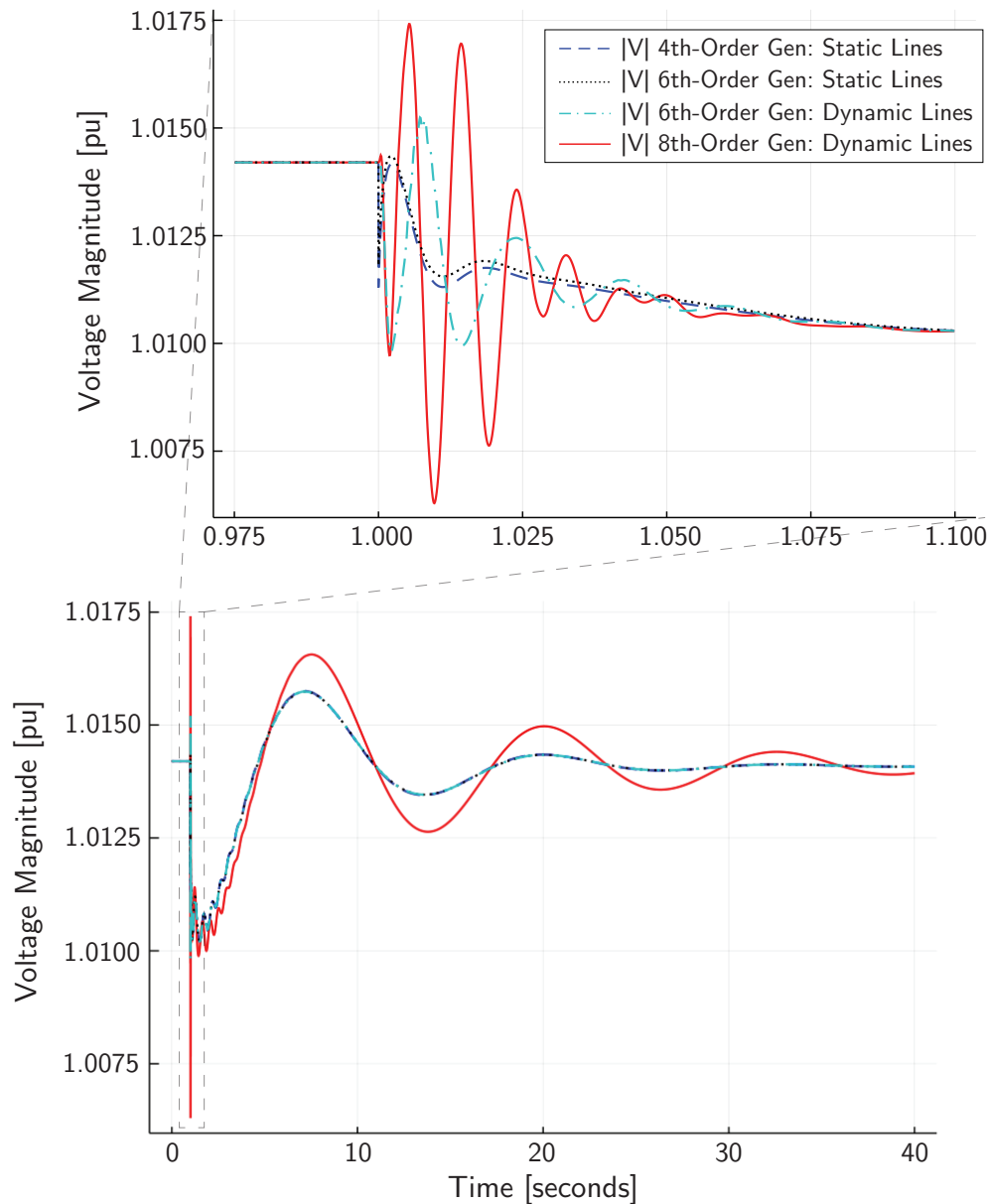
Figure 2.19: Generator bus voltage magnitude $|V|$ for *Example Case A* under different machine and network models for the same perturbation.

known as Marconato model, considers both transient and subtransient electro magnetic fields, with dynamic stator flux representation through differential equations.

Thus, PSID can run an RMS simulation, using a 4th-order or 6th-order model with *Static Lines*, or an EMT simulation using the 8th-order model with *Dynamic Lines*. It is also

possible to combine the 6th-order model (typically used in RMS) with a *Dynamic Lines* model and study such hybrid behavior as depicted in Figure 2.19. As mentioned, this flexibility is one of the core features provided in PSID.

A model with more detail, such as the 8th-order model case, has significantly faster dynamics, as observed in Figure 2.19. The additional modeling detail comes with an extra computational cost. Solving this EMT model requires a time step no larger than 500 μs. The other example RMS simulations only require a time step of 20 ms. This limited example showcases the challenges of making EMT simulations a requirement of power systems in the presence of power electronics converters.

This simple case demonstrates how different model assumptions may change the simulation results. Figure 2.19 shows that additional details from the EMT model furnish an understanding comparable to that provided by simpler or hybrid models. Although this is not a general result, it highlights the possible trade-offs between result details and model complexity.

Example Case B: 14-bus System

An additional objective of PSID is to facilitate the development of study cases for low-inertia systems, similar to traditional RMS benchmark systems. *Example Case B* shows the well-known IEEE 14-bus system with five generators. All the results presented here are also available to the reader as Jupyter Notebooks in the SIIP Examples repository.

Using PSID, we model each generator with a 6th-order machine model, the GENROU model. Additionally, we use an IEEE AC1A Automatic Voltage Regulator (AVR) system and a Gas Steam turbine model (GAST) turbine governor in the slack bus. Quickly switching devices and models is another core feature of PSID. In this example, we conduct two simulations: one with only synchronous machines, and a second case, we replaced the generator located at bus 6 for an aggregated model of a Virtual Synchronous Machine (VSM) grid supporting inverter with 19 states, the same model used in *Example Case A*. This example allows us to explore the effects of substituting synchronous machines with inverter-based generation.

After the system's components are defined, all devices are automatically initialized based on the power flow results. If a feasible point exists, then the system is appropriately initialized and can be used for simulation. Using automatic differentiation, PSID provides small signal information for the operating point, such as eigenvalues, damping of each mode, and participation factors. In this example simulation, we use an admittance matrix formulation for the network model representation.

Figure 2.20 presents a comparison of the eigenvalues (at the operating point) for both systems with and without the inverter, separated in both "fast" and "slow" dynamics. The states are assigned to eigenvalues via their participation factors. This comparison is crucial for understanding the fastest dynamics that could be approximated via an algebraic representation in each simulation.
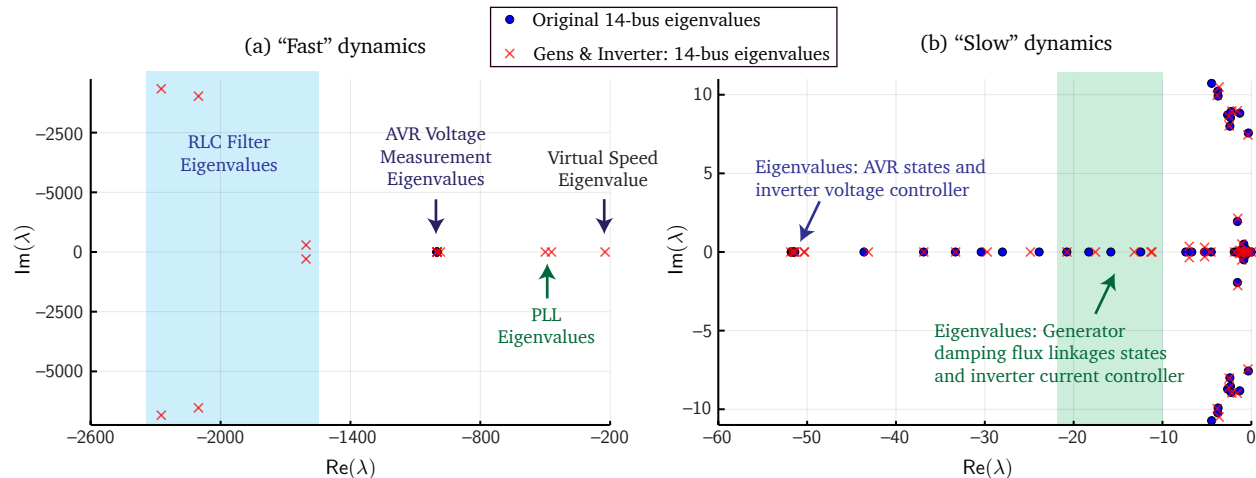
Figure 2.20: Eigenvalues comparison for operating point on both 14-bus system in *Example
Case B*.

As observed in Figure 2.20, electromagnetic dynamics of the RLC filter in the inverter
are the fastest dynamics, and for this operating point could be reasonably neglected in our
study case since they are effectively on different time scale.

Similarly, the low-pass filter model used to measure the bus voltage of the excitation
systems could also be ignored and considered as an ideal measurement. However, based on
this analysis, the inverter eigenvalue associated to the virtual speed and the PLL dynamics
are sufficiently close to the AVR exciter timescale and should be considered in a time
domain simulation. These results highlight the complexity of defining modeling strategies
to study converter and system dynamics interactions.

We perform a time-domain simulation to explore the behavior of the system under a
perturbation. Figure 2.21 depicts the rotor speed of the generator and the virtual speed
of the inverter after an ideal trip of the line connecting buses 2 and 4. As expected, the
dynamics observed in the inverter are faster, but the system manages to converge on a new
stable operating point.

This simplified generator substitution demonstrates that changing generators with con-
verters can significantly impact the dynamic mode interactions. It also shows that there
are opportunities to simplify modeling details to speed-up simulations. However, these
simplifications may require sophisticated approaches to choose model complexity correctly.

The increasing penetration of IBRs will undoubtedly lead to new challenges and op-
portunities in computational power system studies. In this section, we reviewed the main
computational challenges of future low-inertia systems, such as modeling complexity, the
interaction between SM machine controllers and IBR controllers, and numerical time-step
integration requirements. We highlight the importance of Scientific Computing principles to
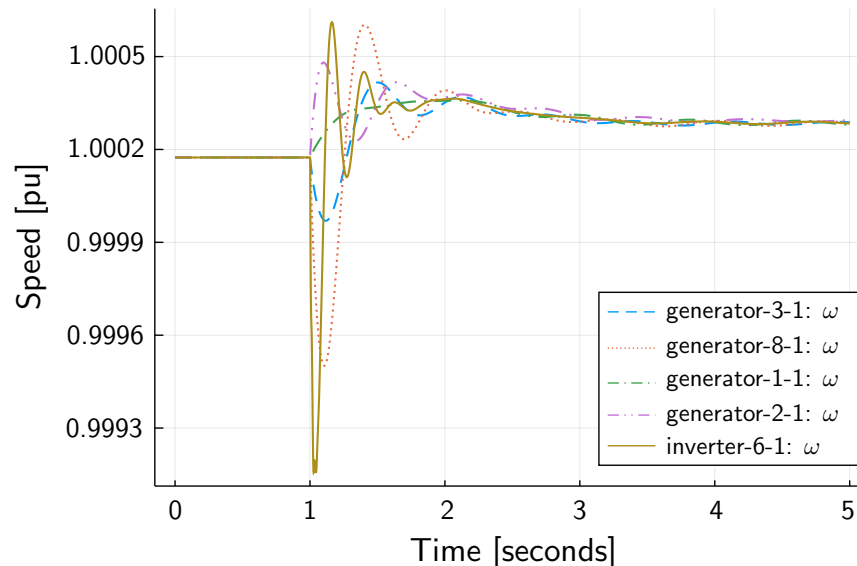
Figure 2.21: Generators' rotor speed and inverter's virtual speed timeseries for *Example Case B* under branch trip between buses 2 and 4.

tackle these issues by enabling *reproducibility* and *validity* of such simulation experiments.

We introduced how the Julia Programming Language is designed to make high-performance computing more accessible and provides reproducibility and scalability tools. In particular, this section presented `PowerSystems.jl` and `PowerSimulationsDynamics.jl`, two Julia packages to tackle new challenges in dynamic modeling while retaining the flexibility to facilitate the implementation of Scientific Computing principles.

Finally, we have presented two simulation cases to highlight the use of these packages to investigate different models and their responses in various settings. We used time-domain simulations and small-signal analysis to study the assumptions in modeling and the converter-system interactions. The two simplified examples highlight the need to re-think the approaches when developing models for power systems' dynamic analysis.

2.4 Grid Forming Small Signal Stability of Line and Voltage Dynamics

Power systems are rapidly integrating large amounts of generation interfaced via power electronics. IBRs replaces rotating machines, decreases system inertia, and alters the dynamics of power system state variables [86, 131].

Currently, most IBRs are connected to power systems operating in grid following mode. Their control relies on measurements of amplitude, phase, and frequency of the grid voltage (typically via a phase-locked loop) to synchronize and inject the current into the grid for

the desired power, i.e., operate in a current source mode [27]. However, these control methods rely on stable voltage and frequency signals to operate correctly. Thus, low inertia grids, and weak voltage regulation capabilities, limit the capability to interconnect new grid-following IBRs [100]. For example, PLL control may present instabilities in weak grids [29], and erroneous frequency measurements following a disturbance can induce converter misoperations [98]. Integrating IBRs operating in grid-forming control modes is an alternative to tackle some of the challenges mentioned above [27]. Grid-forming allows the IBRs to work as synchronized voltage sources, allowing them to function even without synchronous machines present, and maintain the stability of future low/zero-inertia power systems.

Recent work has begun to analyze the interactions of lines and IBRs. In [36] the authors analyze a dispatchable Virtual Oscillator Control (dVOC), a type of grid-forming control. Using Lyapunov stability techniques, the authors show the dVOC's almost global stability when approximating line dynamics. The case of line dynamics effects for droop-control is presented in [136], where a higher-order approximation is proposed as a compromise between a full order model and the first-order approximation. However, the authors neglect the effects of inner-loop controls and shunt capacitance.

In this section, we present a detailed study of the effects of common power system modeling assumptions on grid-forming converter small-signal stability assessments [42]. We use a detailed IBR model connected to an infinite voltage source through a realistic AC interconnection to investigate the system local stability characteristics and transient response.

The main contributions of this section are:

- A demonstration that AC-side dynamics approximations can significantly alter regions of small signal stability for VSM.

- An examination of the impact of modeling approximations on VSM parameter gain tuning. For example we show that the impact reactive power droop on stability is visible only with dynamic line models.

- A brief discussion of the usage of line/voltage dynamics approximations on transient simulations, and a simulation case in which AC-side approximations result in transient responses that are indistinguishable after less than one AC cycle.

Our numerical results show that additional interactions can be expected between IBRs controllers and line dynamics. Hence, traditional modeling assumptions used for line approximations may lead to stability overestimation or inadequate control tuning.

Notation for this section: The complex imaginary unit is represented by $j = \sqrt{-1}$. We denote the rotating reference frame of the network as RI, rotating at a fixed frequency $\omega_s = 1$ p.u. Bold lowercase symbols are used to represent complex variables in the dq or RI reference frames, $\boldsymbol{x} = x_\mathsf{d} + jx_\mathsf{q}$ or $x_R + jx_I$. Bold capital symbols are used to denote complex matrices $\boldsymbol{Y} = G + jB$. Finally, dot notation $\dot{x} = dx/dt$ is used interchangeably.

Modeling of grid-forming inverter and network dynamics

We assume that all electrical quantities in the network are balanced, which allows us to work using dq reference frames via the Park transformation for both the inverters and the grid. The converter is connected to the grid via an RLC filter, an equivalent step-up transformer, and then via a double circuit transmission line at 230 kV as depicted in Figure 2.22, which is a common configuration for large IBR plants.
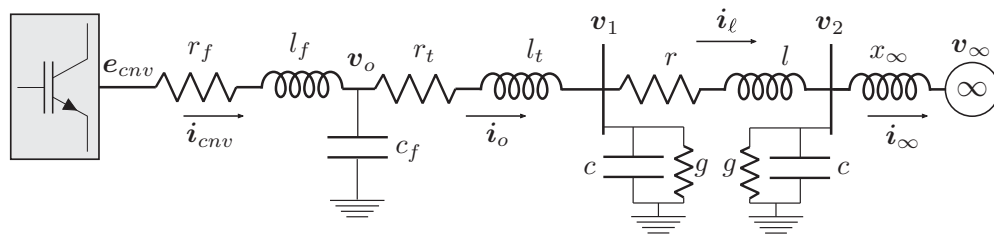
Figure 2.22: One-line diagram for study cases.

Inverter model

The proposed model is based on a VSC grid forming control scheme presented in Figure 2.23 derived from the inverter model used in [26].
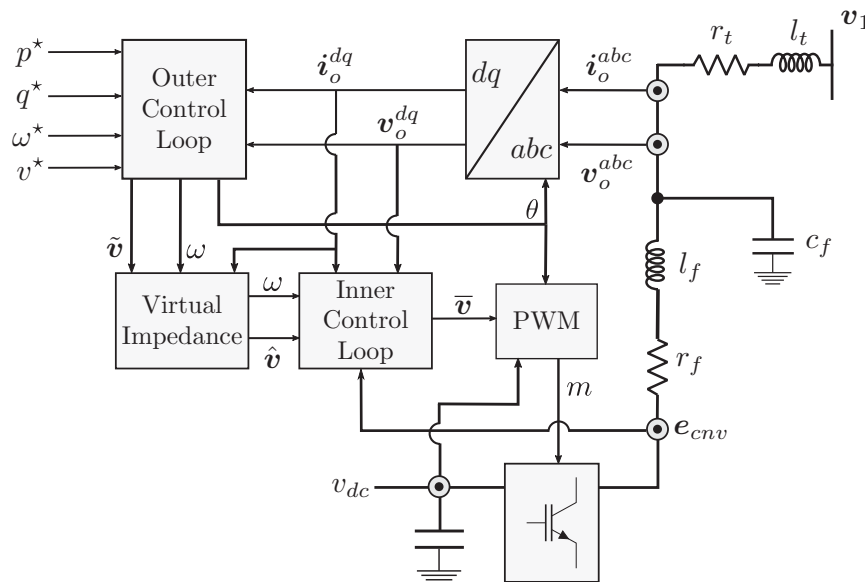
Figure 2.23: VSC grid-forming control scheme.

The grid is already modeled on its own SRF, denoted as RI, rotating at a fixed frequency ω_s. The transformation from grid SRF to the inverter SRF is given by $\boldsymbol{x}_{\mathsf{dq}} = \boldsymbol{x}_{RI}e^{-j\theta}$, where θ is the internal voltage angle displacement of the outer loop control.

- *Outer loop control:* The outer control implements a VSM model. Given the measurements of active and reactive power, computed as $p_e = v_\mathsf{d}i_\mathsf{d} + v_\mathsf{q}i_\mathsf{q}$ and $q_e = -v_\mathsf{d}i_\mathsf{q} + v_\mathsf{q}i_\mathsf{d}$, the control uses a virtual inertia model as described in [78]:

$$\dot{\theta} = \Omega_b(\omega - \omega_s) \tag{2.6}$$

$$\dot{\omega} = \frac{1}{M}\left[(p^\star - p_e) + \frac{1}{k_p}(\omega^\star - \omega)\right] \tag{2.7}$$

The phase angle of the outer loop control is constant under stable steady-state conditions and represents the phase difference between the SRF's of the grid and the inverter. Hence, in equation (2.6), $\omega - \omega_s$ represents the relative speed deviation and θ the corresponding relative phase angle displacement [26]. Equation (2.7) describes the frequency dynamics, considering the inertia term on the active power and the damping over the nominal frequency.

Finally, a traditional droop model with a low-pass filter with cut-off frequency ω_z is used for the voltage regulation:

$$\dot{q}_f = \omega_z(q_e - q_f) \tag{2.8}$$

$$\tilde{v}_d = v^\star + k_q(q^\star - q_f) \tag{2.9}$$

The term $\tilde{\boldsymbol{v}} = \tilde{v}_\mathsf{d} + 0j$ provides the reference signal for the virtual impedance block.

Remark: The traditional power-frequency droop control with a low-pass filter with cut-off frequency ω_z (for active power measurement), has the same steady-state response with the VSM model if $M = 1/(\omega_z k_p)$. Thus, the small signal analysis provided in this paper is also valid for such droop models. However, the VSM control provides a different dynamic response as discussed in [78].

- *Virtual impedance:* As described in [78], the inclusion of a virtual impedance provides an additional block for active stabilization and disturbance rejection via a minor cross-coupling of dq components and a non-zero q-component: $\hat{\boldsymbol{v}} = \tilde{\boldsymbol{v}} - (r_v + j\omega l_v)\boldsymbol{i}_o$. The term $\hat{\boldsymbol{v}}$ provides the reference signal for the inner loop control.

- *Inner loop control:* The inner loop control consists of two cascaded PI controllers, a voltage controller:

$$\dot{\boldsymbol{\xi}} = \hat{\boldsymbol{v}} - \boldsymbol{v}_o \tag{2.10}$$

$$\bar{\boldsymbol{i}} = k_p^v(\hat{\boldsymbol{v}} - \boldsymbol{v}_o) + k_i^v\boldsymbol{\xi} + j\omega_s c_f\boldsymbol{v}_o + k_{ff}^i\boldsymbol{i}_o, \tag{2.11}$$

and a current controller:

$$\dot{\boldsymbol{\gamma}} = \overline{\boldsymbol{i}} - \boldsymbol{i}_{cnv} \tag{2.12}$$

$$\overline{\boldsymbol{v}} = k_p^i(\overline{\boldsymbol{i}} - \boldsymbol{i}_{cnv}) + k_i^i\boldsymbol{\gamma} + j\omega_s l_f \boldsymbol{i}_o + k_{ff}^v \boldsymbol{v}_o, \tag{2.13}$$

The terms $k_p^{v,i}$ and $k_i^{v,i}$ corresponds to the proportional and integral components of the PI
controllers, respectively. The terms $j\omega_s c_f \boldsymbol{v}_o$ and $j\omega_s l_f \boldsymbol{i}_o$ are used to decouple both dq axes
on both controllers. Finally, $k_{ff}^{v,i} \in \{0, 1\}$ is a parameter that is used to enable feed-forward
on the controllers.

• *Converter PWM:* We use an average converter model, that without saturation implies
that:

$$\boldsymbol{e}_{cnv} = \boldsymbol{m} \cdot \frac{v_{dc}}{2} = \frac{\overline{\boldsymbol{v}}}{v_{dc}/2} \cdot \frac{v_{dc}}{2} = \overline{\boldsymbol{v}} \tag{2.14}$$

• *Filter dynamics:* For modeling purposes, it is convenient to compute the filter dynamics
in the inverter SRF. Since $\boldsymbol{v}_1$ is in the network RI reference frame, we use a transformation
to the converter reference frame $\boldsymbol{v}_1^{\text{dq}} = \boldsymbol{v}_1 e^{-j\theta}$, and hence the voltage and current dynamics
are:

$$\frac{l_f}{\Omega_b} \frac{d\boldsymbol{i}_{cnv}}{dt} = [(\boldsymbol{e}_{cnv} - \boldsymbol{v}_o) - (r_f + jl_f\omega_s)\,\boldsymbol{i}_{cnv}] \tag{2.15}$$

$$\frac{l_t}{\Omega_b} \frac{d\boldsymbol{i}_o}{dt} = \left[(\boldsymbol{v}_o - \boldsymbol{v}_1^{\text{dq}}) - (r_t + j\omega_s l_t)\,\boldsymbol{i}_o\right] \tag{2.16}$$

$$\frac{c_f}{\Omega_b} \frac{d\boldsymbol{v}_o}{dt} = [(\boldsymbol{i}_{cnv} - \boldsymbol{i}_o) - j\omega_s c_f \boldsymbol{v}_o] \tag{2.17}$$

Finally, the connection to the grid is performed via the SRF and base power transformation:

$$\boldsymbol{i}_o^{\text{RI}} = \left(\frac{NS_{\text{inv}}}{S_b}\right) \boldsymbol{i}_o e^{j\theta}, \tag{2.18}$$

on which S_{inv} is the AC power base of the inverter, S_b is the system power base and N the
number of inverters connected in parallel. With that, the 13 inverter states for the VSM
model are given by:

$$\vec{\boldsymbol{x}}_c = \left[\boldsymbol{v}_o, \boldsymbol{i}_o, \boldsymbol{i}_{cnv}, \boldsymbol{\xi}, \boldsymbol{\gamma}, q_f, \theta, \omega\right]^\top \tag{2.19}$$

Considering line current and voltage voltage dynamics, described in the next subsection,
the ODE problem with 19 states is:

$$\vec{\boldsymbol{x}} = \left[\boldsymbol{v}_1, \boldsymbol{v}_2, \boldsymbol{i}_\ell, \vec{\boldsymbol{x}}_c\right]^\top \tag{2.20}$$

Remark: Note that in this model, an inverter model represents N equivalent inverters
connected in parallel as depicted in equation (2.18). Since all parameters of the inverter
are in their respective per-unit, those values stay the same (in per-unit) when the total base
power NS_{inv} is scaled up, maintaining their dynamics, but pushing more current into the
grid. This allows us the scalability of the equivalent inverter, similar to that presented in
[74] when working with physical units.

Network model

Considering a π-line as depicted in Figure 2.22, the current and voltage dynamics are represented by the following differential equations:

$$\frac{\ell}{\Omega_b}\frac{d\boldsymbol{i}_\ell}{dt} = [(\boldsymbol{v}_1 - \boldsymbol{v}_2) - (r + j\omega_s l)\boldsymbol{i}_\ell] \tag{2.21}$$

$$\frac{c}{\Omega_b}\frac{d\boldsymbol{v}_1}{dt} = \left[(\boldsymbol{i}_o^{\mathrm{RI}} - \boldsymbol{i}_\ell) - (g + j\omega_s c)\boldsymbol{v}_1\right] \tag{2.22}$$

$$\frac{c}{\Omega_b}\frac{d\boldsymbol{v}_2}{dt} = [(\boldsymbol{i}_\ell - \boldsymbol{i}_\infty) - (g + j\omega_s c)\boldsymbol{v}_2] \tag{2.23}$$

where Ω_b is the system's base frequency ($2\pi 60$ rad/s), and current provided into the infinite bus $\boldsymbol{i}_\infty$ is computed algebraically as $\boldsymbol{i}_\infty = (\boldsymbol{v}_2 - \boldsymbol{v}_\infty)/(jx_\infty)$. All values in the line model are in the system's per-unit, hence current outputs must be re-scaled from the inverter base to the system base as described in equation (2.18), while considering the SRF transformation.

AC side dynamics approximations

In power systems literature, it is *customary* to make approximations of line dynamics for stability analysis. These include neglecting capacitance and the resulting voltage dynamics in short-length lines due to the small value of the current drawn from the shunt impedance [63]. For medium-length lines, voltage dynamics are approximated via algebraic relationships using zero-order approximations. Results in [117, 116] show that the model used in transient simulations for modeling current flows over the network via the admittance matrix $\boldsymbol{Y}$ is a reasonable approximation of integral manifold, and under certain conditions and $r_{\mathrm{branch}} = 0$, the approximation is exact. The validity of these approximations is based on time-scale separation arguments derived from singular perturbation analysis of the power system dynamics [18]. These approximations have been justified in practical terms as they improve computational performance in large transient simulation studies. Zero-order approximations have also been shown to be valid for small signal analysis and are typically used for studying intra and inter-area electromechanical oscillations, and stabilizer parameter tuning [116].

The line and voltage zero-order approximation consists of setting the left-hand side of (2.21)-(2.23) to zero under the assumption that the constants multiplying the differential terms are sufficiently small to adequately approximate the integral manifold. Under this assumption, we obtain the algebraic map $\vec{\boldsymbol{i}} = \boldsymbol{Y}\vec{\boldsymbol{v}}$, the standard current-injection model:

$$\begin{bmatrix} \boldsymbol{i}_o^{\mathrm{RI}} \\ -\boldsymbol{i}_\infty \end{bmatrix} = \begin{bmatrix} y_\ell + y_c & -y_\ell \\ -y_\ell & y_\ell + y_c \end{bmatrix}\begin{bmatrix} \boldsymbol{v}_1 \\ \boldsymbol{v}_2 \end{bmatrix} \tag{2.24}$$

where $y_l = \frac{1}{r+j\omega_s l}$ and $y_c = g + j\omega_s c$. These algebraic equations allow us to compute $\boldsymbol{v}_1$ and $\boldsymbol{v}_2$. Note that these equations can also be used to approximate the filter AC dynamics (2.15)-(2.17).

As discussed in [18], the accuracy of the reduced order model depends on the term that multiplies the derivative (ℓ/Ω_b and c/Ω_b in (2.21)-(2.23)) and its proximity to zero. This approximation error is typically observed in the dynamic response of the system over a disturbance near time zero [117].

If line current and voltage dynamics are approximated, the state space is reduced by six states for the voltages and currents and additional algebraic equations must be included $\vec{y} = \begin{bmatrix} v_1, v_2, i_\ell \end{bmatrix}^\top$ and the differential states are simply $\vec{x}_c$. The simplification defines a Differential-Algebraic system of Equations (DAE). If both lines and filter dynamics (that is the entire AC side) are also approximated, then 12 algebraic states $\vec{y} = [v_1, v_2, i_\ell, v_0, i_0, i_{cnv}]^\top$ must be considered with only seven remaining states for the inverter.

Discussion on Singular Perturbation Theory

Singular Perturbation Theory (SPT) has been extensively used in Power Systems and Control Systems to reduce the order of a dynamical model or provide a simplification of such models.

In general, singular perturbation refers to finding solutions, typically roots of a set of equations or trajectories of a dynamical system, that depends on a parameter ε. We say that a problem is *regularly perturbed* if all solutions $f(x, \varepsilon)$ converge uniformly as $\varepsilon \to 0$. If there is at least one solution which does not converge uniformly, then the problem is called *singularly perturbed*. The importance is that the category, *regular* or *singular*, depends on the **solutions**, and **not** the equations.

Example: Consider the problem of finding the roots of the following polynomial:

$$\varepsilon z^8 - z^3 - 1 = 0$$

Here, numerical computations to obtain the roots as $\varepsilon \to 0$, show that 3 roots converge to the cubic roots of -1, while the other five roots diverge as we push ε to zero. Thus, the problem of finding of the roots of the previous equation as $\varepsilon \to 0$ is *singular*.

Note that in ODE systems, the process of finding the trajectories by setting $\varepsilon \to 0$ via singular perturbation, typically results in solutions that do not converge to the same trajectory, although it could be that it converges for some domain in time, for example when the fast states already converged.

The book from Kokotovic, Khalil and O'Reilly [60] provides the foundation of SPT for engineering applications, on which we based the discussion of this subsection.

Standard Formulation on SPT

The main formulation for SPT provides two types of states, $x \in \mathbb{R}^n$ for "slow" states and $z \in \mathbb{R}^m$ for "fast" states, that are multiplied by a small positive scalar ε:

$$\dot{x} = f(x, z, \varepsilon, t), \quad x(t_0) = x^0, \quad x \in \mathbb{R}^n \tag{2.25a}$$

$$\varepsilon \dot{z} = g(x, z, \varepsilon, t), \quad z(t_0) = z^0, \quad z \in \mathbb{R}^m \tag{2.25b}$$

The previous model is already directed towards a reduced-order modeling, via a singular parameter perturbation by setting $\varepsilon = 0$, which reduces the order of the system from $n + m$ to n since equation (2.25b) reduces to an algebraic equation:

$$0 = g(\bar{x}, \bar{z}, 0, t). \tag{2.26}$$

Here, the bar notation for the variables now refer to a system with $\varepsilon = 0$. The following assumption is necessary for the previous model to be in *standard form*:

Assumption 1 *Model* (2.25a)-(2.25b) *is in* standard form *if and only if equation* (2.26) *in a domain of interests (of the states) has* $k \geq 1$ *distinct ("isolated") real roots:*

$$\bar{z} = \bar{\phi}_i(\bar{x}, t), \quad i = 1, 2, \ldots, k \tag{2.27}$$

This assumption is typically stated in all formulations of SPT, and ensures that a well-defined n-dimensional reduced model will correspond to each root (2.27). To obtain the reduced model we simply substitute (2.27) in (2.25a):

$$\dot{\bar{x}} = f(\bar{x}, \bar{\phi}_i(\bar{x}, t), 0, t), \quad \bar{x}(t_0) = x^0 \tag{2.28}$$

Re-writing everything in a new function $\bar{f}$, we can rewrite our previous equation as:

$$\dot{\bar{x}} = \bar{f}(\bar{x}, t), \quad \bar{x}(t_0) = x^0 \tag{2.29}$$

the so-called *quasi-steady-state model*, since z, whose velocity is $\dot{z} = g/\varepsilon$, can be large when ε is small, that may rapidly converge to a root of (2.27).

• *Example on Generator modeling:* Consider the 8th-order balanced Sauer-Pai model in per-unit [85]:

$$\left(\frac{1}{\Omega_b}\right)\dot{\delta} = \omega - \omega_s \tag{2.30a}$$

$$(2H)\dot{\omega} = \tau_m - \tau_e - D(\omega - \omega_s) \tag{2.30b}$$

$$(T'_{d0})\dot{e}'_q = -e_q - (x_d - x'_d)(i_d - \gamma_{d2}\psi''_d - (1 - \gamma_{d1})i_d + \gamma_{d2}e'_q) + v_f \tag{2.30c}$$

$$(T'_{q0})\dot{e}'_d = -e_d + (x_q - x'_q)(i_q - \gamma_{q2}\psi''_q - (1 - \gamma_{q1})i_q - \gamma_{d2}e'_d) \tag{2.30d}$$

$$(T''_{d0})\dot{\psi}''_d = -\psi''_d + e'_q - (x'_d - x_\ell)i_d \tag{2.30e}$$

$$(T''_{q0})\dot{\psi}''_q = -\psi''_q - e'_d - (x'_q - x_\ell)i_q \tag{2.30f}$$

$$\left(\frac{1}{\Omega_b}\right)\dot{\psi}_d = r_a i_d + \omega\psi_q + v_d \tag{2.30g}$$

$$\left(\frac{1}{\Omega_b}\right)\dot{\psi}_q = r_a i_q - \omega\psi_d + v_q \tag{2.30h}$$

on which the time constants have been included on the left-hand side of the differential equations.

Equations for the rotor angle and speed, δ and ω, (2.30a) and (2.30b), model the electro-mechanical transformation in the rotor. Here, the angle δ is in radians, and the rotor speed ω is in per-unit. The base frequency $\Omega = 2\pi f \approx 377$ rad/s for a 60 Hz system, implies that $\Omega_b^{-1} \approx 2 \cdot 10^{-3}$. The synchronizing speed ω_s is usually equal to 1.0 per unit.

Equation (2.30c) models the *transient* dynamics of the DC field winding, while (2.30d) models the *transient* dynamics of rotor-core induced current (usually from one-q winding). The value for T'_{d0} is usually on the order of $4 \sim 8$ seconds, while the value for T'_{q0} on the order of $10^{-1} \sim 1$ seconds.

Equation (2.30e) models the *subtransient* dynamics of the d-damper winding, while (2.30f) models the *subtransient* dynamics of another q-damper winding. The values for T''_{d0} and T''_{q0} are usually on the order of $10^{-2} \sim 10^{-1}$ seconds.

Finally, equations (2.30g) and (2.30h) are the stator electrical equations that link the voltage to currents and magnetic fluxes. The value of the frequency base is $\Omega_b^{-1} \approx 2 \cdot 10^{-3}$ for a 60 Hz system.

From this model, it is possible to obtain simplified models by using singular perturbation theory with other engineering assumptions. The first approximation used yields the 6th-order model, that is done by making zero the left-hand side of the stator fluxes equations (2.30g) and (2.30h). This usually presented as $\dot\psi_d = \dot\psi_q = 0$, since neglecting $\Omega_b^{-1} = 0$, would imply that the dynamics of the angles (2.30a) should be ignored, that is not possible to do. With the previous assumption, it is possible to eliminate the stator fluxes states. An important distinction here is that, assuming $\dot\psi_d = \dot\psi_q = 0$ does **not** imply that the stator fluxes remains fixed, and they are simply updated via their algebraic equation. That is, the simplification is done assuming the approach used in SPT by making $\Omega_b^{-1} = 0$.

On other approximations, singular perturbation may or not be used, and relies more on engineering observations to obtain more simplified models. For example, the 5th-order model uses that $T'_{q0} = 0$ and $x'_q = x_q$ to the elimination of e'_d dynamics. While, the 4th-order model uses $T'_{d0} = T'_{q0} = 0$ to eliminate the ψ''_d and ψ''_q states. Finally the 2nd-order classical model, eliminates all *transient* and *subtransient* dynamics and consider e'_q as a fixed constant.

Time-scale properties

As mentioned, the slow response or the *quasi-steady-state* is approximated by the reduced model (2.29). A key difference for z is that the fast states z, that should start at t_0 from a prescribed z^0, our approximation defined by (2.27) is not free for $\bar z$ and there may be a large discrepancy between its initial value:

$$\bar z(t_0) = \bar\phi(\bar x(t_0), t_0) \neq z^0 \tag{2.31}$$

Thus, $\bar{z}$ cannot be a uniform approximation of z. The best we can expect is that the
approximation:

$$z = \bar{z}(t) + O(\varepsilon) \tag{2.32}$$

will hold on an interval excluding t_0, that is for $t \in [t_1, T]$, where $t_1 > t_0$. The approximation
for x will be uniform, since we can enforce to start $\bar{x}(t_0) = x^0$ from the original system:

$$x = \bar{x}(t) + O(\varepsilon) \quad t \in [t_0, T] \tag{2.33}$$

Boundary layer

The previous approximation (2.32) showcase that during an initial interval $[t_0, t_1]$, the so-
called *boundary layer*, the original variable z approaches $\bar{z}$, and then during $[t_1, T]$, it will
remain close to $\bar{z}$. The question that we are interested in answering in SPT is: Will z **escape
to infinity** during this transient or **converge to** its quasi-steady-state $\bar{z}$?

To study this, we define our fast time-scale τ as:

$$\tau = \frac{t - t_0}{\varepsilon}, \quad \tau = 0 \text{ when } t = t_0 \tag{2.34}$$

and hence

$$\frac{dz}{d\tau} = \varepsilon \frac{dz}{dt} \tag{2.35}$$

In addition, while z and τ change almost instantaneously, the slow-states x remain very
near its initial value x^0. To describe the behavior of z as a function of τ, we use the so-called
boundary layer correction: $\hat{z} = z - \bar{z}$, that satisfies the "boundary layer system":

$$\frac{d\hat{z}}{d\tau} = g(x^0, \hat{z}(\tau) + \bar{z}(t_0), 0, t_0) \tag{2.36}$$

with the initial condition $\hat{z}(0) = z^0 - \bar{z}(t_0)$, and using x^0 and t_0 as fixed parameters.

The solution $\hat{z}(\tau)$ of this initial value problem is used as a "boundary layer" correction
of (2.32):

$$z = \bar{z}(t) + \hat{z}(\tau) + O(\varepsilon) \tag{2.37}$$

In this representation, $\bar{z}$ is the slow transient of z, while $\bar{z}$ is the fast transient of z. Then
for (2.37) to converge, after a short period, to the slow approximation (2.32), we require
that $\hat{z}(\tau)$ must decay to an $O(\varepsilon)$ as $\tau \to \infty$. In the slow time scale t, this is rapid since:

$$\frac{d\hat{z}}{d\tau} = \varepsilon \frac{d\hat{z}}{dt}$$

The stability properties of (2.36), which are crucial for the approximation to hold, are
stated in the following two assumptions:

Assumption 2 (As. 3.1 in [60]) *The equilibrium $\hat{z}(\tau) = 0$ of (2.36) is asymptotically stable uniformly in x^0 and t_0, while $z^0 - \bar{z}(t_0)$ (the initial condition of the boundary layer system) belongs to its domain of attraction, so $\hat{z}(\tau)$ exists for $\tau \geq 0$.*

Obviously if this assumption is satisfied then

$$\lim_{\tau \to \infty} \hat{z}(\tau) = 0$$

uniformly in x^0, t_0. That is, z will come close to its quasi-steady-state $\bar{z}$ at some time $t_1 > t_0$.

In addition, to ensure that z stays close to $\bar{z}$, we think that as if any instant $t \in [t_1, T]$ (i.e. after $\hat{z}$ already decayed) can be the initial instant, and make the following assumption of the linearization of the boundary layer system (2.36):

Assumption 3 (As. 3.2 in [60]) *The eigenvalues of the Jacobian $\partial g / \partial z$ evaluated along $\bar{x}(t), \bar{z}(t)$ (and for $\varepsilon = 0$), have real parts smaller than a fixed number:*

$$\text{Re } \lambda \left\{ \frac{\partial g}{\partial z} \right\} \leq -c < 0 \tag{2.38}$$

Assumptions 2 and 3 both describe a strong stability property of the boundary layer system (2.36). If z^0 is assumed to be sufficiently close to $\bar{z}(t_0)$, then Assumption 3 encompasses Assumption 2, since the linearization result is sufficient to ensure that $z^0 - \bar{z}(t_0)$ will go to zero. In addition, result (2.38) means that the Jacobian is nonsingular, which implies that the root $\bar{z}(t)$ is distinct, as required by Assumption 1.

Theorem 1 (Tikhonov's Theorem) *If Assumptions 2 and 3 are satisfied, then the approximation (2.33), (2.37) is valid for all $t \in [t_0, T]$, and there exists $t_1 \geq t_0$, such that (2.32) is valid for all $t \in [t_1, T]$.*

Analysis on Linear Time Invariant (LTI) systems

Consider a LTI system, that could come after a linearization of our non-linear system in an operating point:

$$\dot{x} = A_{11}x + A_{12}z + B_1 u, \quad x \in \mathbb{R}^n, u \in \mathbb{R}^r \tag{2.39a}$$
$$\varepsilon \dot{z} = A_{21}x + A_{22}z, \quad z \in \mathbb{R}^m \tag{2.39b}$$

with $x(t_0) = x^0$ and $z(t_0) = z^0$. We are interested in decoupling the system via a similarity transformation. By doing the change of variables:

$$\eta(t) = z(t) + L(\varepsilon)x(t) \tag{2.40}$$

we obtain:

$$\dot{x} = (A_{11} - A_{12}L)x + A_{12}\eta \tag{2.41a}$$

$$\varepsilon\dot{\eta} = R(L, \varepsilon)x(t) + (A_{22} + \varepsilon L A_{12})\eta \tag{2.41b}$$

by imposing $R(L, \varepsilon) = 0$ we can decouple the system. This is equivalent to imposing:

$$R(L, \varepsilon) = A_{21} - A_{22}L + \varepsilon L A_{11} - \varepsilon L A_{12}L = 0 \tag{2.42}$$

a matrix equation to solve for $L \in \mathbb{R}^{m \times n}$. If this is satisfied, the system is written in the so-called *actuator form* in which the fast states η drive the slow states x.

Lemma 1 *If A_{22} is invertible (nonsingular), there is an $\varepsilon^* \geq 0$ such that $\forall \varepsilon \in [0, \varepsilon^*]$, there exists a solution $L(\varepsilon)$ to the matrix equation (2.42), which is approximated to:*

$$L(\varepsilon) = A_{22}^{-1}A_{21} + \varepsilon A_{22}^{-2}A_{21}A_0 + O(\varepsilon^2) \tag{2.43}$$

where

$$A_0 = A_{11} - A_{12}A_{22}^{-1}A_{21} \tag{2.44}$$

Note that for $\varepsilon = 0$, we have $L(0) = A_{22}^{-1}A_{21}$ and hence the dynamics for x are:

$$\dot{x} = A_{11} - A_{12}Lx + A_{12}\eta = A_0 x + A_{12}\eta \tag{2.45}$$

while for η we have:

$$0 = A_{22}\eta$$

and since A_{22} is invertible, that implies that $\eta(t) = 0$ for $\varepsilon = 0$, and hence the dynamics for x are:

$$\dot{\bar{x}} = A_0 x \tag{2.46}$$

This is the so-called zero-order singular perturbation approximation for the slow-states. The A_0 is the so-called *reduced Jacobian* for non-linear DAE systems that are approximated around a point of operation. The approximation for L in (2.43) is valid for all ε in a certain range that will depend on the norm of the matrices A_{ii} [60].

Eigenvalue Properties of LTI systems

For the LTI system in actuator form (i.e. block triangular), the characteristic equation is given by:

$$\psi(s, \varepsilon) = \frac{1}{\varepsilon^m}\psi_s(s, \varepsilon)\psi_f(p, \varepsilon) \tag{2.47}$$

where ψ_s and ψ_f are the characteristic equations for the slow and fast states respectively:

$$\psi_s(s, \varepsilon) = \det[sI_n - (A_{11} - A_{12}L)] \tag{2.48a}$$

$$\psi_f(p, \varepsilon) = \det[pI_m - (A_{22} + \varepsilon L A_{12})] \tag{2.48b}$$

For the fast-states these are computed in the high-frequency scale $p = \varepsilon s$. Thus, for the original LTI system, the first n eigenvalues are the roots of the characteristic equation $\psi_s(s, \varepsilon) = 0$, while the remaining m eigenvalues are:

$$\lambda_i = \frac{\pi_j}{\varepsilon}, \quad i = n + j, \ j = 1, \ldots, m \tag{2.49}$$

where π_j are the roots of the fast characteristic equation $\psi_f(p, \varepsilon) = 0$.

Note that, for $\varepsilon = 0$, the slow eigenvalues λ_i are the ones given by the matrix $A_0 = A_{11} - A_{12}A_{22}^{-1}A_{21}$, while the eigenvalues π_j for the fast states, in the high frequency scale, are the eigenvalues of the matrix A_{22}. How good is this approximation of the eigenvalues of the original system as $\varepsilon \to 0$ is provided in the following theorem:

Theorem 2 (Th. 3.1 in [60]) *If A_{22}^{-1} exists, then as $\varepsilon \to 0$, the first n slow eigenvalues of the original system* (2.39) *tend to fixed position in the complex plane defined by the eigenvalues of A_0, while the remaining m fast eigenvalues tend to infinity, with the rate $1/\varepsilon$, along asymptotes defined by the eigenvalues of A_{22}, namely:*

$$\frac{1}{\varepsilon}\lambda_j(A_{22}), \quad i = n + j, \ j = 1, \ldots, m \tag{2.50}$$

Moreover, if the n eigenvalues of $\lambda_i(A_0)$ are distinct and the m eigenvalues of $\lambda_j(A_{22})$ are distinct, where $\lambda_i(A_0) = \lambda_j(A_{22})$ is allowed, then the eigenvalues of the original system (2.39) are approximated as:

$$\lambda_i = \lambda_i(A_0) + O(\varepsilon), \quad i = 1, \ldots, n \tag{2.51a}$$

$$\lambda_i = \frac{1}{\varepsilon}\left[\lambda_j(A_{22}) + O(\varepsilon)\right], \quad i = n + j, \ j = 1, \ldots, m \tag{2.51b}$$

Corollary 1 (Co. 3.1 in [60]) *If A_{22}^{-1} exists, and if A_0 and A_{22} are Hurwitz (all eigenvalues on the strict left-half plane), then there exists $\varepsilon^* > 0$ such that $\forall \varepsilon \in (0, \varepsilon^*]$, the original system* (2.39) *is asymptotically stable.*

This allow us to infer the stability of the original system (2.39) by studying the stability of lower-order system A_0 and A_{22} in separate time-scales is crucial for practical analysis and design.

For our study case in VSM stability with line dynamics, the reduced variables via SPT are linearized in a operating point, and define the matrix A_{22}, which we assume is not singular, and we can eliminate the algebraic variables to obtain the reduced Jacobian A_0 that defines our reduced system for the differential variables on which we can compute its eigenvalues to analyze local stability. Simulation cases are presented in the next subsection.

Simulation Studies

Simulations are performed using the Julia programming language. `PowerSystems.jl` and `ModelingToolkit.jl` packages are used to construct the dynamical system and perform fast jacobian evaluations [69, 76]. The VSM model was then implemented in `Power-SimulationsDynamics.jl` for future studies in larger systems. All the code and experiments are available in our public repository, with available interactive Jupyter Notebooks at https://github.com/Energy-MAC/InverterDynamicLinesModels.

Parameters of the 2.75 MVA inverter are obtained from [26]. The line parameters per kilometer are taken from [63] for a typical 230 kV overhead line and has been adapted to represent a double circuit which is a more common interconnection configuration for large power plants. The equivalent formulation of the π-model is used to obtain the parameters. If ℓ is the length of the line in kilometers, and $\boldsymbol{z}_{\mathrm{km}} = r_{\mathrm{km}} + jx_{\mathrm{km}}$ is the series impedance per kilometers and $\boldsymbol{y}_{\mathrm{km}} = g_{\mathrm{km}} + jb_{\mathrm{km}}$ is the shunt admittance per kilometers, then the equivalent parameters (in natural units) of the π-circuit are computed as:

$$\boldsymbol{z} = \boldsymbol{z}_{\mathrm{km}}\ell \left(\frac{\sinh(\gamma\ell)}{\gamma\ell} \right) \qquad \boldsymbol{y} = \frac{\boldsymbol{y}_{\mathrm{km}}\ell}{2} \left(\frac{\tanh(\gamma\ell/2)}{\gamma\ell/2} \right)$$

where $\gamma = \sqrt{\boldsymbol{z}_{\mathrm{km}}\boldsymbol{y}_{\mathrm{km}}}$ is the propagation constant [63]. Finally, the parameters of the equivalent π-circuit are converted to per-unit assuming using 230 kV base voltage (phase-to-phase) and 100 MVA base power, to obtain the final values of r, l, g and c.

Case 1: Line length effects

To access the impact of modeling approximations on the location of eigenvalues, we use three models. We use *DynamicLines* to denote the full ODE formulation, *AlgebraicLines* to denote the algebraic map from equations (2.21)-(2.23), and *FullAlgebraic* by setting lines (2.21)-(2.23) and filter (2.15)-(2.17) dynamics as algebraic maps.

Figure 2.24 depicts the root locus of the eigenvalues, λ, when increasing the line length ℓ from 100 to 400 km, for an equivalent model of 50 VSM inverters ($N = 50$) at $p^{\star} = 1$ p.u. Only the eigenvalues associated to the inverter internal states, obtained via its participation factors, are shown.

As observed, most of the eigenvalues are close to each other across the three models. The eigenvalues associated with $\boldsymbol{\gamma}, \theta, \omega$ and q_f, stay mostly in place through the parameter sweep. On the contrary, the eigenvalues associated with the integrator state of the voltage controller $\boldsymbol{\xi}$, move significantly. In particular, it is observed that the *DynamicLines* case move in a different direction of the other two approximated models. Although this result seems to indicate that such a difference will increase when the line length is increased, we have conducted the analysis up to the practical limit of 400 kilometers dictated by the St. Clair curve for the 230 kV line [63]. These differences in the eigenvalues location will impose differences in parameter tuning as showcased in the following study case.
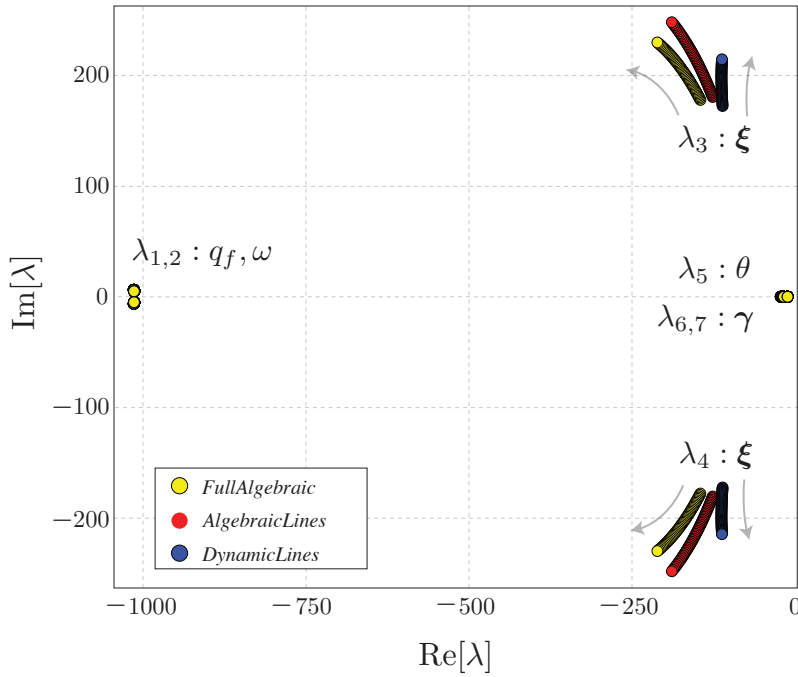
Figure 2.24: Root locus for three models when increasing the line length.

Case 2: Outer control effects

In this section we explore the effect on the small signal stability region by varying the active
and reactive power droops on the three different line/voltage approximations presented in
Case 1, for a length of $\ell = 100$ km. For this case we explore two scenarios. We consider
the equivalent model of 50 VSM inverters in parallel ($N = 50$) operating with a setpoint
of $p^\star = 1$ p.u. Figure 2.25a depicts the stability regions for this case. The second scenario
explores the equivalent model of $N = 100$ operating with a setpoint $p^\star = 0.5$. That is,
both scenarios provide the same power to the grid, 137.5 MW, but over different operating
points. The stability regions of this scenario are depicted in Figure 2.25b.

Figues 2.25a and 2.25b show that, due to presence of the infinite bus and high x/r
ratio of the filter and lines, the reactive power droop k_q has a minor effect on the stability
regions. The nominal operating point is 2% droop in per-unit ($k_p = k_q = 0.02$) as shown
in the figures, and hence the stability limits observed for k_q are further above the typical
values. However, the full algebraic model for the AC side yields *no* upper limit for the
stability on k_q when the system is in a stable region due to the active power droop k_p.

Figues 2.25a and 2.25b also show that, similar to the results presented in [136], the
upper bound for the stability on the active power droop that is more conservative in the
full dynamic model. This showcases that when tuning droop gains, it is crucial to fully
model AC side dynamics to ensure stability that could be not detected in line and voltage
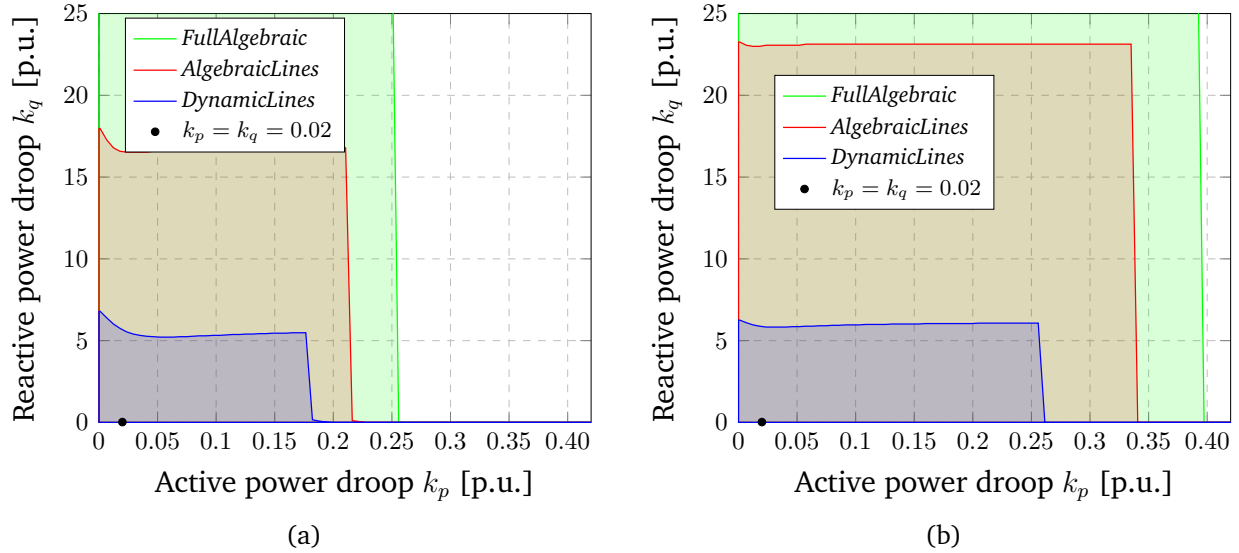
Figure 2.25: Small signal stability regions comparison for active/reactive power droop sweep with (a) $N = 50$ and $p^\star = 1$ p.u. (137.5 MW), and (b) with $N = 100$ and $p^\star = 0.5$ p.u. (137.5 MW).

approximations. However, it is important to note that in both scenarios of this study case, all three regions have enough room to move the active power droop to even 15%.

Finally, the operating point plays an important role in these regions. The stability regions on Figures 2.25a and 2.25b are not the same due to the difference on the operating points. Although, in both scenarios the total active power injected to the grid is the same, the stability region is narrower in the equivalent model operating at $p^\star = 1$ p.u.

Case 3: Inner control effects

Similar to the outer control study case, we explore the effect on the stability due to the gains of both voltage and current controllers. Contrary to the outer loop control, the root locus for the inverter eigenvalues does not show signs of instability when these gains are swept individually between 10% to 10 times their nominal values for an equivalent model of $N = 50$ with $p^\star = 1$ p.u. Figure 2.26 showcase the root locus of the eigenvalues associated to the inverter states for increasing the current controller proportional gain k_p^i. Eigenvalues $\lambda_{1,2}$ associated with ω and q_f are omitted since mostly remain fixed around $\lambda_{1,2} \approx -1000$ (see Figure 2.24). Similar to the previous cases, there are differences in the specific location for the eigenvalues, but the direction of movement is similar between the three models, showcasing a similar small signal response for the three proposed models. Both eigenvalues $\lambda_{6,7}$ move towards zero when $k_p^i \to \infty$, but remaining on the left half-plane. Similar plots for parameter sweep of other inner control gains can be found in the public repository, that
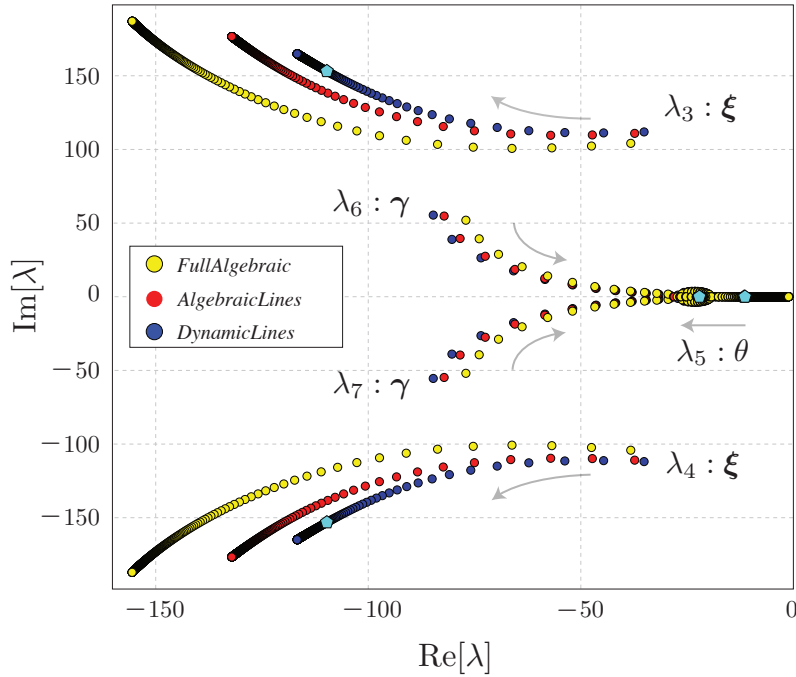
Figure 2.26: Root locus for three models when sweeping over k_p^i. Eigenvalues for nominal parameters of the *DynamicLines* model are depicted in cyan.

showcase a similar response that do not showcase small signal stability issues, independent of the network model.

Case 4: Transient Simulations

As discussed in [117, 60], the improved accuracy of higher order models is relevant when the time constants on the left-hand side of line/voltage equations are close to zero. We explore the voltage at the inverter's terminal $|v_o|$ for a line trip in the double circuit (doubling its impedance). The line considered has a length of 100 km, with an equivalent inverter model of $N = 50$ operating at $p^\star = 0.5$ p.u. Figure 2.27 depicts the evolution of the voltage for the three proposed models under this disturbance. In order to minimize the effects of the numerical integrator in the result, the maximum step size dtmax was set to 10^{-4}. The simulation used the solver GRK4T.

Results show that the dynamic approximations do not significantly alter the transient response simulation. Differences in the transient response between the full order and the zero-order approximations decay after the first 20 ms, suggesting that in this case the algebraic approximations are valid. This highlights our previous discussion on convergence of the fast states in SPT analyses. Here, the voltage $|v_o|$ here is one of these fast-states that is approximated in the *FullAlgebraic* representation. After the fault, in the *FullAlgebraic*
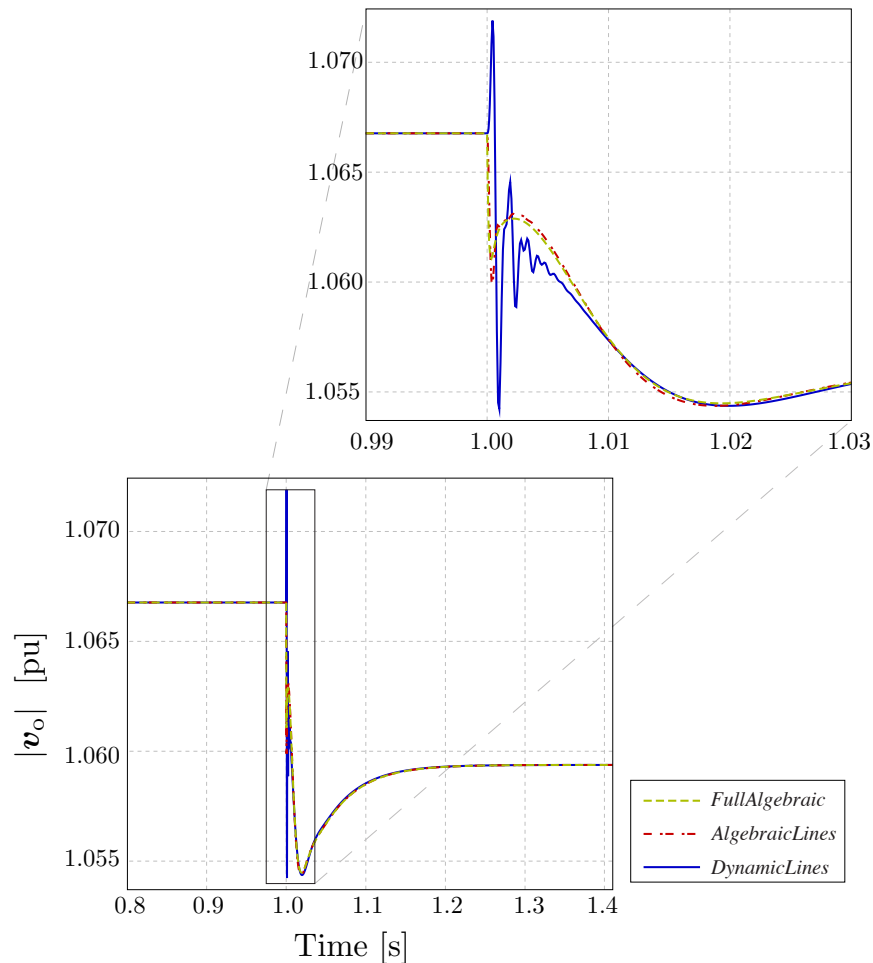
Figure 2.27: Voltage magnitude $|\boldsymbol{v}_o|$ after a single circuit fault at $t = 1$ s.

representation, the *quasi-steady-state* voltage $\bar{z}$ immediately must be reinitialized to other point, while in the *DynamicLines* representation, the voltage z is free to start on the specified condition. Observe that, after 20 ms, the quasi-steady-state approximation almost match the full model representation, and can be considered our $t_1 = 1.02$ (that is greater than $t_0 = 1.0$) on which our approximation is uniform for z.

An important aspect is that, after the fault, **we must ensure that the assumption of distinct roots is satisfied**. We do not verify this, and rely to the *re-init* procedure implemented in DAE numerical algorithms.

Finally, it is relevant to note that the importance of line and voltage dynamics will depend on the specific phenomena of interest and the size of line parameters relative to the inverter, and must be carefully evaluated for each specific study, considering the benefits of such approximation in computational performance.

As concluding remarks, in this section we demonstrate that small stability for VSM inverter models depends in important ways on assumptions about electromagnetic phenomena. Our results indicate that ignoring line and voltage dynamics—which is customary in conventional power system stability assessments—significantly modifies some eigenvalues and regions of small signal stability. These results indicate that, where possible, control loop gains should be tuned with high-order representations of AC-side dynamics. For the transient simulation case we investigated, we find that line/voltage approximations result in similar outcomes. However, transient simulations will depend on the specific parameter sizes, operating points, and phenomena under investigation.

Broadly speaking, our results indicate that low-inertia stability analyses and transient investigations should be done with full order ODEs. However, we have explored only a small number of scenarios, and more studies are needed to identify the specific conditions in which the inaccuracies introduced by line and voltage dynamics approximations are outweighed by the computational advantages of doing so. At a minimum, software tools used in the power systems community to study low inertia phenomena need to be flexible enough to easily provide different levels of line model representation.

This highlights the importance of continuing to focus on AC-side dynamics in multi-machine, multi-inverter systems, while considering the impact of different generator models and inverter control schemes. Because there have been a number of recent advances in numerical techniques for solving stiff systems (e.g. [76]), these need to be included in investigations of the tradeoffs between computational speed and the modeling inaccuracies introduced by AC-side approximations.

2.5   Small-Signal Stability of Load and Network Dynamics on Grid-Forming Inverters

As mentioned in previous sections of this chapter, there have been significant efforts to understand the effects of control strategies of IBRs on system stability, e.g., GFLs and grid-forming GFMs using QSP and EMT approaches. Recent studies have uncovered interactions between excitation systems and inverter controllers using small-signal analyses [78], as well as effects of QSP network modeling in the global and small-signal stability of GFM inverters [36, 42].

However, most of IBR system-wide analyses commonly use constant impedance load models despite the fact that load representation has an important influence on dynamic behavior and system stability [21, 109]. For example, [61, 105] identify that accurate load modeling is an important issue in replicating measurements after disturbances. As discussed by Charles Concordia in the 80's and corroborated in a survey in 2010 by the CIGRE working group C.4605 [87], the industry acknowledges the importance of adequate load modeling. Yet, the emphasis is mostly placed on the accurate modeling of generating units, such as detailed control structures of IBRs, while load models are regarded as of

secondary importance. Further, as power electronics also become commonplace on the load side, the commonly used assumptions about load model structures also need to be revised [6, 32].

The main objective of section work is to explore the interaction of static and dynamic load representations and network dynamics on the small-signal stability of GFM inverters. Here, we present a detailed study of the effects of modeling assumptions on grid-forming stability and dynamic behavior of GFM IBRs. We focus our analysis in three GFM control strategies: droop, VSM and dVOC. The results showcase the control interactions depending on the network model and load representations in the resulting local stability characteristics.

The main contributions of this section are:

- A stability analysis for network dynamics represented in QSP/EMT domain against constant power and ZIP loads.

- A thorough small-signal stability and bifurcation analysis for maximum loadability scenarios for GFM controls considering different load models.

- A discussion of the increased modeling details required to capture constant power load effects and composite loads in the EMT domain.

Notation for this section: The complex imaginary unit is represented by $j = \sqrt{-1}$. We denote the SRF of the network as DQ, rotating at a fixed frequency $\omega_s = 1$ p.u. Bold lowercase symbols are used to represent complex variables in the dq or DQ reference frames, $\boldsymbol{x} = x_\mathsf{d} + jx_\mathsf{q}$. Bold capital symbols are used to denote complex matrices $\boldsymbol{Y} = G + jB$. Finally, we use $\dot{x} = dx/dt$ and $f_x = \partial f/\partial x$.

Instability Aspects of Constant Power Loads

To give intuition about the stability challenges in supplying CPLs, we start our analysis for DC systems, on which a voltage source is supplying a CPL through an inductor. This intuition is similar for dynamic phasor analysis in AC systems, as we discuss later.

As mentioned in [32], ideal CPLs satisfy instantaneously at all times $v \cdot i =$ constant; thus, if a voltage across a CPL increases/decreases, then the current must decrease/increase respectively to satisfy the constant power condition. This behavior can be visualized in Figure 2.28. Most generation sources, such as GFM IBRs or generators whose AVRs are set to voltage control, describe a concave v-i curve that decreases the voltage when the current increases. The intersection $x_0 = (i_0, v_0)$ (black circle) determines the operating point of the source connected to the load. Suppose that an external perturbation increases the current Δi through the inductor, then the load voltage (red circle) is lower than the source voltage (blue circle), resulting in an increase of the current provided by the source. Similarly, if a disturbance decreases the current Δi, the source voltage dips below the load's voltage,
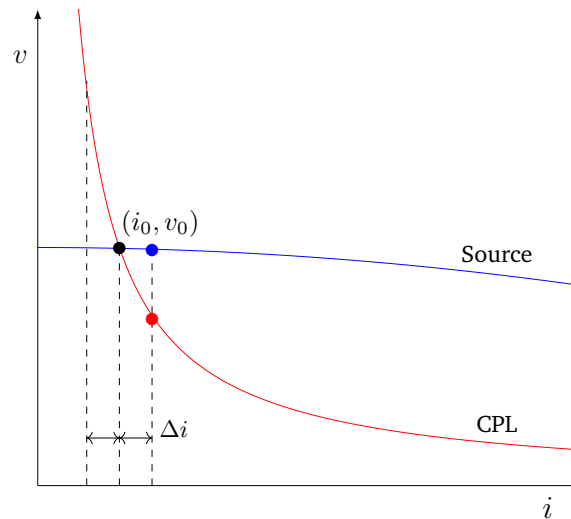
Figure 2.28: v-i curves for common voltage sources and ideal CPLs.

decreasing the current. In both cases, the system moves away from x_0, resulting in an unstable operating condition.

Network dynamics also play a role in the stability assessment of AC systems with CPLs. When network dynamics are neglected, as in standard QSP modeling, the circuit dynamics are represented by the algebraic relationship using the admittance matrix $\boldsymbol{i} = \boldsymbol{Y}\boldsymbol{v}$. In this case, CPLs do not necessarily induce instability in the dynamic model of a generation system connected to the CPL. However, using EMT dynamic phasor modeling, Allen & Ilić [5] show that small-signal stability for a source connected to a CPL ($S = \boldsymbol{v}\boldsymbol{i}^* = \text{constant}$) via a series resistor and inductance requires the condition: $|\boldsymbol{v}_{\text{source}} - \boldsymbol{v}_{\text{load}}| > |\boldsymbol{v}_{\text{load}}|$. This condition is highly unlikely to occur in AC transmission systems, where $|\boldsymbol{v}_{\text{source}}| \approx |\boldsymbol{v}_{\text{load}}| \approx 1.0$ p.u. Thus, the operating points over the desired part of the Power-Voltage (P–V) curve on typical load conditions are always unstable. In practice this is not necessarily observed, since load models and composition changes the stability regions, as we discuss next.

Maximum loadability analysis

To study the effect of load modeling and GFM controls on system stability, we consider a two-bus source vs load balanced system as depicted in Figure 2.29. For GFM inverters, we use a detailed outer control model and inner control models taken from [26, 4, 78], and tune the outer control parameters to have a 2% P-ω p.u./p.u. and 5% Q-v p.u./p.u. droop steady-state response using the procedure described in [55]. Since the focus is on small-signal stability, we ignore hybrid dynamical effects of limiters.

For comparison purposes, the simulation also includes results for SM models. We utilize the GENROU machine model for QSP studies and the Marconato machine model for EMT
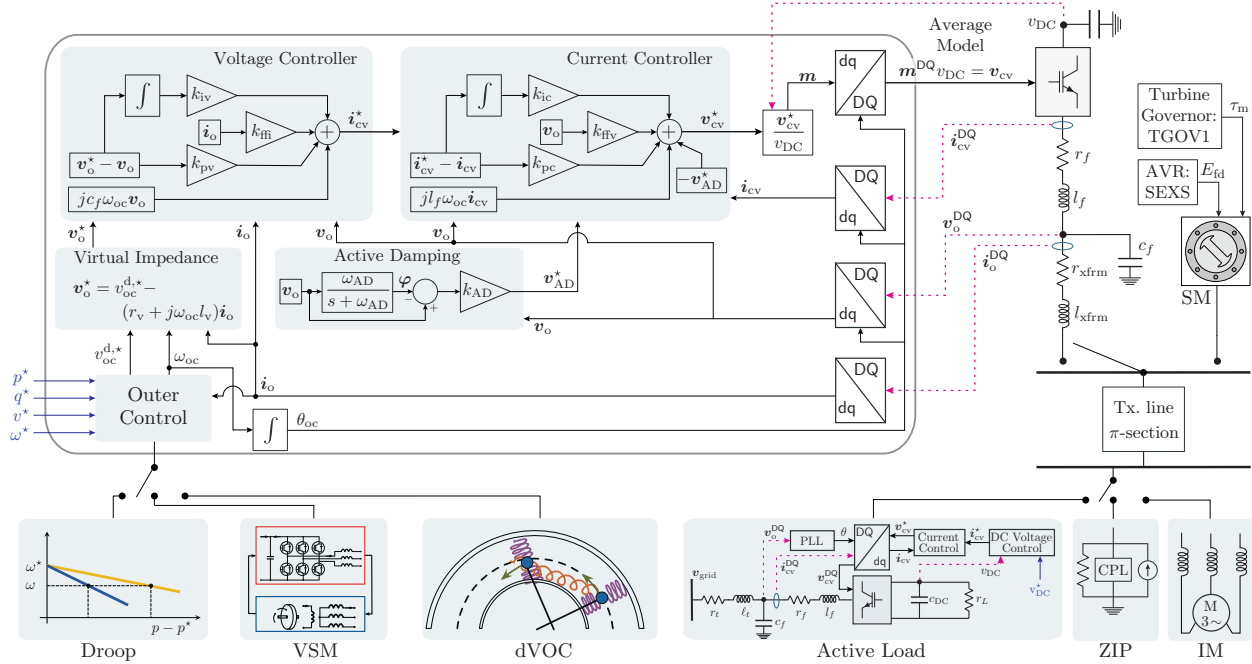
Figure 2.29: Problem set-up for load studies.

studies [85]. To study voltage instabilities it is common to analyze the power/voltage (P–V)
curves to understand if the theoretical maximum value of power can be delivered through
a single line. From a static load flow perspective, this maximum value is attained at the
nose of the upper part of the P–V curve. However, as our results will show, network and
load dynamics reduce the stability regions.

The simulations and analyses are implemented using the Julia package `PowerSimula-`
`tionsDynamics.jl`. The parameters and study cases to replicate the results are available
in the Github repository `https://github.com/Energy-MAC/GFM-LoadModeling`. Summary
of the main results of the following subsections are presented in Table 2.1.

Mathematical representation of IBRs used

This subsection presents the dynamical representation of all models used for GFM IBRs.

Inner Control: All models use the same inner control presented in Figure 2.29. This
consists in algebraic virtual impedance model, with two cascading PI blocks for the voltage
and current controller and a active damping block. This model is equivalent to the one
presented in Section 2.4 and is described again here for completeness:

- *Virtual impedance:* A virtual impedance is used for active stabilization and distur-
bance rejection via a minor cross-coupling of dq components and a non-zero q-component:

Table 2.1: Summary of Maximum Loadability results

Case	Source Model	$P^\star$ [p.u.]	Bifurcation	Participating States
QSP CPL	GENROU	1.169	Hopf	e_q, E_{fd}
	Droop/VSM	1.242	Singularity-Induced	$\boldsymbol{\xi}_{dq}$
	dVOC	1.241	Singularity-Induced	$\boldsymbol{\xi}_{dq}$
EMT CPL	All	>0	Unstable	See subsection on CPL Instability
QSP/EMT CIL or CCL	All	4.5	Stable	
EMT Single -Cage IM	Marconato	0.688	Hopf	e_q, E_{fd}
	Droop/VSM	1.015	Transcritical	$\boldsymbol{\psi}_{dq}$
	dVOC	1.049	Transcritical	$\boldsymbol{\psi}_{dq}$
EMT Active Load	Marconato	1.075	Hopf	e_q, E_{fd}
	Droop/VSM	1.458	Hopf	ζ, v_{DC}
	dVOC	1.430	Hopf	ζ, v_{DC}

$\boldsymbol{v}_o^\star = v_{oc}^{d,\star} - (r_v + j\omega_{oc}l_v)\boldsymbol{i}_o$. The term $\hat{v}$ provides the reference signal for the voltage controller.

- *Cascading controllers:* The inner loop control consists of two cascaded PI controllers, a voltage controller:

$$\dot{\boldsymbol{\xi}} = \boldsymbol{v}_o^\star - \boldsymbol{v}_o \tag{2.52}$$

$$\boldsymbol{i}_{cv}^\star = k_{pv}(\boldsymbol{v}_o^\star - \boldsymbol{v}_o) + k_{iv}\boldsymbol{\xi} + j\omega_{oc}c_f\boldsymbol{v}_o + k_{ffi}\boldsymbol{i}_o, \tag{2.53}$$

and a current controller:

$$\dot{\boldsymbol{\gamma}} = \boldsymbol{i}_{cv}^\star - \boldsymbol{i}_{cv} \tag{2.54}$$

$$\boldsymbol{v}_{cv}^\star = k_{pc}(\boldsymbol{i}_{cv}^\star - \boldsymbol{i}_{cv}) + k_{ic}\boldsymbol{\gamma} + j\omega_{oc}l_f\boldsymbol{i}_o + k_{ff}^v\boldsymbol{v}_o - \boldsymbol{v}_{AD}^\star, \tag{2.55}$$

- *Active Damping:* An active damping term is included for additional suppression of oscillations in the LC filter [26]:

$$\dot{\boldsymbol{\varphi}} = \omega_{AD}(\boldsymbol{v}_o - \boldsymbol{\varphi}) \tag{2.56}$$

$$\boldsymbol{v}_{AD}^\star = k_{AD}(\boldsymbol{v}_o - \boldsymbol{\varphi}) \tag{2.57}$$

Outer Control: The three models considered for GFM IBRs are:

- *Droop Control:* The model achieves synchronization using two droop controllers for
frequency - active power and voltage - reactive power, via two low-pass filters as follow:

$$\dot{\theta} = \Omega_b(\omega_{\text{oc}} - \omega_s) \tag{2.58a}$$

$$\dot{p}_f = \omega_z(p_e - p_f) \tag{2.58b}$$

$$\dot{q}_f = \omega_z(q_e - q_f) \tag{2.58c}$$

$$\omega_{\text{oc}} = \omega^\star + k_p(p^\star - p_f) \tag{2.58d}$$

$$v_{\text{oc}}^{\text{d},\star} = v^\star + k_q(q^\star - q_f) \tag{2.58e}$$

- *VSM:* The model is equivalent as the one presented in Section 2.4 in equations (2.6)–
(2.9), and presented again here for completeness:

$$\dot{\theta} = \Omega_b(\omega_{\text{oc}} - \omega_s) \tag{2.59a}$$

$$\dot{\omega}_{\text{oc}} = \frac{1}{M}\left[(p^\star - p_e) + \frac{1}{k_p}(\omega^\star - \omega)\right] \tag{2.59b}$$

$$\dot{q}_f = \omega_z(q_e - q_f) \tag{2.59c}$$

$$v_{\text{oc}}^{\text{d},\star} = v^\star + k_q(q^\star - q_f) \tag{2.59d}$$

- *dVOC:* The model for the dVOC is based on [4] as:

$$\dot{\theta} = \Omega_b(\omega_{\text{oc}} - \omega_s) \tag{2.60a}$$

$$\dot{v}_{\text{oc}}^{\text{d},\star} = \Omega_b\left[\frac{k_1}{v_{\text{oc}}^{\text{d},\star}}\left[-\sin(\gamma)(p^\star - p_e) + \cos(\gamma)(q^\star - q_e)\right] + k_2\left[(v^\star)^2 - (v_{\text{oc}}^{\text{d},\star})^2\right]v_{\text{oc}}^{\text{d},\star}\right] \tag{2.60b}$$

$$\gamma = \psi - \frac{\pi}{2} \tag{2.60c}$$

$$\omega_{\text{oc}} = \omega_s + \frac{k_1}{(v_{\text{oc}}^{\text{d},\star})^2}\left[\cos(\gamma)(p^\star - p_e) + \sin(\gamma)(q^\star - q_e)\right] \tag{2.60d}$$

In all models, the active power p_e and reactive power q_e are measured flowing to the
second leg of the LCL filter, that is:

$$p_e + jq_e = \boldsymbol{v}_{\text{o}}\boldsymbol{i}_{\text{o}}^\dagger = (v_{\text{o}}^{\text{d}} + jv_{\text{o}}^{\text{q}})(i_{\text{o}}^{\text{d}} - jv_{\text{o}}^{\text{q}})$$

We utilize the network frequency as $\omega_s = 1$ p.u., with $\Omega_b = 2\pi60$ the base frequency, and
filter and network dynamics are the same as the ones used in Section 2.4 in (2.15)–(2.17)
and (2.21)–(2.23), respectively.

QSP P–V curves for CPLs

A QSP analysis ignores network dynamics and assumes that circuit dynamics evolve to a
stable equilibrium. Thus, filters and transmission lines are modeled using the algebraic
admittance matrix representation $\boldsymbol{i} = \boldsymbol{Y}\boldsymbol{v}$.
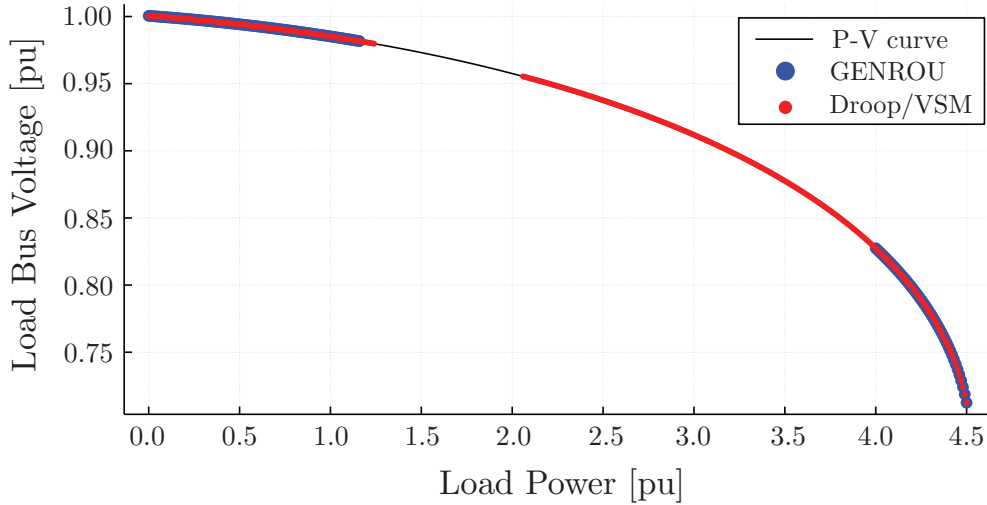
Figure 2.30: P–V Curve for sources connected to a CPL in a QSP study.

Figure 2.30 depicts our analysis in the QSP domain assuming a single source connected to a CPL. The results only show the P–V curves for GENROU and Droop/VSM for clarity, and P–V curves for all models are available in the repository. The curves were constructed using load power from 0 to 4.5 p.u., the *nose* of the P–V curve, using a discrete step of 0.01 p.u. We examined the eigenvalues of the linearized reduced system $A = f_x - f_y g_y^{-1} g_x$ (or $A_0 = A_{11} - A_{12} A_{22}^{-1} A_{21}$ as described in Section 2.4) at each operating point. For all source models, the colored regions depict stable operating points, while empty regions showcase unstable operating conditions.

We can observe that the instability boundary occurs at similar loading levels for all generation sources $P \approx 1.2$ p.u. (see Table 2.1); however, the bifurcation characteristics are significantly different between GFM inverters and the GENROU model. In the GENROU case, the critical eigenvalues are a complex pair that crosses the $j\omega$ axis when the load reaches the critical $P^\star$. This behavior corresponds to a subcritical *Hopf bifurcation* for SMs [19], where the q-axis voltage e_q' and the field voltage E_{fd} states have most significant participation factors in the unstable eigenvalues. In Figure 2.31 we depict the phase portrait of the transient q-axis voltage e_q' and the field voltage E_{fd} states, the ones with largest participation on such eigenvalues. We introduce different perturbations in the value of e_q' and the resulting trajectories (of the non-linear system) are presented. At the critical load $P^\star$, there is an unstable limit cycle around the locally stable equilibrium point, a consistent result with the literature that this is a subcritical Hopf bifurcation.

The bifurcation characteristics of the GFM inverters are significantly different than the SM case. Specifically, we observe a Singularity-Induced Bifurcation (SIB) as the load value increases [79]. When the system reaches $P^\star$ one eigenvalue, associated with the integrator of the GFM voltage controller $\boldsymbol{\xi}_{dq}$, crosses $\pm\infty$ to the other side of the complex plane,
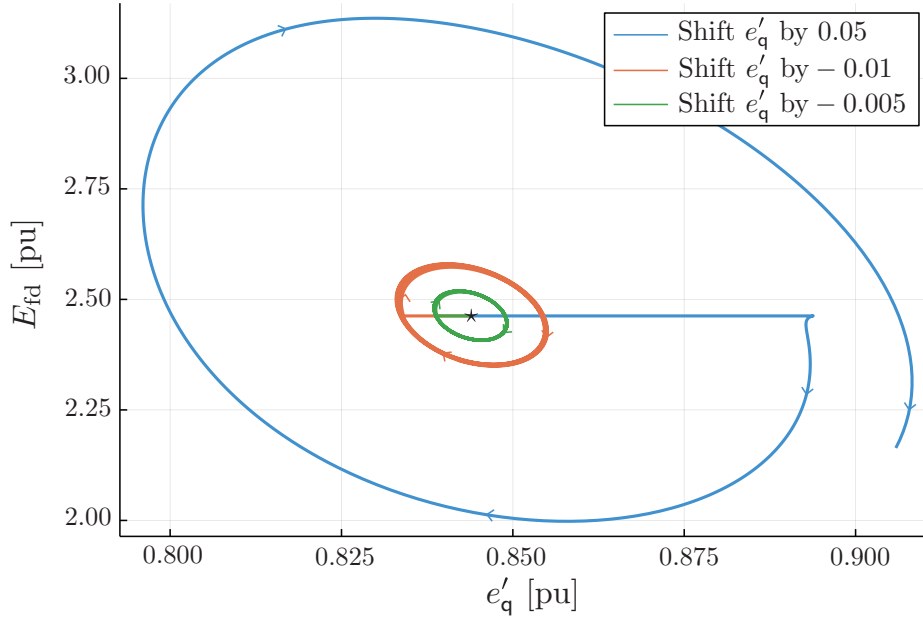
Figure 2.31: Phase portrait e_q'–E_{fd} for GENROU machine at $P^\star = 1.169$ pu.

changing the stability of the system (see Table 2.1).

Furthermore, the stability regions of the Droop/VSM are equivalent since the outer control parameters achieve the same steady-state response, and the inner control parameters are the same. The case of the dVOC is slightly different since the droop behavior depends on e_0, which changes at different load levels [55]. When tuning the dVOC parameters to match the steady state droop response, we assume $e_0 = 1$ p.u. (i.e., no load).

EMT P–V curves for ZIP and Induction Machine models

The analysis in this section has the same setup as the previous subsection, but now including detailed circuit models for the AC filters and transmission lines in a SRF, described by equations (2.21)-(2.23) in Section 2.4. Ideal CPL models result in a unstable system as the eigenvalues associated with the transmission become positive, as discussed in previous subsections. On the contrary, algebraic models for Constant Current Load (CCL) and Constant Impedance Load (CIL) result in stable regions for all operating conditions and all source models considered.

The single-cage Induction Machine (IM) load uses 5th-order dynamic phasor EMT model [62] including an algebraic capacitor model in parallel to ensure unitary power factor of the IM device. A similar P–V curve is constructed (available in the repository) with the IM parameters. Table 2.1 showcases that in this case the system exhibits a similar Hopf bifurcation for the states E_{fd} and e_q' for the SM case. These results are similar to the QSP–CPL case, in which the critical eigenvalues are associated with the excitation system. This
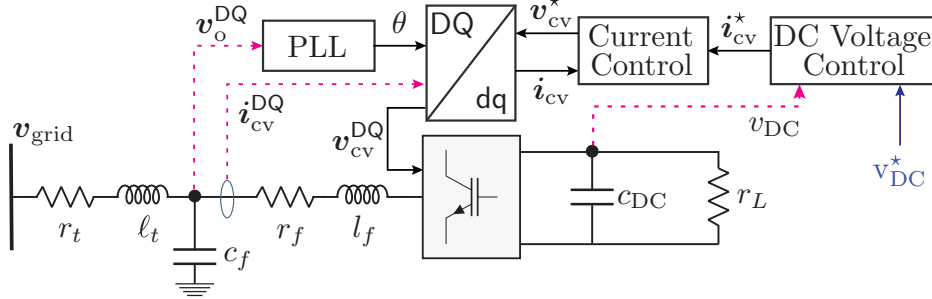
Figure 2.32: Active load block diagram.

reveals that an AVR re-tuning or the addition of a power system stabilizer can enhance stability regions.

In contrast to the QSP–CPL setting, there are no algebraic states when the IM is supplied through GFM, so no SIB can occur. However, for GFM inverters at the critical load $P^\star$, a single real eigenvalue crosses to the right hand side causing a transcritical bifurcation. The states associated with this eigenvalue, according to its participation factors, are the IM rotor flux linkages ψ^r_{dq}. Hence, in this case the stability limits comes from the the IBR and load models interactions.

EMT P–V curves for an active load

As discussed in previous subsections, ideal CPL models are not suitable for EMT studies, so in this section we employ a 12-state model *Active Load* model that measures the AC side using a Phase-Lock-Loop (PLL) and regulates a DC voltage to supply a resistor r_L. This model induces a CPL-*like* behavior as it tries to maintain a fixed DC voltage to supply $P = v^2_{\mathrm{DC}}/r_L$ [77]. Figure 2.32 showcases the *Active Load* model, on which the reference term $i^\star_{\mathsf{q}}$ from the DC voltage controller is chosen to regulate minimum reactive power consumed from the active load.

The complete model is given by:

$$\dot{\theta} = \Omega_b(\omega_{\mathrm{pll}} - \omega_s) \tag{2.61a}$$

$$\dot{\epsilon} = v^{\mathsf{q}}_{\mathsf{o}} \tag{2.61b}$$

$$\omega_{\mathrm{pll}} = \omega^\star + k^p_{\mathrm{pll}} v^{\mathsf{q}}_{\mathsf{o}} + k^i_{\mathrm{pll}} \epsilon \tag{2.61c}$$

$$\dot{\zeta} = v^\star_{\mathrm{DC}} - v_{\mathrm{DC}} \tag{2.61d}$$

$$i^{\mathsf{d},\star}_{\mathrm{cv}} = k^p_{\mathrm{DC}}(v^\star_{\mathrm{DC}} - v_{\mathrm{DC}}) + k^i_{\mathrm{DC}} \zeta \tag{2.61e}$$

$$\frac{c_{\mathrm{DC}}}{\Omega_b} \dot{v}_{\mathrm{DC}} = \frac{p_{\mathrm{cv}}}{v_{\mathrm{DC}}} - \frac{v_{\mathrm{DC}}}{r_L} \tag{2.61f}$$

$$\dot{\gamma}_{\mathsf{d}} = i^{\mathsf{d}}_{\mathrm{cv}} - i^{\mathsf{d},\star}_{\mathrm{cv}} \tag{2.61g}$$

$$\dot{\gamma}_{\mathsf{q}} = i^{\mathsf{q}}_{\mathrm{cv}} - i^{\mathsf{q},\star}_{\mathrm{cv}} \tag{2.61h}$$
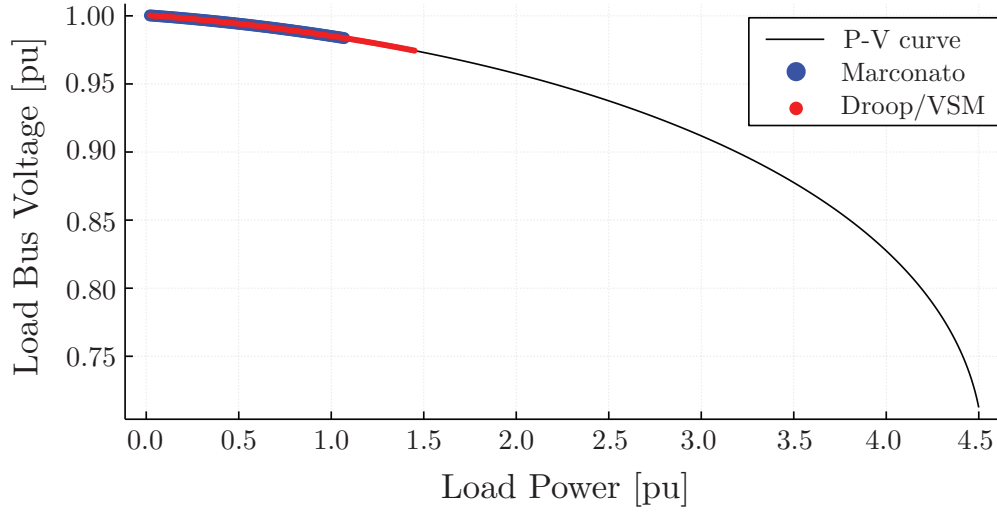
Figure 2.33: P–V curves for EMT/active load model.

$$v_{cv}^{d,\star} = k_{pc}(i_{cv}^{d} - i_{cv}^{d,\star}) + k_{ic}\gamma_{d} + \omega_{pll}l_{f}i_{cv}^{q} \tag{2.61i}$$

$$v_{cv}^{q,\star} = k_{pc}(i_{cv}^{q} - i_{cv}^{q,\star}) + k_{ic}\gamma_{q} - \omega_{pll}l_{f}i_{cv}^{d} \tag{2.61j}$$

Equations (2.61a), (2.61b) and (2.61c) describes the PLL dynamics to lock the active load to the grid. Equations (2.61d)–(2.61e) describes the DC Voltage Controller to steer the DC voltage to $v_{DC}^{\star}$, while equation (2.61f) describes the DC voltage dynamics at the capacitor assuming an ideal converter. Finally, equations (2.61g)–(2.61j) describes the dynamics of the AC Current Controller. Additional six states are defined for the LCL filter in the same fashion of equations (2.15)–(2.17).

The resulting P–V curves are depicted in Figure 2.33. The GFM inverters case shows two critical eigenvalues associated with the load's model DC voltage controller integrator state ζ and the DC Voltage v_{DC}. As the load power is increased, two complex conjugate eigenvalues move from the left-hand to right-hand side complex plane generating a Hopf bifurcation as depicted in Figure 2.34. The phase portrait showcases the states v_{DC} and ζ, as we introduce different perturbations in the value of v_{DC} to assess the system stability. At the critical load $P^{\star}$ there an is unstable limit cycle around a locally stable equilibrium point, which is consistent with a subcritical Hopf bifurcation. A re-tuning in the active load DC voltage PI controller is a future direction to explore to enhance system stability, changing their dynamic characteristics if needed.

Importance of Composite Load Modeling in GFM dominated systems

The ZIP model consists of three loads in parallel, a CPL, a CCL, and a CIL, and it is ubiquitous in QSP power system studies. A ZIP load can capture the static and dynamic behavior
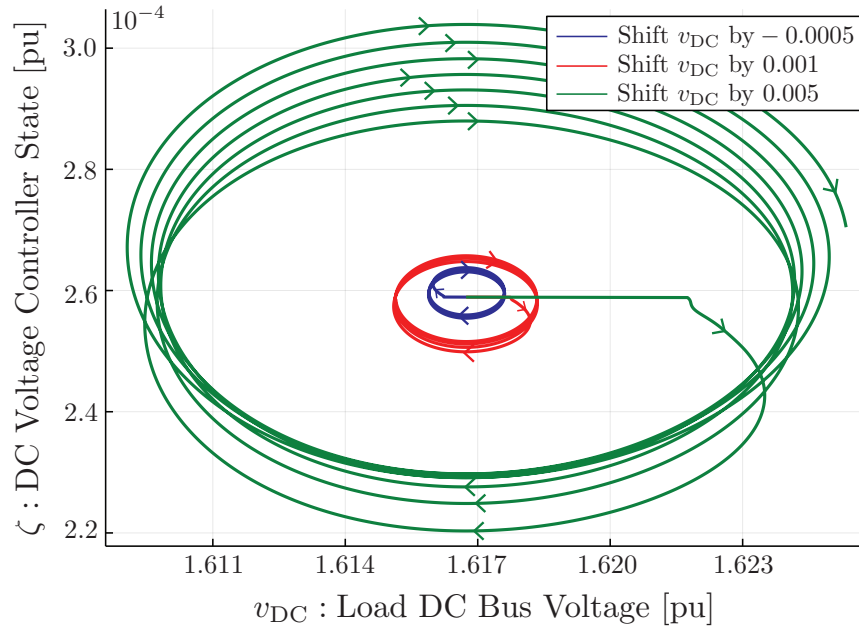
Figure 2.34: Phase portrait v_{DC}–ζ for droop GFM supplying active load at $P^\star$.
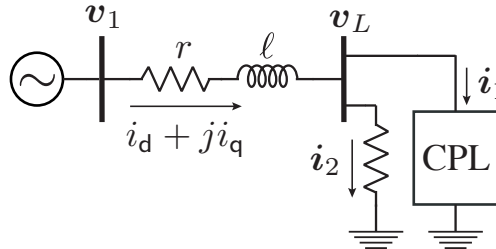
Figure 2.35: ZIP Load example.

of many aggregated composite loads in power systems with the appropriate proportion assignment to each submodel. Unfortunately, there are no closed-form results (such as those presented in [5]) on small-signal stability for the dynamic phasor domain. However, it is possible to obtain results in some cases; for example, in the system depicted by Figure 2.35, the electric current dynamic phasor (in p.u.) flowing through the line are given by:

$$\frac{\ell}{\Omega_b} \frac{d\boldsymbol{i}_{\text{dq}}}{dt} = \boldsymbol{v}_{\text{dq1}} - \boldsymbol{v}_{\text{dqL}} - r\boldsymbol{i}_{\text{dq}} - jx\boldsymbol{i}_{\text{dq}}, \tag{2.62}$$

in $x = \omega_s \ell$ is the line reactance, where $\omega_s = 1.0$ p.u. Given an operating point, we are looking to compute the eigenvalues of the linearized system. To do so we solve for the term

$\boldsymbol{v}_L$ given the load parameters of the resistor r_L and CPL values (P, Q):

$$\boldsymbol{i} = \boldsymbol{i}_1 + \boldsymbol{i}_2, \qquad \boldsymbol{v}_L \boldsymbol{i}_1^* = P + jQ, \qquad \boldsymbol{i}_2 = \frac{\boldsymbol{v}_L}{r_L} \tag{2.63}$$

Equations (2.63) are a system of non-linear equations where is possible to solve $\boldsymbol{v}_L$ as a function of $\boldsymbol{i}$, resulting in two possible solutions. Given the complexity of symbolic solution, there is no closed form relationship for assessing stability as a function of the proportion between CIL $\boldsymbol{i}_1$ and CPL $\boldsymbol{i}_2$ in the ZIP load model. However, it is possible to analyze the stability by constructing the following system of DAE system:

$$\dot{x} = f(x, y, \eta) \tag{2.64}$$
$$0 = g(x, y, \eta) \tag{2.65}$$

where $f(x, y, \eta)$ represents the line current equations (2.62) and $g(x, y, \eta)$ are the algebraic equations of the ZIP load (2.63). In here, $x = \boldsymbol{i}$ are differential states and $y = [\boldsymbol{v}_L, \boldsymbol{i}_1, \boldsymbol{i}_2]$ are algebraic states and the parameter η is used to control the proportion of CPL to CIL. Assuming no reactive power load (i.e. $Q = 0$) in this system, we obtain the determinant of the Jacobian of the algebraic constraints with respect to the algebraic states as follows:

$$\det(g_y(x, y, \eta)) = |\boldsymbol{i}_1|^2 - \frac{|\boldsymbol{v}_L|^2}{r_L^2} = |\boldsymbol{i}_1|^2 - |\boldsymbol{i}_2|^2 \tag{2.66}$$

Equation (2.66) becomes zero when the magnitude of the currents flowing through the CPL and the impedance are equal introducing a SIB [79].

We illustrate the bifurcation with the following numerical example: consider the system presented in Figure 2.35 with $r = 0.01$, $x = 0.1$, $P_{\text{cpl}} = 1$ p.u., and $\boldsymbol{v}_1 = 1.0 + 0j$ p.u. The proportion of current flowing through r_L and the CPL can be adjusted using the parameter $\eta \in (0, 1)$ as follows:

$$P_{\text{zip}} = \eta P_{\text{cpl}} + P_{r_L} = 1 \;\rightarrow\; P_{r_L} = 1 - \eta P_{\text{cpl}} \tag{2.67a}$$
$$P_{r_L} = \frac{|\boldsymbol{v}_L|^2}{r_L} = 1 - \eta P_{\text{cpl}} \;\rightarrow\; r_L = \frac{|\boldsymbol{v}_L|^2}{1 - \eta P_{\text{cpl}}} \tag{2.67b}$$

In this fashion, we ensure the total load to be always 1 p.u. (reactive power is set to zero); hence, steady-state voltage is constant at $|\boldsymbol{v}_L| = 0.985$ p.u. Equations (2.67) allow us to traverse through the singularity manifold $S \equiv \{(x, y, \eta) \mid \det(g_y(x, y, \eta)) = 0\}$, to analyze the trajectory of the line current i_d, i_q eigenvalues.

As we change the parameter η from $0 \rightarrow 1$, one of the eigenvalues of the reduced system ($A = f_x - f_y g_y^{-1} g_x$) moves towards $-\infty$, and changes sign as we cross the singularity manifold at $\eta^\star = 0.5$, while the second eigenvalue remains on the left side of the complex plane. The line current states remain small-signal stable if $\eta < 0.5$, a condition where the current magnitude through the resistor is larger than the CPL current magnitude. Figure
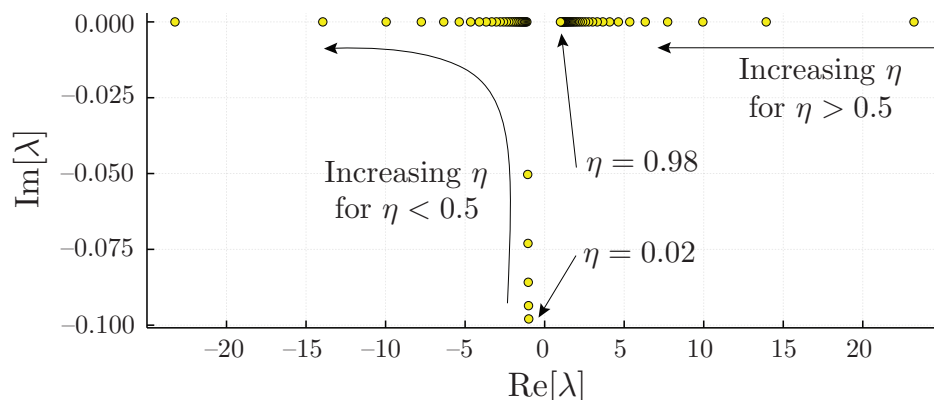
Figure 2.36: Root locus as η changes from $0 \to 1$.

2.36 showcases the root-locus of this eigenvalue as we increase η, on which we observe that diverges through $-\infty$, changing sign when $\eta \geq 0.5$.

The example highlights the importance of load model composition on network stability. As we move towards a system with larger shares of IBRs and fast dynamics become more relevant, the results show the dependence between current stability and different proportions of a ZIP load model. The analysis showcases the potential inadequacies of modeling only CIL or CPL and the need for detailed composite load models as we increase the shares of IBR generation.

As concluding remarks, this Section demonstrates that small-signal stability conclusions for IBRs are heavily dependent on modeling assumptions regarding electromagnetic network phenomena and load representation. The results indicate that considering line and voltage dynamics significantly affects which load models are suitable to use in dynamic studies. As power systems integrate increasing amounts of electronics-based loads that behave as CPLs and IBRs, more advanced CPL models are needed to assess stability.

However, we have only explored single-line systems and a specific set of parameters and load models. More comprehensive studies are needed using composite load models in more extensive systems to properly assess the changing stability regions as we increase system loading. Future work should focus on exploring different load model distribution scenarios using a combination of SMs and IBRs models in the system. Further, the inclusion of limiters for SMs controllers and current limits in IBRs can significantly affect system stability and introduce other kinds of bifurcations. Exploring more precise control and protection effects in IBR-dominated systems in combination with load recovery models is also a relevant research direction.

2.6 Conclusions

The results presented in this chapter highlight the importance on modeling details in computational studies, in particular for future power systems dominated by GFM inverters. In this chapter, we first discussed how GFM technology will be crucial to ensure a reliable transition to inverter dominated systems. As we phase-out more traditional generation, ancillary services commonly provided by these rotating units will be provided by IBRs, and GFM inverters are natural candidates to cover for these requirements.

However, given the importance of power systems in our society, these changes must be analyzed first using analytical and computational tools. We discussed how scientific computing is crucial to ensure that our studies enable reproducibility of the experiments, and has mechanisms to verify the validity of the conclusions derived. This is particularly relevant today when there exists a myriad of models and assumptions for IBRs, that will significantly modify the stability results of these devices connected in power systems. Open source tools, such as PowerSimulationsDynamics.jl, are one of the first steps to ensure model transparency with the flexibility to enable or disable system assumptions via the choice of device and network model complexity.

We have presented how changing network dynamics modify the regions of small-signal stability in VSM inverters. In particular, we showed that neglecting these dynamics over-estimate these regions, possibly providing a false estimation if the tuning of the outer control loop is done using a QSP model. This showcase how rooted assumptions in positive sequence studies should be revisited to ensure a secure transition into a renewable grid.

In addition, as we move to more active distribution grids, with more renewable sources and electronics-based loads, such as EV chargers, there is a necessity to revisit our modeling assumptions for load models. Since network dynamics are more relevant in a inverter-dominated grid, traditional models such as ideal CPL are not useful to study the interactions between IBRs, loads and the AC network. In this changing scenario there is a necessity for more detailed load models, such as active load models, that can capture better the dynamics of a CPL-*like* model. Proper load composition will be crucial to ensure that inverter interactions are properly represented in simulation studies that can accurate replicate real measurements after disturbances.

There is still plenty of work to be done. All the studies presented in this chapter assume that there is a stiff DC voltage source that can supply all the power required from the AC side. Accurate model of the DC-side, such as solar PV and wind turbines, is a relevant aspect to assess IBR stability in power systems. In addition, inverter cannot provide large short-circuit current due to hardware limitations, and hence the effects of current limiters is a relevant future direction, particularly for analyzing limit-induced bifurcations. Finally, as more SMs are replaced by IBRs, it is expected low short-circuit currents in the grid. Protection coordination in this scenario is an important research direction for future work.

Chapter 3

Peer-to-peer and Sharing Economy of Distributed Solar Generation Investment

Investment in renewable sources has seen substantial growth in recent years. For example, in the last 5 years, renewable generation capacity has seen an average annual growth of 8.5% [53]. In particular, investment in PV has seen significant growth worldwide, from 40 GW in installed capacity in 2010 to 303 GW in 2016 [80]. In the U.S., PV has an average annual growth of 68% over the last decade. The U.S. solar industry employment grew by 16% annually in the five-year period, between 2012 and 2017, adding 131,000 jobs [125]. Much of this prominent growth is from small-scale distributed systems.

Distributed Generation (DG) can play a major role in future electricity grids to meet the energy demand by promoting renewable sources and reducing the greenhouse gas emissions associated to the power grid. In this sense, rooftop solar PV has been the main participant in recent decades.

Three key factors drive growth in behind-the-meter PV systems. First, as depicted in Figure 3.1, the integrated costs of PV have fallen by 50% over the last years [34, 10], and levelized electricity costs are now below $0.16 per kWh for distributed rooftop systems in many regions [22]. Second, state and federal subsidies improve the private economics of PV—for example, the federal investment tax credit (equal to 30% of installation costs) [92]. Third, net-metering policies, in which utilities credit customers for hourly production in excess of their consumption, effectively mandate utilities to purchase excess distributed solar PV production at retail rates, which are much higher than utilities' avoided cost of purchasing energy from wholesale generators.

However, subsidies and tax credits are being phased out, and utilities strenuously oppose net-metering because it enables customers to avoid the true costs of infrastructure, reserves, and reliability. In some of the sunniest states (Arizona and Hawaii), net-metering programs are weakening or disappearing altogether [94]. In addition, these policies are criticized due to the increased cost shift from owners of distributed generation to other utility ratepayers. Depending on the net avoided cost of utilities and net-metering policies, expanding PV penetration can increase the retail price of electricity [8].
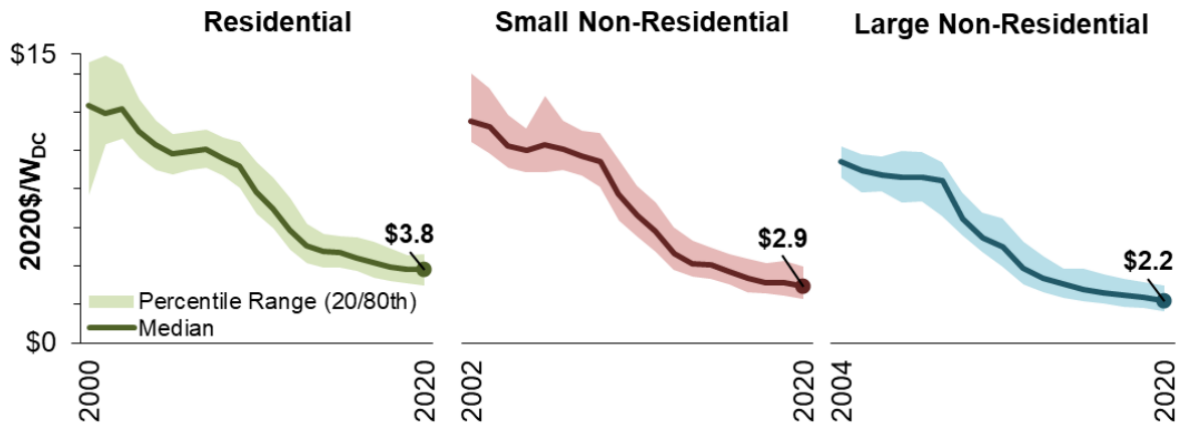
Figure 3.1: Solar PV installation costs trends. Figure from [9].

Are there feasible and sensible strategies to sustain the future growth in behind-the-meter PV in the face of these challenges? *In this chapter, based on our papers [45, 46], we submit that the sharing economy business model offers a plausible pathway.* Sharing has already transformed housing and transportation markets by allowing individuals to offer underutilized products like ridesharing (Uber, Lyft) and unoccupied real estate (Airbnb) on peer-to-peer platforms. Here, we explore how connected communities of homes could share excess electricity generation. There are several pilot programs that are currently studying sharing economy models for transactions of excess solar generation. For example, the Brooklyn Microgrid in the U.S., or the NRGcoin in Europe, are projects exploring peer-to-peer energy transactions using blockchain-based frameworks, and how those P2P models can be implemented in theory and practice [83, 120, 128, 127].

There is also an important precedent for solar sharing in the United States: at least 16 states have "virtual net-metering" programs that allow owners of one solar system to distribute net-metering credits to the bills of other customers [52, 17, 135]. In some states these programs are limited to individual properties (for example multi-tenant housing), but in other states all customers are eligible to pool credits with other customers. These programs extend net-metering to aggregations of buildings but continue to rely on the notion of reverse flow receiving the same credit as consumption. Multiple available schemes are summarized in Figure 3.2.

Here we investigate a model that could persist if the concept of net-metering is eliminated, in which groups of customers pool their *hourly* consumption and production, with pooled hourly net reverse flow receiving no utility credit. In this chapter, we analyze the PV investment decisions of individual homes under a sharing economy model, and compare them to decisions that would occur in the status quo standalone net-metering case, and also against a collective of homes participating in wholesale markets.

There is a substantial amount of work on optimal sizing and siting of DG. The basic idea
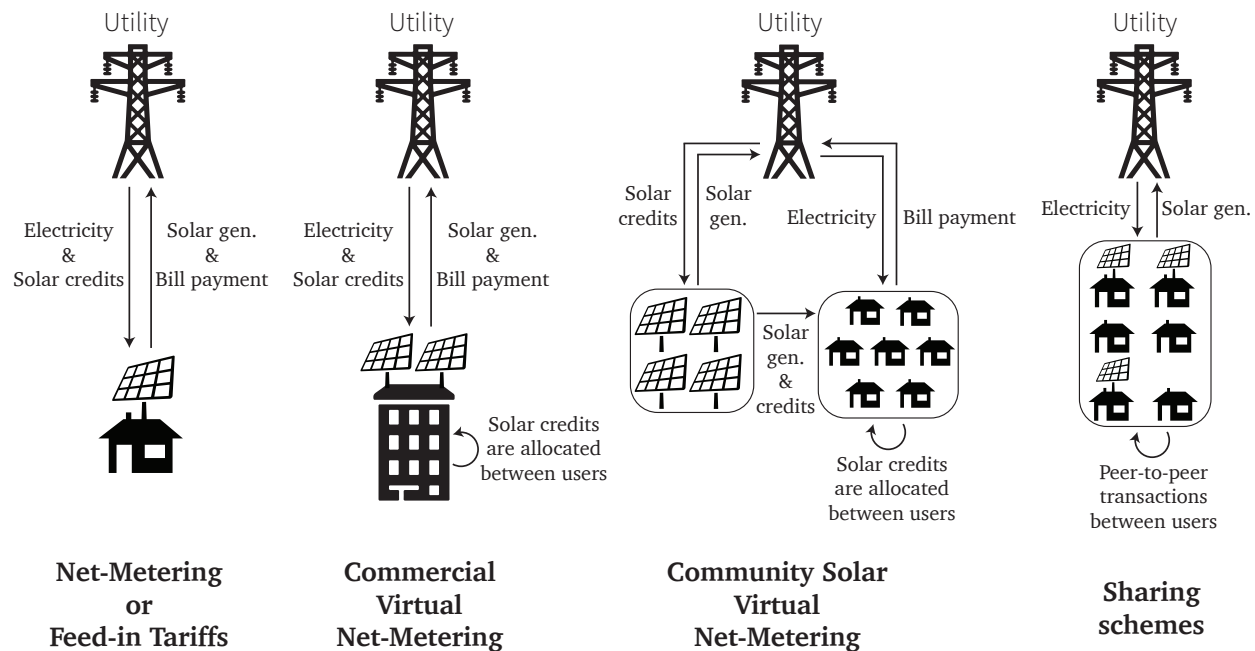
Figure 3.2: Multiple net-metering and sharing schemes for users.

of aggregating variable energy production (or consumption) has been developed in other contexts, including flexible loads [14, 39] and transmission-level aggregation of renewables [96, 140]. On the other hand, papers such as [112, 91, 57, 89, 58, 38] focus on engineering impacts, cost minimization or utility profit maximization of DER for individual consumers or utilities. Game theoretical approaches [71, 103, 129], examine peer-to-peer energy trading schemes among consumers and producers, but these do not study the amount of capacity firms should procure. We are unaware of efforts to address how PV investment decisions are affected when users are able to share or aggregate their solar production (depending on the market scheme).

In this chapter we propose different optimization models to determine optimal investment of PV under various pricing and sharing schemes, considering explicitly the uncertainty from behind-the-meter energy consumption and solar generation. The main contributions of this work are:

- We formulate solar investment decisions under various pricing and sharing schemes as optimization problems that explicitly model uncertainty arising from behind-the-meter energy consumption and solar production. These includes a status-quo standalone net-metering case, a sharing scheme and a wholesale market approach for optimal investment in behind the meter PV.

- We show that investment decisions in the shared solar case can be cast as a game that

admits a unique, social welfare supporting, Nash equilibrium, while also deriving a simple optimal investment threshold policy for individual customers participating in the shared setting.

- We provide intuition for the main drivers of rooftop PV investment, such as PV costs, retail prices and net-load characterization. This is one of the first studies to show how PV investment is affected by market design. We also show that some standalone customers will over-invest and others will under-invest, relative to the social-welfare maximizing decisions of the shared solar case.

- We present thorough analysis of different numerical simulations, using real data on load profiles and solar production. Results show that sharing schemes can promote PV investment in comparison to standalone scenarios, while wholesale market models can drastically modify PV investment in presence of distribution fees.

Nomenclature and Notation for this Chapter

Sets

$\mathcal{N}$ Set of firms or households, indexed by $k = 1, \ldots, n$.

$\mathcal{T}$ Set of time slots, indexed by $t = 1, \ldots, T$.

$\mathcal{M}$ Set of periods that represents a collective of consecutive time slots, indexed by $m = 1, \ldots, M$, that usually represents months or years.

$\mathcal{T}_m$ Subset of time slots that belong to a period m.

Parameters

$\ell_k(t)$ Random load of firm k in time slot t in kW.

$w_k(t)$ Effective random irradiance at firm k in time slot t in kW/m^2.

π^{s} Capital cost of solar PV per m^2 amortized over T time slots.

$\pi^{\mathrm{g}}(t)$ Wholesale price of electricity in \$/kWh.

$\pi^{\mathrm{d}}(t)$ Retail tariff for electricity in distribution in \$/kWh.

$\pi^{\mathrm{nm}}(t)$ Net-metering price or feed-in-tariff for selling electricity to the grid in \$/kWh.

a_k^{max} Maximum area available to install PV panels for the firm k.

a_k^{cap} Area necessary to install PV panels for the firm k to be a zero-energy firm (in expectation) in the analyzed time horizon (called annual cap).

P_k^{max} Maximum limitation of energy injection imposed by the utility.

Variables

a_k Panel area in m² installed for user k.

$\boldsymbol{a}$ Vector that contains the PV installed a_k for all users.

Finally, we define the average expected value as $\overline{\mathbb{E}}_{\mathcal{T}}[x|y] = \frac{1}{T}\sum_{t\in\mathcal{T}}\mathbb{E}[x(t)|y(t)]$ and the positive part function as $f(x)^+ = \max(f(x), 0)$.

3.1   Problem Set-up for Firms under Different Market Schemes

Consider a connected community $\mathcal{N}$ of n firms (users) or households indexed by k. These firms are considering the installation of rooftop solar PV systems. The investment decision for firm k is the panel area a_k for its PV system. We consider a multi-year investment horizon broken into small time intervals on which time slots are indexed by t (we will assume time slots are one hour in simulations).

We use a simple linear model of investment costs: the price of PV panels amortized over their lifetime is π^{s} \$/m² per time slot. This can be derived by combining the commonly used \$/watt PV levelized cost figures with production models, or using overnight costs over the entire time horizon. For example, assume the overnight cost of installing PV panels is given by Π in \$/m² (this includes installation + infrastructure cost). Consider a time slot t of h hours duration (possibly 1 hour), a PV panel lifetime of T_y years (commonly 20 years) and an annual discount rate r_y (such as 4%). The previous implies that there are approximately N time slots in the PV panel's lifetime, calculated as:

$$N \approx \left\lfloor \frac{1}{h} \times 24 \times 365.25 \times T_y \right\rfloor \tag{3.1}$$

Then the amortized cost of the PV panels per time slot π^{s} can be calculated using:

$$\Pi = \sum_{n=0}^{N-1} \frac{\pi^{\mathrm{s}}}{(1+r_d)^n} = \pi^{\mathrm{s}} \frac{1-(1+r_d)^{-N}}{1-(1+r_d)^{-1}} \;\rightarrow\; \pi^{\mathrm{s}} = \Pi \cdot \frac{1-(1+r_d)^{-1}}{1-(1+r_d)^{-N}} \tag{3.2}$$

where r_d represents the discount rate per time slot, calculated using the formula:

$$(1+r_d)^{\left\lfloor \frac{1}{h} \times 24 \times 365.25 \right\rfloor} = (1+r_y)^1 \tag{3.3}$$

The solar profile available to firm k in time slot t is denoted by $w_k(t)$. If the firm invests in a_k of panel area, it generates $a_k w_k(t)$ kWh of electricity. We say that $w_k(t)$ captures the *effective* irradiance including factors such as panel efficiency, inverter efficiency and relative declination of incident sunlight. It varies with the time of day and technology choice. The electricity demand for home k in time slot t is $\ell_k(t)$. We treat ℓ_k and w_k as

non-stationary random sequences. The firm demand $\ell_k(t)$ is first served by its own local PV production. The deficit or *net-load* $(\ell_k(t) - a_k w_k(t))^+$ is bought from the utility at a specific tariff. Depending on the situation, any surplus may be sold back through different schemes. This situation is depicted in Figure 3.3.
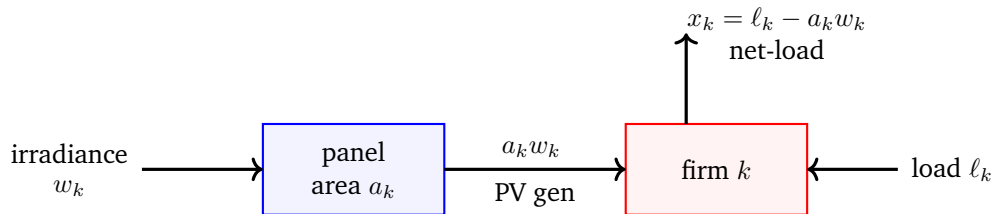
Figure 3.3: Set-up for each firm k: effective irradiance w_k, panel area investment a_k, PV generation $a_k w_k$, load ℓ_k, and net-load $x_k = \ell_k - a_k w_k$.

We consider three different problems to studying the investment of PV panels from firms or households. Figure 3.4 provides a visual presentation of the three proposed market structures.
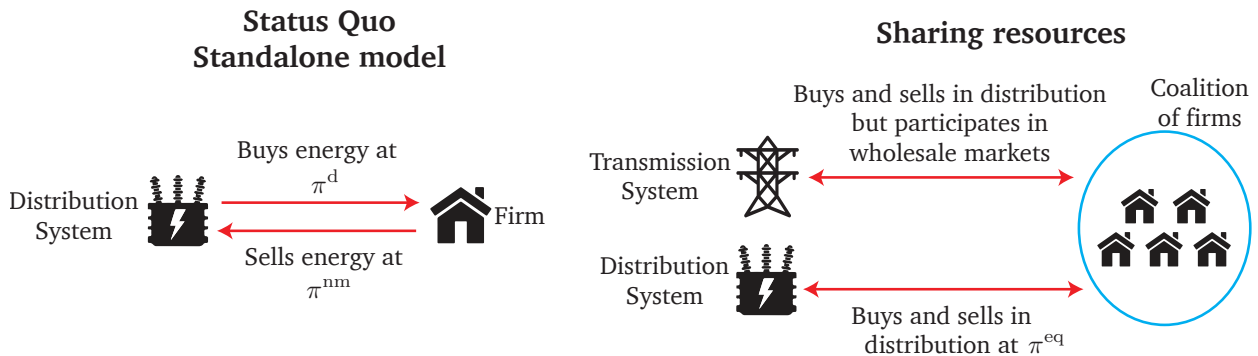
Figure 3.4: Options for how firms can buy and sell energy.

The three models considered are:

- The *standalone model* considers independent firms willing to invest in PV in which the excess generation is sold to the grid at a net-metering price π^{nm}, and the energy deficit is purchased at a retail tariff π^{d}.

- The *sharing or peer-to-peer model* studies how a collective of firms is willing to invest in PV when there exists a peer-to-peer market for trading energy.

- The *collective on wholesale markets* model considers coordinated PV investment for the collective where an aggregator can sell excess generation or purchase energy deficit in the wholesale market for the entire collective at a price π^{g}.

Figure 3.5 summarizes the three proposed models. The mathematical formulations of each model are presented in detail in the following subsections.
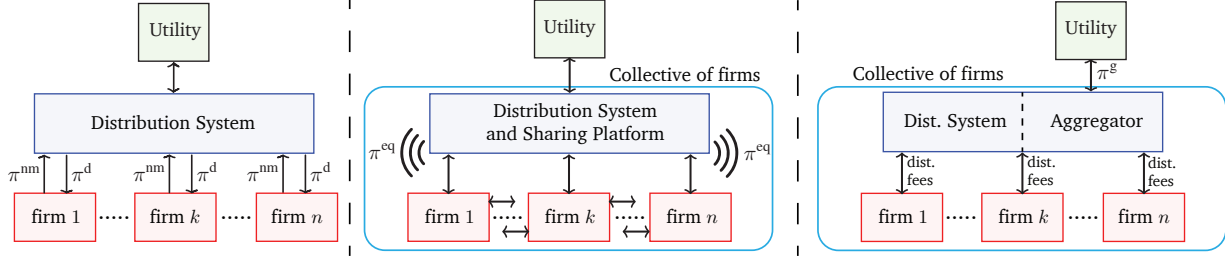
Figure 3.5: Proposed models: (a) left: *standalone problem*, (b) middle: *sharing or peer-to-peer scheme model*, (c) right: *collective on wholesale markets*.

3.2 Firms under a Standalone Net-Metering Market Scheme

We consider a single firm k that has to decide how much area a_k (m²) of PV panels to install depending on its own load ℓ_k, irradiance w_k, costs π_k^s and pricing π_k^d, π_k^{nm} (left side of Figure 3.5). The optimization problem for each user k, $\mathcal{P}_k^{sa}$, can be written as:

$$\min_{a_k} \; \tilde{J}_k(a_k) = \pi^s a_k + \overline{\mathbb{E}}[\pi^d(t)(\ell_k(t) - a_k w_k(t))^+] - \overline{\mathbb{E}}[\pi^{nm}(t)(a_k w_k(t) - \ell_k(t))^+] \qquad (3.4)$$

subject to:

$$0 \leq a_k \leq a_k^{max} \qquad\qquad\qquad (3.5)$$

$$\overline{\mathbb{E}}_{\mathcal{T}_m}[\ell_k(t) - a_k w_k(t)] \geq 0, \qquad\qquad \forall m \in \mathcal{M} \qquad (3.6)$$

$$\mathbb{E}[a_k w_k(t) - \ell_k(t)] \leq P_k^{max}, \qquad\qquad \forall t \in \mathcal{T} \qquad (3.7)$$

The objective function (3.4) minimizes installation costs on PV plus the costs of purchasing energy to the grid minus the income of selling energy at net-metering price. Equation (3.5) limits the investment decision to less than the maximum area available to install PV. Equation (3.6) does not allow firm k to be a net producer through a period (usually a month or a year). Equation (3.7) imposes that the investment decision should not violate, in expectation, injection limits denoted by P_k^{max}. P_k^{max} typically depends on the reliability of the distribution system or utility limitations. Both (3.6) and (3.7) can be cast as upper bounds of the variable a_k as:

$$a_k \leq \frac{\overline{\mathbb{E}}_{\mathcal{T}_m}[\ell_k(t)]}{\overline{\mathbb{E}}_{\mathcal{T}_m}[w_k(t)]} = a_m^{cap}, \qquad\qquad \forall m \in \mathcal{M} \qquad (3.8)$$

$$a_k \leq \frac{P_k^{\text{max}} + \mathbb{E}[\ell_k(t)]}{\mathbb{E}[w_k(t)]} = a_t^{\text{pcap}}, \qquad\qquad \forall t \in \mathcal{T} \qquad (3.9)$$

Defining

$$m_k = \min\left\{a_k^{\text{max}}, a_1^{\text{cap}}, \ldots, a_M^{\text{cap}}, a_1^{\text{pcap}}, \ldots, a_T^{\text{pcap}}\right\} \qquad (3.10)$$

the optimization problem can be simply cast as:

$$\min_{a_k} \ \tilde{J}_k(a_k) \ \text{ s.t. } \ 0 \leq a_k \leq m_k \qquad (3.11)$$

The solution for this problem when net-metering price is pegged to the retail electricity price is as follows:

Theorem 3 *Assume $\pi^{nm}(t) = \pi^d(t) \ \forall t \in \mathcal{T}$, and that prices π^d are independent of the irradiance w_k. Then, the optimal PV investment decision of household k under the standalone model $\mathcal{P}_k^{sa}$ is given by the threshold policy:*

$$a_k^* = \begin{cases} m_k & \text{if} & \overline{\mathbb{E}}[w_k(t)] > \pi^s/\overline{\mathbb{E}}\left[\pi^d(t)\right] \\ 0 & \text{else} \end{cases}$$

Proof: If the net-metering price is pegged to the retail electricity price, i.e. $\pi^{nm} = \pi^d$, the cost function simplifies to

$$\tilde{J}_k(a_k) = \pi^s a_k + \overline{\mathbb{E}}[\pi^d(t)(\ell_k(t) - a_k w_k(t))] \qquad (3.12)$$

Observe that this is linear in a_k with slope $(\pi^s - \overline{\mathbb{E}}[\pi^d w_k])$. The independence between π^d and ω_k yields the result. $\square$

In the case of discounted net-metering prices $\pi^{nm} < \pi^d$, the objective function $\tilde{J}_k(a_k)$ is convex (while not linear), and thus, the optimal investment decision a_k^* can be easily computed using historical data to form empirical expectations and solving it using convex optimization solvers. The convexity is shown as follows: Denote the net-load $x_k = \ell_k - a_k w_k$, and $\pi^{nm} = \gamma \pi^d$, with $\gamma \in [0, 1]$, each positive part term (at each time step) in the objective function (3.4) can be written as:

$$f(x_k) \ = \pi^d \max(0, x_k) - \pi^{nm} \max(0, -x_k) \qquad (3.13)$$
$$= \pi^d(\max(0, x_k) - \gamma \max(0, -x_k)) = \pi^d g(x_k) \qquad (3.14)$$

Note that the slope of $g(x_k)$ for $x_k < 0$ is given by γ, while for $x_k > 0$ the slope is given by 1. For values of $\gamma \in [0, 1]$, any line between two points will be above $g(x_k)$, preserving its convexity. For a slope bigger than 1 ($\gamma > 1$), the function g is non-convex (in fact, concave), since any line that connects $g(x_1)$ with $x_1 < 0$ and $g(x_2)$ with $x_2 > 0$, will be below the function g.

3.3 Collective of Firms under a Sharing (peer-to-peer) Market Scheme

Now, in this scenario, we study PV investment decisions of a firm under a *peer-to-peer or sharing economy business model*. The setting is depicted in the middle of Figure 3.5.

Individual firms

Each firm k may have a deficit of net-load $(\ell_k - a_k w_k)^+$ during some time slots. This energy deficit can be purchased from homes who have a surplus in the collective, or from the utility at a price π^{d} \$/kWh. Similarly, firms can have excess net generation $(a_k w_k - \ell_k)^+$ during some time slots. This can be sold to other homes, or returned to the utility under the net-metering price or feed-in-tariff π^{nm}.

Spot market for sharing excess PV generation

We study a simple spot market for sharing excess PV generation from firms. The collective supply S and demand D of shared electricity are

$$S = \sum_{k=1}^{n}(a_k w_k - \ell_k)^+, \quad D = \sum_{k=1}^{n}(\ell_k - a_k w_k)^+.$$

Consider the time slot t. If the supply $S(t)$ exceeds the collective demand $D(t)$, firms with excess solar generation will compete against each other, and as a result, the shared electricity will trade at the *floor price* offered by the utility. The *floor price* is the net-metering price or feed-in-tariff $\pi^{\mathrm{nm}}(t)$, assumed to be less than the utility price $\pi^{\mathrm{d}}(t)$. On the other hand, if the collective demand $D(t)$ exceeds the collective supply $S(t)$, homes with a net deficit of electricity will compete against each other, and so, the shared electricity will trade at the *ceiling price* $\pi^{\mathrm{d}}(t)$. These effects are illustrated in Figure 3.6.
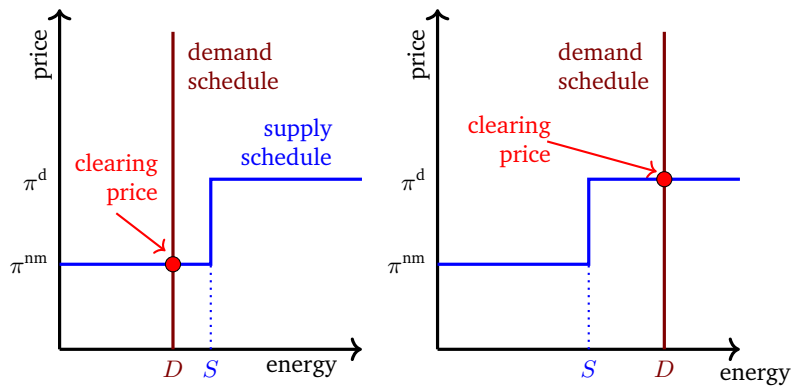
Figure 3.6: Clearing price for electricity in the spot market for the *sharing (peer-to-peer) scheme*. Left figure: Excess supply $S > D$; right figure: Excess demand $S < D$.

As a result, the spot market price for shared electricity in this competitive scenario is:

$$\pi^{\text{eq}}(t) = \begin{cases} \pi^{\text{nm}}(t) & \text{if} \quad S(t) > D(t) \\ \pi^{\text{d}}(t) & \text{else} \end{cases} \tag{3.15}$$

We stress that this clearing price is stochastic—it depends on market conditions in each time slot.

At each time slot $t \in \mathcal{T}$, we define the collective load $L(t) = \sum_k \ell_k(t)$, the collective generation $G(t) = \sum_k a_k w_k(t)$ and the collective net-load $X(t) = L(t) - G(t)$. Observe the following relationship (at any time slot t):

$$\begin{aligned} S - D &= \sum_{k \in \mathcal{N}} (a_k w_k - \ell_k)^+ - \sum_{k \in \mathcal{N}} (\ell_k - a_k w_k)^+ \\ &= \sum_{k \in \mathcal{N}} a_k w_k - \ell_k \\ &= G - L \\ &= -X \end{aligned}$$

Thus, the spot market price for shared electricity (3.15) can be re-written in terms of the collective net-load $X(t)$ as:

$$\pi^{\text{eq}}(t) = \begin{cases} \pi^{\text{nm}}(t) & \text{if} \quad X(t) < 0 \\ \pi^{\text{d}}(t) & \text{if} \quad X(t) \geq 0 \end{cases} \tag{3.16}$$

That is, in this competitive scenario, if the collective net-load is positive, the spot market price is the ceiling price $\pi^{\text{d}}(t)$. Otherwise, the price is traded at the net-metering or feed-in price.

Optimal investment decisions under sharing

We now deal with optimally invested PV in this peer-to-peer market scheme. Note that firm k's expected cost (per time slot) has three components:

$$J_k(a_k \mid a_{-k}) = \underbrace{\pi^{\text{s}} a_k}_{\text{capital cost}} + \underbrace{\overline{\mathbb{E}}\left[\pi^{\text{eq}}(\ell_k - a_k w_k)^+\right]}_{\text{cost of buying deficit}} - \underbrace{\overline{\mathbb{E}}\left[\pi^{\text{eq}}(w_k - a_k \ell_k)^+\right]}_{\text{revenue from sharing surplus}}$$

$$= \pi^{\text{s}} a_k + \overline{\mathbb{E}}\left[\pi^{\text{eq}}(\ell_k - a_k w_k)\right]. \tag{3.17}$$

We stress that the objective function for firm k depends on the spot market price π^{eq}, and hence on the collective net-load $X(t)$, and so the investment decisions a_{-k} of other households. This induces a *PV investment decision game*. The decision of each firm will affect the total net-load of the collective, which affects the clearing price as defined in

equation (3.16) and ultimately alters each firm's expected cost. For example, if a firm with
low irradiance is aware that there will be high PV investment from other firms (and hence
many hours in which $X(t) < 0$), then it is more convenient for the low irradiance firm
to not invest and purchase energy at a lower π^{nm} price. On the contrary, if no one in the
collective is willing to invest, it is possible that the optimal decision for that firm is to install
more PV. The social cost for this game is given by $J(\boldsymbol{a}) = \sum_k J_k(a_k \mid a_{-k})$.

As a first step we consider the case of common irradiance $w_k = w$, with no bound on
maximum panel area supported at each firm. The result is the following:

Theorem 4 *Assume that all firms receive common irradiance $w_k = w, \forall k$, a fixed retail price
$\pi^d(t) \equiv \pi^d, \forall t$ and a zero net-metering (feed-in) price $\pi^{nm}(t) = 0, \forall t$. Then:*

(a) *this game admits a unique Nash equilibrium,*

(b) *the optimal total investment $A = \sum_k a_k^*$ is the unique solution of:*

$$0 = \pi^s - \frac{\pi^d}{T} \sum_{t \in \mathcal{T}} p(t)\mathbb{E}\left[w(t) \mid L(t) > Aw(t)\right] \tag{3.18}$$

where $p(t) = Prob\{L(t) > Aw(t)\}$, or equivalently $p(t) = Prob\{X(t) > 0\}$.

(c) *at this Nash equilibrium, the optimal investment of firm k is:*

$$a_k^* = A \cdot \frac{\overline{\mathbb{E}[\ell_k \mid L = Aw]}}{\overline{\mathbb{E}[L \mid L = Aw]}} \tag{3.19}$$

(d) *this Nash equilibrium maximizes social welfare.*

Proof: With the assumption of no net-metering, common irradiance, fixed retail prices, and
expanding the average expectation, equation (3.17) reduces to:

$$J_k(a_k \mid a_{-k}) = \pi^s a_k + \frac{\pi^d}{T} \sum_{t \in \mathcal{T}} p(t)\mathbb{E}[\ell_k(t) - a_k w(t) \mid X(t) \geq 0] \tag{3.20}$$

We first show that a Nash equilibrium exists. Consider firm k, which investment decision
is a_k and fix the decisions of all the firms a_{-k}^* from equation (3.19), with A the solution of
equation of (3.18). To show that $\boldsymbol{a}^*$ is a Nash equilibrium, we have to show that a_k^* obtained
from equation (3.19) is indeed a global minimizer of $J_k(a_k \mid a_{-k}^*)$. Let $\alpha = \sum_{j \neq k} a_j^*$ the
investment of the other firms, and so $A = a_k + \alpha$. Given the common irradiance $\omega_k = \omega$,
observe that the condition $X \geq 0$ can be rewritten as:

$$L - Aw \geq 0 \rightarrow L \geq (\alpha + a_k)w \tag{3.21}$$

and so, considering any time slot t, in terms of the net-load $x_k = \ell_k - a_k w$, the cost function
can be written as:

$$J_k(a_k \mid a_{-k}) = \sum_{t \in \mathcal{T}} \left\{ \frac{\pi^{\text{s}}}{T} a_k + \frac{\pi^{\text{d}}}{T} p(t) \mathbb{E}\left[x_k(t) \mid L(t) \geq (\alpha + a_k) w(t) \right] \right\} \tag{3.22}$$

that can be written in terms of the distributions as:

$$J_k(a_k \mid a_{-k}) = \sum_{t \in \mathcal{T}} \left\{ \frac{\pi^{\text{s}}}{T} a_k + \frac{\pi^{\text{d}}}{T} \int_{\ell_k=0}^{\infty} \int_{w=0}^{\infty} \int_{L=a_k+\alpha}^{\infty} x_k f_{\ell_k,w,L}(\ell_k, w, L) d\ell_k dw dL \right\} \tag{3.23}$$

By taking the derivative (note that $dx_k/da_k = -w$) and using the Leibniz rule we get:

$$\frac{dJ_k}{da_k} = \sum_{t \in \mathcal{T}} \left\{ \underbrace{\frac{\pi^{\text{s}}}{T} - \frac{\pi^{\text{d}}}{T} p(t) \mathbb{E}[w(t)|L \geq (a_k + \alpha)w]}_{\phi_t(a_k)} - \underbrace{\frac{\pi^{\text{d}}}{T} f_L(a_k + \alpha) \, \mathbb{E}[\ell_k - a_k w \mid L = (a_k + \alpha)w]}_{\psi_t(a_k)} \right\} \tag{3.24}$$

Observe that for a_k^* obtained from (3.19), we obtain $a_k^* + \alpha = A$. Then from (3.18),
$\sum_t \phi_t(a_k^*) = 0$. Thus:

$$\frac{dJ_k}{da_k}(a_k^*) = -\pi^{\text{d}} f_L(A) \overline{\mathbb{E}}[\ell_k - a_k^* w \mid L = Aw] \tag{3.25}$$

$$= -\pi^{\text{d}} f_L(A) \overline{\mathbb{E}}[\ell_k | L = Aw] - \frac{\overline{\mathbb{E}}[\ell_k Aw | L = Aw]}{\overline{\mathbb{E}}[L | L = Aw]} \tag{3.26}$$

$$= 0 \tag{3.27}$$

that implies the derivative vanishes at a_k^*. Now observe that the function $\phi_t(a_k)$:

$$\frac{\pi^{\text{s}}}{T} - \frac{\pi^{\text{d}}}{T} \int_{\ell_k=0}^{\infty} \int_{w=0}^{\infty} \int_{L=a_k+\alpha}^{\infty} w f_{\ell_k,w,L}(\ell_k, w, L) d\ell_k dw dL$$

is monotone increasing on a_k, since increasing a_k decrease the value of the integral, and
hence, due to the negative sign, increase the value of $\phi_t(a_k)$. In addition, $\psi_t(a_k)$ is mono-
tone non-increasing, since increasing a_k can only increase solar production, reducing the
expected net-load (if $L = (a_k + \alpha)w$). Since $\psi_t(a_k)$ also vanishes at a_k^* we have for our
functions:

$$\phi_t(a_k) \begin{cases} < 0 & \text{if } a_k < a_k^* \\ = 0 & \text{if } a_k = a_k^* \\ > 0 & \text{if } a_k > a_k^* \end{cases} \qquad \psi_t(a_k) \begin{cases} \geq 0 & \text{if } a_k < a_k^* \\ = 0 & \text{if } a_k = a_k^* \\ \leq 0 & \text{if } a_k > a_k^* \end{cases}$$

Combining our results we obtain:

$$\frac{dJ_k}{da_k} \begin{cases} < 0 & \text{if } \quad a_k < a_k^* \\ = 0 & \text{if } \quad a_k = a_k^* \\ > 0 & \text{if } \quad a_k > a_k^* \end{cases}$$

that proves that a_k^* is the global minimizer of $J_k(a_k^* \mid a_{-k}^*)$, and hence establishing that
$\boldsymbol{a}^* = (a_1^*, \ldots, a_n^*)$ is a Nash equilibrium with a solution obtained from equations (3.18) and
(3.19). To show that this Nash equilibrium supports social welfare, consider the social cost
and considering the assumption that all firms receive same irradiance $w_k = w$:

$$J(A) = \pi^{\mathrm{s}} \sum_{k \in \mathcal{N}} a_k + \frac{\pi^{\mathrm{d}}}{T} \sum_{t,k} \mathbb{E}\left[\ell_k(t) - a_k w(t) \mid X(t) \geq 0\right]$$

$$= \pi^{\mathrm{s}} A + \frac{\pi^{\mathrm{d}}}{T} \sum_{t \in \mathcal{T}} \mathbb{E}\left[L(t) - A w(t) \mid X(t) \geq 0\right]$$

Setting the derivative to zero, yields equation (3.18), which shows that the Nash equilib-
rium supports social welfare. $\square$

Note that this result does not apply to the case where $\pi^{\mathrm{nm}} \neq 0$. This is a more challenging
case to analyze because the mathematical results are not as clean as the ones presented
in equations (3.18) and (3.19). However, we now explore a more realistic condition of
diverse irradiance, net-metering price different than zero, and assume that each firm k
can invest at most m_k m^2 of panel area due to physical limitations at the site (such as
rooftop size or power limitations). Assuming that a large number of n firms participate in
PV sharing we will have asymptotically (in n) perfect competition, in which no single firm
can influence the statistics of the clearing price π^{eq}, we have:

Theorem 5 *In the peer-to-peer or sharing economy business model, under the perfect com-
petition model (in which no single firm can influence the statistics of the clearing price π^{eq}),
optimal PV investment decisions of firm k are given by the threshold policy:*

$$a_k^* = \begin{cases} m_k & \text{if } \sum_t \left\{ p(t)\mathbb{E}\left[\pi^d(t) w_k(t) \mid X(t) > 0\right] + (1 - p(t))\mathbb{E}\left[\pi^{nm}(t) w_k(t) \mid X(t) < 0\right] \right\} > \pi^s T \\ 0 & \text{otherwise} \end{cases}$$

*where $X(t)$ is the net-load random sequence, $p(t) = Prob\{X(t) > 0\}$, and T is the number of
time slots.*

Proof: Expanding the expectation, the cost function (3.17) can be written as

$$J_k(a_k) = \pi^{\mathrm{s}} a_k + \overline{\mathbb{E}}[\pi^{\mathrm{eq}}(\ell - a_k w_k)^+] \tag{3.28}$$

$$= \pi^{\mathrm{s}} a_k + \frac{\pi^{\mathrm{d}}}{T} \sum_t p(t) \mathbb{E}[\ell_k(t) - a_k w_k(t) \mid X(t) > 0]$$

$$- \frac{\pi^{\mathrm{d}}}{T} \sum_t (1 - p(t)) \mathbb{E}[a_k w_k(t) - \ell_k(t) \mid X(t) < 0] \tag{3.29}$$

Note that because of the perfect competition model, the cost function for household k
depends only on its own investment decision a_k. This cost function is linear in the decision

variable a_k with slope

$$\phi = \pi^{\mathrm{s}} - \frac{\pi^{\mathrm{d}}}{T}\sum_t p(t)\mathbb{E}[w_k(t) \mid X(t) > 0] - \frac{\pi^{\mathrm{nm}}}{T}\sum_t p(t)\mathbb{E}[w_k(t) \mid X(t) < 0] \qquad (3.30)$$

As a result, the optimal investment is $a_k^* = 0$ if this slope $\phi > 0$, and $a_k^* = m_k$ otherwise. This can be rearranged to yield the threshold policy of Theorem 5.

Remark 1: If the load ℓ_k and irradiance w_k are stationary random sequences, then $p(t) = p$ is independent of t. In this case, for fixed retail prices, the threshold policy of Theorem 5 becomes:

$$a_k^* = \begin{cases} m_k & \text{if} \quad p\pi^{\mathrm{d}}\mu_k + (1-p)\pi^{\mathrm{nm}}\nu_k > \pi^{\mathrm{s}} \\ 0 & \text{else} \end{cases} \qquad (3.31)$$

The quantity $\mu_k := \overline{\mathbb{E}}[w_k \mid X > 0]$ captures the value of PV for firm k when the collective is in deficit, while the quantity $\nu_k := \overline{\mathbb{E}}[w_k \mid X \leq 0]$ captures the value when the collective has an excess of supply. The value $\zeta_k := p\pi^{\mathrm{d}}\mu_k + (1-p)\pi^{\mathrm{nm}}\nu_k$ captures the *merit of firm* k over the time horizon.

Remark 2: Now, suppose we further assume that there is no net-metering (i.e. $\pi^{\mathrm{nm}} = 0$). In this case, the threshold policy of Theorem 5 becomes

$$a_k^* = \begin{cases} m_k & \text{if} \quad \mu_k = \mathbb{E}[w_k \mid X > 0] > \theta \\ 0 & \text{else} \end{cases} \qquad (3.32)$$

where the threshold θ is the unique solution of

$$\theta = \frac{\pi^{\mathrm{s}}}{\pi^{\mathrm{g}}p} \qquad (3.33)$$

The quantity $\mu_k = \mathbb{E}[w_k \mid X > 0]$ *captures the value of PV for home* k. This home will invest the maximum possible if $\mu > \theta$, and not invest otherwise.

Computing the threshold policy

Computation of the threshold in Theorem 5 is not trivial. Observe that this threshold determines PV investment of firms, which influences the statistics of the collective net-load X, which, in turn, affects the threshold. Here, we proposed a convergent algorithm that jointly computes the threshold condition and investment decisions a^*. Define the index sets of firms

$$\begin{aligned} \mathbb{S} &= \text{firms that elect to invest in PV} = \{k : a_k = m_k\} \\ \mathbb{T} &= \text{firms that elect not to invest in PV} = \{k : a_k = 0\} \end{aligned}$$

Algorithm 1 Collective of firms investing in PV

1: **Initialization:**
2: Compute maximum generation for each firm $\bar{g}_k := \overline{\mathbb{E}}[m_k w_k]$.
3: Sort the firms by $\bar{g}_k$ on descending order.
4: Start with $\mathbb{S} = \mathbb{T} = \varnothing$ and add the upper half of the sorted firms to the set $\mathbb{S}$, while the bottom
   half to the set $\mathbb{T}$.
5: **for** iteration $i = 1, \ldots$ **do**
6:     Compute the collective generation $G(t) = \sum_{k \in \mathbb{S}} m_k w_k(t)$.
7:     Compute the probability of deficit $p = \Pr\{L > G\}$.
8:     **for** firms k on $\mathbb{S}$ **do**
9:         Compute merit of site k as $\mu_k = \overline{\mathbb{E}}[w_k \mid X > 0]$, $\nu_k = \overline{\mathbb{E}}[w_k \mid X \leq 0]$ and $\zeta_k = p\pi^{\mathrm{d}}\mu_k + (1 -
           p)\pi^{\mathrm{nm}}\nu_k$.
10:        If $\exists k : \zeta_k < \pi^{\mathrm{s}}$, pick firm k^{L} with the minimum ζ_k and remove it from the set $\mathbb{S}$.
11:    **end for**
12:    **for** firms k on $\mathbb{T}$ **do**
13:        Compute merit of site k as $\mu_k = \overline{\mathbb{E}}[w_k \mid X > 0]$, $\nu_k = \overline{\mathbb{E}}[w_k \mid X \leq 0]$ and $\zeta_k = p\pi^{\mathrm{d}}\mu_k + (1 -
           p)\pi^{\mathrm{nm}}\nu_k$.
14:        If $\exists k : \zeta_k > \pi^{\mathrm{s}}$, pick firm k^{H} with the maximum ζ_k and remove it from the set $\mathbb{T}$.
15:    **end for**
16:    Add firm k^{L} to the set $\mathbb{T}$ and firm k^{H} to set $\mathbb{S}$.
17:    Halt if no firms are moving or the same moves are being done after two iterations.
18: **end for**
19: Solve the standalone case for indecisive firms, which are the last firms on changing between
    sets.

Algorithm 1 iteratively updates the set of firms that invest and do not invest in order
to determine the threshold condition and the decision $\boldsymbol{a}^*$ based on the threshold policy
(3.31). The algorithm initializes the set $\mathbb{S}$, by adding the best firms without considering
the collective deficit, and initializes the set $\mathbb{T}$ using the other ones. With this, an iterative
process starts, which computes the threshold policy and the worst firm $k \in \mathbb{S}$, i.e. the firm
with the minimum value $p\pi^{\mathrm{d}}\mu_k + (1 - p)\pi^{\mathrm{nm}}$ that is less than π^{s}, is removed from the set
$\mathbb{S}$ and added to the set $\mathbb{T}$. On the other hand, the best firm $k \in \mathbb{T}$, i.e. the firm with the
maximum value $p\pi^{\mathrm{d}}\mu_k + (1 - p)\pi^{\mathrm{nm}}$ that is greater than π^{s}, is removed from $\mathbb{T}$ and added
to $\mathbb{S}$. This process is repeated until no changes of firms occur or the same changes are
occurring after two iterations.

3.4   Collective of Firms under a Wholesale Market Scheme

In this scenario we explore the PV investment decisions of the collective, when it is co-
ordinated and participate in wholesale market for purchasing and selling energy to the
grid. This case is depicted on the right in Figure 3.5. We study the problem in which

a centralized planner, like an aggregator, can decide the optimal PV investment for each firm a_k. In practice, the centralized planner will decide where to invest, and will promote through incentives, typically lower electricity bills, the optimal investment decisions of the participants. In this case, the key difference is that a collective of users is subjected to the wholesale market price $\pi^g(t)$, instead of a retail tariff π^d.

Decision problem for the planner

The problem for the centralized planner can be written as:

$$\min_{\boldsymbol{a}} \hat{J}_c = \sum_{k \in \mathcal{K}} \left\{ \pi^s a_k + \overline{\mathbb{E}}[\pi^g(t)(\ell_k(t) - a_k w_k)] \right\} + d_{\text{fee}}(\boldsymbol{a})$$

$$\text{s.t.} \qquad 0 \leq a_k \leq m_k, \quad \forall k = 1, \ldots, n.$$

In this problem we consider that the collective is still under the domain of a utility, and hence a distribution fee $d_{\text{fee}}(\boldsymbol{a})$ is considered in addition of the wholesale market price. Usually, a retail tariff π^d has additional fees that are lumped on the price on top of the pure wholesale market price, to cover distribution costs for the utility. In this work, distribution fees are modeled as a combination of three different schemes:

$$d_{\text{fee}}(\boldsymbol{a}) = \alpha_1 \overline{\mathbb{E}} \left\{ \left| \sum_{k \in \mathcal{K}} \ell_k(t) - a_k w_k(t) \right| \right\} + \alpha_2 \overline{\mathbb{E}}_{\mathcal{M}} \left\{ \max_{t \in \mathcal{T}_m} \left| \sum_{k \in \mathcal{K}} \ell_k(t) - a_k w_k(t) \right| \right\} + \alpha_3 n \quad (3.34)$$

The first term represents a volumetric cost for using the grid (independent if its injecting or withdrawing). The second term depicts a demand charge, in which the collective pays a fee over a period (usually a month) that depends on the maximum consumption or injection in that period. Finally, the third term represents a connection cost that depends on the total users in the collective. A key aspect here is that the collective is subjected to lower wholesale market electricity aspects, but there are additional fees for using the distribution system.

Solution under a price taker aggregator

It is assumed that $\pi^g(t)$ does not depend on the investment decisions of the collective, i.e. the collective is considered a price-taker entity. Thus, using empirical expectations, the previous problem is a convex problem, that can be recast as a linear program by adding sufficient slack variables to replace the terms with absolute value and max functions of the distribution fees.

3.5 Numerical Simulations

In this section we use simulations to assess how solar adoption differs in the proposed three models: (a) a standalone net-metering scenario, (b) a shared solar model and (c)

a collective participating in wholesale markets. We consider a collective of 1,000 firms, optimized using Python and cvxpy with the Gurobi solver [28, 37].

Data

- *Load and effective irradiance.* We construct empirical expectations for household electricity use and solar production with 2017 data from homes in the same neighborhood in Texas, taken Pecan Street's Dataport [104]. We normalize solar production using each system's nominal capacity, that is, actual production is eventually rescaled in proportion to a_k.

  We generate 1000 synthetic profiles with 194 load and solar profiles from the database by randomly selecting combinations of solar and load time series and adding white noise with variance $\sigma^2 = 0.2$ (kWh)^2 to all non-zero values, while ensuring non-negativity after the addition.

- *Prices.* We use a levelized cost of 2.80 $/W$_{DC}$ for installed PV systems (including balance of system costs and inverter) [34]. Assuming a typical panel is 165×99 cm (1.64 m^2) and 300 W$_{DC}$ [82] we compute that firms face an investment cost of 512.2 $/m^2. Using a real interest rate r of 5% and a time horizon of 20 years, we obtain an annuity of 41.1 $/m^2, or π^s of 0.0047 $/m^2 per hour.

  We use a retail price π^d of 0.18 $/kWh and a net-metering price π^{nm} of $\gamma\pi^d$ for the standalone model, with $\gamma \in [0,1]$. In the sharing (peer-to-peer) economy business model we set $\pi^{nm} = 0$ (no net-metering). Indeed, our objective is to argue that the sharing economy model can supplant net-metering in some (likely) future scenario when utilities withdraw these programs. Finally, we use historical wholesale electricity prices $\pi^g(t)$ from Texas in 2017 [104].

- *Limits.* Annual firm-level production is uncapped for the sharing economy and wholesale market models (while capped for the standalone model). That is, we set the annual cap $a^{cap} = \infty$, from equation (3.8), for both the sharing economy and wholesale market, ignoring that constraint. However, the constraint is considered for the standalone model. Finally, the instantaneous power injection is uncapped in all models, and hence equation (3.7) is not considered in any model.

Results

Case 1. Low net metering price and investment

The objective of this case is to show how a lower-than-retail net metering price limits investment in the standalone case compared to the sharing case. To remove the influence of the annual production cap, we limit roof area for all customers, setting $a_k^{max} = \beta_1 a_k^{cap}$, $\forall k$, with $\beta_1 = 0.2$. We vary γ, i.e., the net-metering price as a proportion of the retail tariff

$\pi^{\mathrm{nm}} = \gamma \pi^{\mathrm{d}}$ for the standalone case. We stress that $\pi^{\mathrm{nm}} = 0$ for the sharing (peer-to-peer) business model, in all scenarios of γ.

Figure 3.7 depicts the difference in investment in PV between the models, calculated as:

$$D(\gamma) = \frac{\sum_k a_k^{*,\mathrm{sharing}} - \sum_k a_k^{*,\mathrm{standalone}}(\gamma)}{\sum_k a_k^{*,\mathrm{standalone}}(\gamma)} \ [\%] \tag{3.35}$$
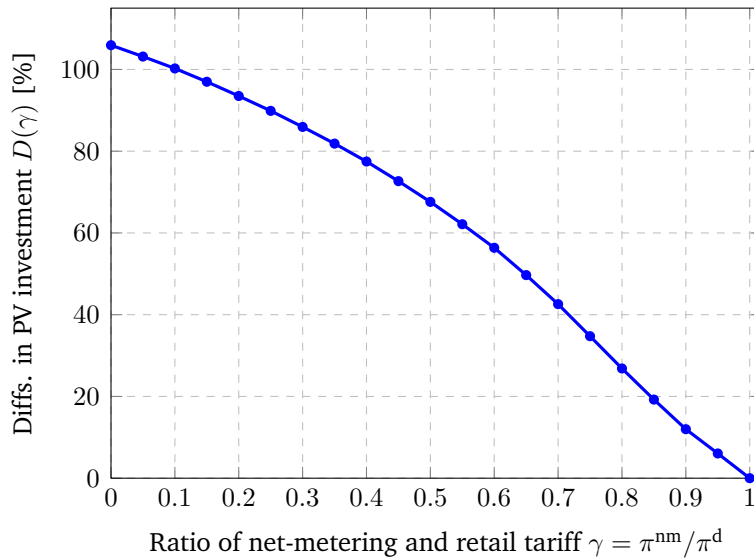
Figure 3.7: Differences of PV investment in *Case 1*. Net-metering prices $\pi^{\mathrm{nm}} = \gamma \pi^{\mathrm{d}}$ only vary for the standalone case.

For $\gamma < 1$, PV investment is greater for the sharing economy model. This is because, for a low maximum panel area, optimal investment decisions of the collective in the sharing model will never yield a negative collective net-load, at any hour of the day (i.e. $X(t) > 0, \forall t \in \mathcal{T}$). This implies that each firm in the collective that invests in PV always receives the full retail price when selling excess generation. On the contrary, for the standalone case, even at small area installations, firms have hours in which their own net-load is negative as depicted in Figure 3.8.

When net-load is negative, firms face a discounted selling price, and this discount reduces their optimal PV investment. The lower the net-metering price, the more convenient becomes for users to engage in a sharing scheme, since they are getting paid full retail tariff π^{d} given that $X > 0$. For the data analyzed, over 100% difference in investment is observed for the case on which both standalone and sharing schemes face zero net-metering price $\pi^{\mathrm{nm}} = 0$.

Finally, investment is the same if there is no discount, i.e. $\gamma = 1$. In such case, threshold policies of Theorem 1 and Theorem 3 are equivalent, providing the same optimal PV
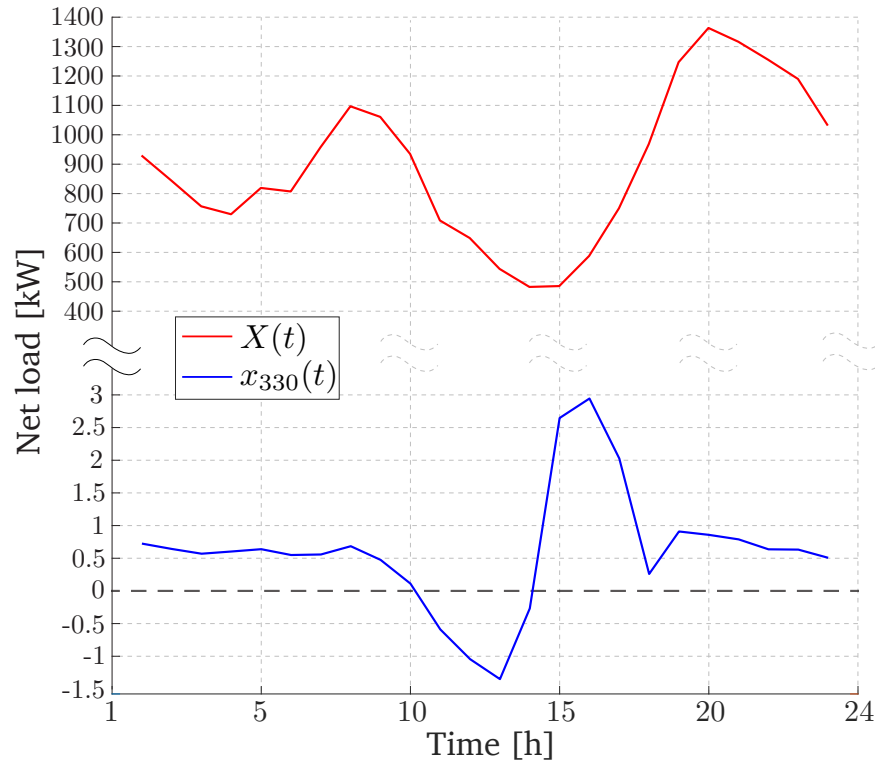
Figure 3.8: Comparison of net-load of the firm with id 330 (blue) and the collective (red) on February 1st for *Case 1*. Hourly collective net-load $X(t)$ is positive throughout the year, but individual firms can have negative net-load x_k in some hours of the year.

investment solution, since $X(t) > 0, \forall t$, and hence each firm in the sharing model always faces $\pi^{\text{eq}}(t) = \pi^{\text{d}}(t), \forall t$, as in the standalone case with $\gamma = 1$.

Case 2. Effects of the annual cap a_k^{cap}

Our aim is to study how the annual production cap a_k^{cap} influences investment decisions in the standalone model (this cap does not apply in the sharing model). We set $a_k^{\text{max}} = \beta_2 a_k^{\text{cap}}, \forall k$, with $\beta_2 > 1$. According to our earlier results, firms in the sharing model are limited by the maximum area available to invest $a_k^{\text{max}} = m_k = \beta_2 a_k^{\text{cap}}$. However, in the standalone model firms are limited by the annual cap $m_k = a_k^{\text{cap}}$. Figure 3.9 depicts the comparison of cumulative investment on PV between the two models using $\gamma = 0.9$ and $\beta_2 = 1.5$. In the Figure, a low number on the horizontal axis corresponds to a firm with high irradiance.

We note two findings in Figure 3.9:

- First, firms with high irradiance *under-invest* in the standalone case relative to the sharing case due to the annual cap: The slope of the investment curve is lower for high
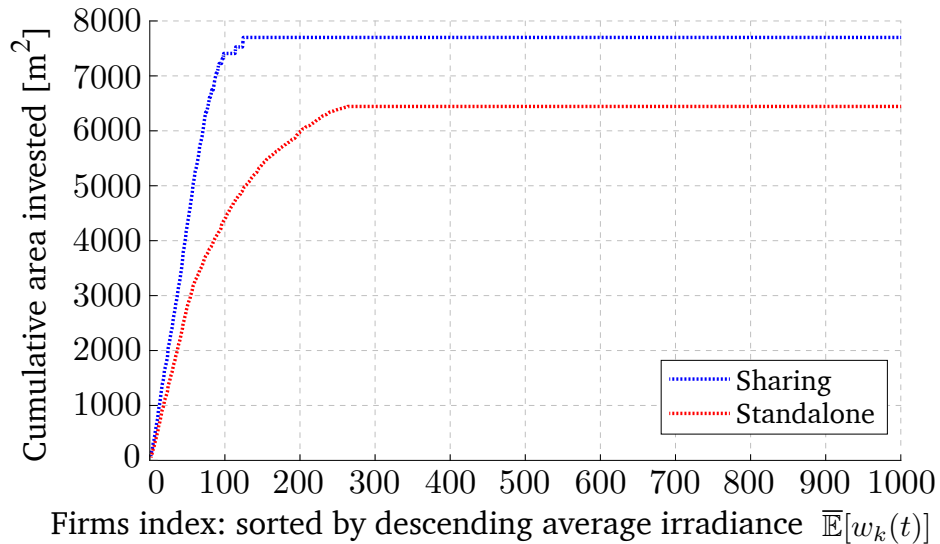
Figure 3.9: Comparison of total investment decision between the standalone and sharing
model with $\gamma = 0.9$ and $\beta_2 = 1.5$.

irradiance firms in the standalone case. Higher slope in the sharing model implies
that individual firms are investing more in PV due to the removal of the annual cap.

- Second, firms with intermediate irradiance *over-invest* in the standalone case, as
  observed in the slope of the red line for $k \in [120, 260]$, as its favorable for their private
  economics.

  To confirm this effect, a second simulation was run using $\gamma = 0.8$, and $\beta_2 \sim U[1.5, 3.0]$
  was chosen randomly for all firms. This represent a case when there is a large
  maximum available panel area to install relative to the annual cap in the standalone
  model. Figure 3.10 presents the investment decision of each firm in both sharing
  and standalone case. As can be seen in this case, firms with higher irradiance in the
  standalone model are not able to invest as much as they want, given the annual cap.
  In addition, some firms ($k > 200$) invest in the standalone case, while they do not
  invest in the sharing case. This confirms that such firms *over-invest* in such schemes,
  given that it is still favorable for their private economics.

In addition, we analyze the reduction in total costs (or increase in total welfare) of the
community between the standalone and sharing models for Case 2. We note that there is
a reduction of 23.4% of the total cost for the community. More interestingly, we compare
the total cost reduction for each firm between the two models. Figure 3.11 depicts the cost
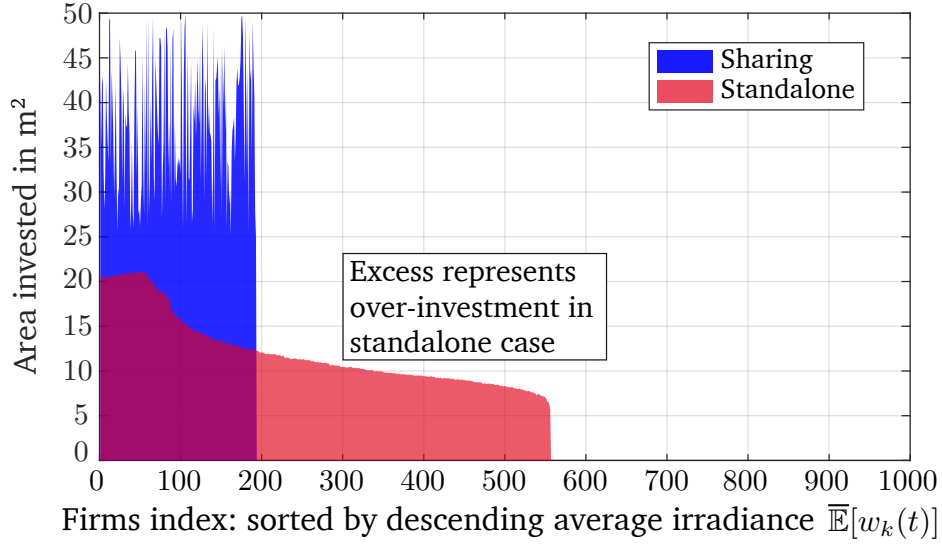
Figure 3.10: Comparison of individual investment decision between the standalone and sharing model with $\gamma = 0.8$ and $\beta_2 \sim U[1.5, 3.0]$.
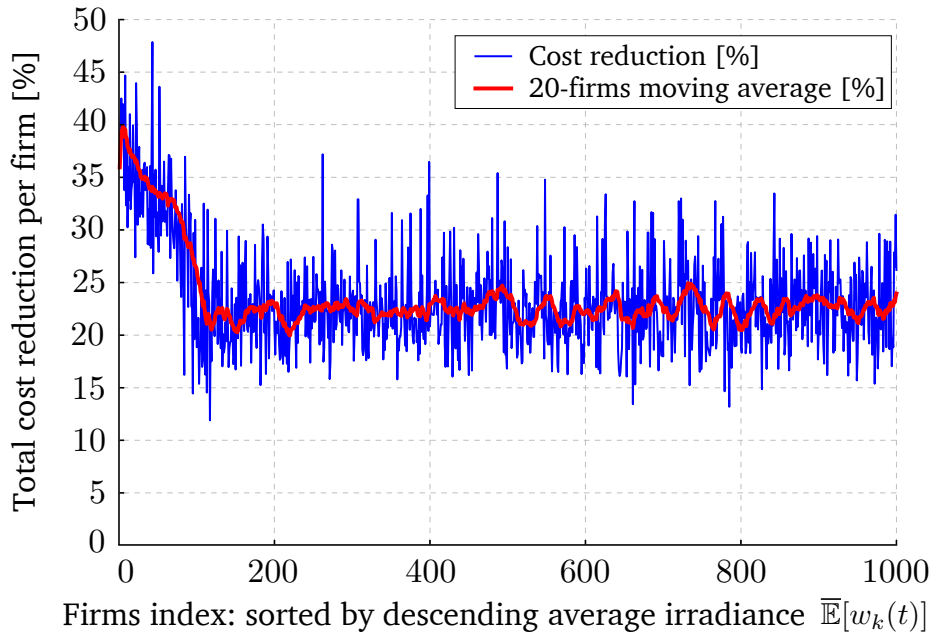
Figure 3.11: Comparison of the total cost reduction per firm between the sharing and standalone model with $\gamma = 0.9$ and $\beta_2 = 1.5$.

reduction for each firm between the standalone and sharing models, computed as:

$$\text{Cost Reduction for firm } k \ [\%] = \frac{\tilde{J}_k\left(a_k^{*,\text{standalone}}\right) - J_k\left(a_k^{*,\text{sharing}} \mid a_{-k}^{*,\text{sharing}}\right)}{\tilde{J}_k\left(a_k^{*,\text{standalone}}\right)} \tag{3.36}$$

again using $\gamma = 0.9$ and $\beta_2 = 1.5$. The simple moving average of 20 firms is also provided to showcase the trend of such cost reduction as the average irradiance per firm decreases.

We note two key findings in Figure 3.11:

- First, all firms are better off in the sharing case than in the standalone case. The cost reduction is always positive and at least of 12%. This implies that no firm benefits from leaving the community for a standalone setup.

- Second, the trend is that firms with more irradiance yield higher benefits, with cost reductions of over 35% in some cases. In sum, for the parameters and data we use in *Case 2*, the number of firms that invests in the sharing case is smaller by roughly 50%, but the total area invested is higher by roughly 20%. Additionally, everyone reduces their total cost by at least 12%, and 23.4% on average, in comparison to the standalone case.

Case 3. Effects of solar prices π^s

We now explore the effects of varying the amortized cost of solar PV on total investment decisions. To show the importance of tariff design, we also consider a scenario where PV owners are simply paid the wholesale market price. Figure 3.12 depicts the comparison under different PV costs π^s. We set $\pi^{nm} = 0$ for both sharing and standalone ($\gamma = 0$) models, and $\beta_2 = 1.1$ to consider a small effect on the annual cap for the standalone model.

Some important results to highlight from Figure 3.12:

- We first note that investments only occur in wholesale market models for lower values of π^s, in comparison to both standalone and sharing models. Since the wholesale market price π^g is usually smaller than the retail tariff π^d, the revenue obtained for the owner is lower than the standalone/sharing cases when the selling price is π^d. This highlights that currently, most of the investment in distributed/residential PV is driven by higher retail and selling prices. If distributed users are subjected to wholesale prices for purchasing/selling energy, given current distributed PV prices ($\pi^s = \pi^s_{nom} = 0.0047$ \$/m^2), then no investment will occur.

- Second, we observe that if PV is compensated at only the wholesale price ($\alpha_2 = 0$), the optimal investment decisions for the parameters chosen are sensitive to PV costs, going from the maximum possible investment to zero around $\pi^s/\pi^s_{nom} = 0.2$.

- Third, we note that charging at the wholesale market price only does not capture the total distribution costs for the utility. Therefore we also consider a case with a monthly demand charge, which we set to $\alpha_2 = 10$\$/kW. In such scenarios PV investment can offset this new charge. Without PV investment, these demand charges represent 45% of total costs of the collective, which is in line with existing utility cost structures [15].

  As shown in the black line in Figure 3.12, at a higher PV cost $\pi^s/\pi^s_{nom} > 0.2$, there is more investment in PV than in the no additional fees case (in green). This is
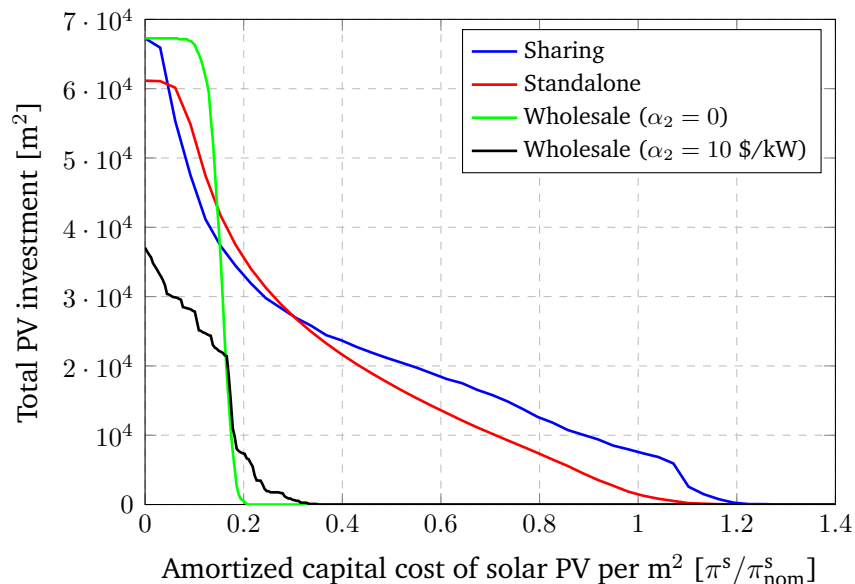
Figure 3.12: Total PV investment among different models when varying the amortized capital cost of PV π^s in Case 3. The x-axis is the ratio of amortized cost against the nominal solar PV cost $\pi^s_{nom} = 0.0047$ \$/m^2 (per time slot).

because the generation from the extra PV investment decreases net-load, effectively diminishing the impact from the demand charge α_2. On the other hand, similar investment is observed between 10^4 to $2 \cdot 10^4$ m, since more investment does not further reduce the demand charge, since now the peak net-load is outside sunny hours.

Finally, at lower costs of PV (< 0.18), there is a smaller investment in PV in comparison to the green line, since for a sufficiently high investment in PV, the collective now has a peak net injection at sunny hours. This increases the payment for demand charge when more PV is deployed due to a maximum net peak injection (see equation (3.34)). Thus, even at low prices of solar, for the collective it is not optimal to invest its maximum PV capacity at the considered demand charge rate.

3.6 Discussion and Conclusions

The simulations results in the previous section highlight the main contributions of this work—the insights and drivers for PV investment. First, as illustrated by *Case 1* and *Case 2*, differences between investment models are strongly influenced by the area available each customer has for PV panels. When this area is low, customers with favorable economics install their maximum in both the standalone and sharing cases as in *Case 1* with $\gamma = 1$.

When the net-metering price is lower than the retail tariff (i.e. $\gamma < 1$), results indicate that there is larger PV investment in the sharing case due to the effect of negative net-load only for individual firms, but not for the collective (see Figure 3.8).

Second, when the available area constraint is inactive and the annual cap constraint is active, in the standalone model a fraction of customers under-invest while others over-invest relative to sharing case. Under-investors exist due to their annual production cap when net-metering is available, or a lack of remuneration when net-metering is unavailable. On the other hand, over-investors exist because, although their merit is worse than others in the community, for their private economics solar remains cheaper than retail electricity (see slopes in Figure 3.9 for *Case 2*). In addition, as illustrated by Figure 3.11, firms prefer to stay in the sharing (or P2P) case rather than in the standalone one. The specific cost reduction is highly dependent on the load and irradiance of each firm, but for the parameters used in *Case 2*, on average firms are 23.4% better off than in the standalone model.

Moreover, results in a wholesale market scheme, as in *Case 3*, show that distributed PV investment is mostly driven by higher retail and selling prices. As depicted in Figure 3.12, lower PV costs are required to promote PV investment under wholesale market prices. The inclusion of additional fees, such as a demand charge, can lead to more PV investment in the wholesale market model, but in the cases we examined net-metering at retail prices always leads to more PV investment. For the parameters used in *Case 3*, we require at least 60% of solar cost reduction ($0.4\pi^{\mathrm{s}}_{\mathrm{nom}}$) to observe the first unit of investment in PV in a wholesale market setting.

As concluding remarks, in this work we study optimal investment decision for distributed PV under three models:

(a) a standalone net-metering model with annual production cap,

(b) a sharing economy or peer-to-peer model where firms can trade excess generation in a local spot market and,

(c) a wholesale market participation model, in which an aggregator can promote PV investment.

In the standalone model (a) each firm makes independent investment decisions based on their own load and irradiance profiles. Under the sharing scheme (b), optimal investment decisions are coupled as they affect the clearing price on the local spot market. For a large number of firms we have asymptotically perfect competition, and we show that optimal investments are determined by a threshold policy that can be computed using Algorithm 1. In the wholesale market model (c), an entity decides the investment for each firm, that are coupled due to the distribution fees for the entire collective.

We present experiments using load and irradiance data to investigate how decisions depend on area availability, annual production caps and distribution fees. For low total PV investment, we find the sharing and standalone models yield the same results under a full

net-metering scenario. For discounted net-metering pricing, the sharing model supports a higher investment in PV than the standalone framework. In the case of high total PV investment, there are hours where the collective net-load is negative, changing the distribution of firms that invest in the sharing model in comparison to the standalone case. We also show that, in a case where PV is remunerated only at wholesale costs, given current costs of PV and low wholesale energy prices, no PV investment occurs. This highlights the importance of high retail tariffs to make distributed PV investment attractive for firms. Finally, we show how the inclusion of demand charge, in a scenario of low PV installation costs, can change the optimal PV investment in a wholesale market participation model. These fees need to be considered if a future scenario includes these types of distribution fees for collectives.

As future work, interesting extensions to this work are related to analyzing the impacts of different solar investments considering physical constraints of the distribution system, designing a sharing model framework to buy and sell energy for isolated communities or when contingencies occur and the collective is disconnected from the grid (i.e. no retail tariff). Part of this work was already explored by our research group in the paper [70]. Other future directions include studying how energy sales are impacted for a utility when firms invest in PV under different market structures; and address fairness and equity issues in the collective participating in these markets.

Chapter 4

Electric Vehicle Flexibility on 2050 Low-Carbon Energy Scenarios for California

In the important effort to keep global temperatures within certain limits and tackle the climate crisis, future electric systems will move into having high shares of RESs, such as solar and wind. These energy sources have inherent characteristics of variability and volatility that pose significant challenges in power systems. In particular, balancing generation with demand is a crucial aspect that must be satisfied at all times to ensure secure and reliable operation of the electric grid.

To study how power systems will look in the future we rely in expansion planning models. These consider a simplified model of the power system to decide *what* types of energy technology, *where*, and *when* to install system infrastructure, such as transmission lines, generators or energy storage [35]. The main purpose of these models is to understand the effects of policy and investment decisions in the evolution and operation of future power systems.

Given the high level of complexity of energy systems, it becomes very difficult to create representative models for long-term horizons, and hence several simplifying assumptions are used to capture specific aspects with varying levels of detail. For example, traditional expansion planning models usually do not capture the chronological sequence of times, using load duration curves (or time-slices) to represent the amount energy necessary to supply throughout the time-horizon. Similarly, spatial representation of infrastructure usually is neglected, or heavily simplified, that can misrepresent transmission congestion.

Most modern expansion planning models use optimization approaches to optimally decide which infrastructure must be installed in the system, while satisfying specific policy and/or reliability constraints. Figure 4.1 summarizes the most common objectives and constraints on traditional expansion planning models. Figure 4.1 presents both generation and transmission as separated problems, but novel formulations usually combine both generation and transmission expansion planning in a single optimization problem.

```
┌ ─  ─  ─  ─  ─  ─  ─  ─  ─  ─  ─  ─  ─  ─  ─  ─  ─  ─ ┐
        Traditional Expansion Planning Models

  ┌──────────────────────────────┐   ┌──────────────────────────────┐
  │  Generation Expansion Planning │   │ Transmission Expansion Planning │
  │                                │   │                                │
  │  ┌──────────────────────────┐  │   │  ┌──────────────────────────┐  │
  │  │ Minimize:                │  │   │  │ Minimize:                │  │
  │  │   Investment Cost + Operational Costs │ │   Investment Cost + Operational Costs │
  │  └──────────────────────────┘  │   │  └──────────────────────────┘  │
  │  s.t.                          │   │  s.t.                          │
  │   ┌────────────────────────┐   │   │   ┌────────────────────────┐   │
  │   │ Satisfying Expected Demand │ │   │ Power balance for each node │ │
  │   ├────────────────────────┤   │   │   ├────────────────────────┤   │
  │   │ Security Constraints (LOLP & Reserves) │ │ Network model (transport, AC/DC) │
  │   ├────────────────────────┤   │   │   ├────────────────────────┤   │
  │   │ Limiting generation to installed capacity │ │ Power limits on lines │
  │   ├────────────────────────┤   │   │   ├────────────────────────┤   │
  │   │ Generation output for each unit │ │ Security constraints (contingencies) │
  │   ├────────────────────────┤   │   │   ├────────────────────────┤   │
  │   │ Installation schedule limitations │ │ Budget constraints │
  │   ├────────────────────────┤   │   │   ├────────────────────────┤   │
  │   │ Budget constraints │      │   │   │ Pre-existence constraints │  │
  │   └────────────────────────┘   │   │   └────────────────────────┘   │
  │           •                    │   │           •                    │
  │           •                    │   │           •                    │
  │           •                    │   │           •                    │
  └──────────────────────────────┘   └──────────────────────────────┘
└ ─  ─  ─  ─  ─  ─  ─  ─  ─  ─  ─  ─  ─  ─  ─  ─  ─  ─ ┘
```

Figure 4.1: Common objectives and constraints in traditional generation and transmission expansion planning models. Figure adapted from [35].

The fundamental challenge of expansion planning models is to consider the relevant aspects of a specific study with a sufficient level of depth while keeping computational tractability [106]. Given this, a proper tuning of time and space scales is critical to resulting optimization problems are solvable in reasonable times, even for convex formulations. In addition, a trade-off exists when considering sources of uncertainty, such as future fuel prices or renewable energy production. The usage of stochastic optimization can provide reliable solutions with respect to the represented uncertainty, but can hid the analysis for more fundamental aspects of the problem while creating tractability issues. Thus, there are multiple tools and models that can support the analysis of different energy policies and future scenarios, but understanding the nuances is crucial for finding the appropriate model for each study case and specific policy questions. Figure 4.2 summarizes this challenge for a future WECC and California scenario.

In this chapter we will study the investment decisions for both generation and transmission, in future WECC and California by 2050, by exploring different policies and their effects on those infrastructure decisions. The main contributions of this chapter are:
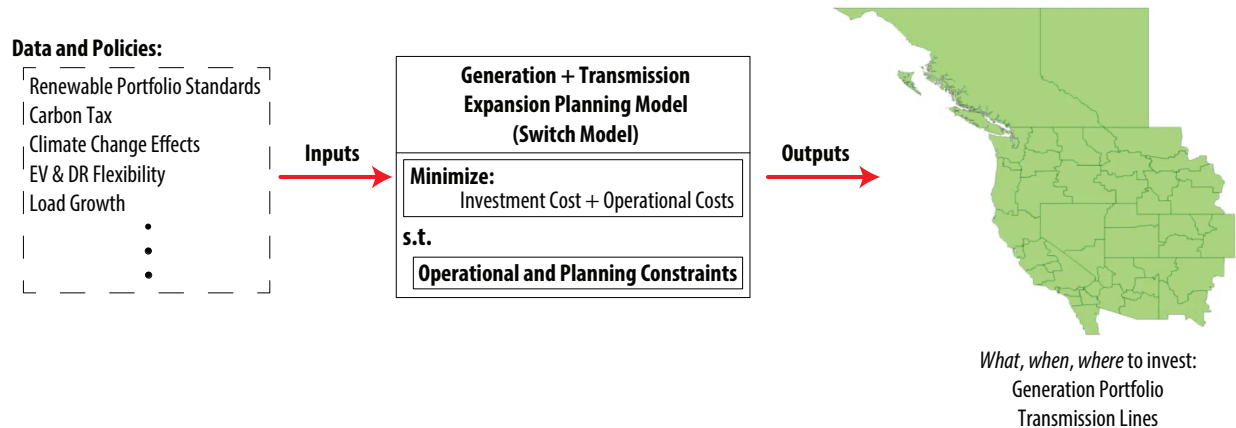
Figure 4.2: Summary of planning scenario for WECC and California by 2050.

- We review how the modularity of the Switch Power System Planning Model can be used to evaluate fundamental model challenges and trade-offs of expansion planning tools in considering the relevant aspects of a study case by modifying which modules are available.

- We implement two new DR and EV modules in the Switch model to evaluate and assess the value of flexibility of these resources in expansion planning models.

- We present a thorough analysis of the value DR and EV flexibility in a future WECC and California 2050 scenario by using the previous implemented modules in the Switch model.

The chapter is organized as follows: Section 4.1 provides a brief summary of the Switch Power System Planning Model. Then, Section 4.2 describe the mathematical and code implementation of both DR and EV modules implemented in the Switch model. Section 4.3, summarizes the model and data used for the 2050 WECC and California study while presenting the results of the optimization model. Finally, Section 4.4 concludes the chapter.

4.1   The Switch Power System Planning Model

Switch 1.0 was a planning model for power systems that implemented a condensed form of production cost modeling into a expansion planning problem. It was originally developed by Professor Matthias Fripp as part of his work at the University of California, Berkeley. Switch 1.0 was written in AMPL and was used in multiple studies in different systems [33, 97, 72]. With further development by Prof. Matthias Fripp, Dr. Josiah Johnston, Dr. James Nelson, Dr. Ana Mileva, Dr. Patricia Hidalgo-Gonzalez, Benjamin Maluenda and Rodrigo Henriquez-Auba, the Switch tool transitioned into a fully open source tool, Switch 2.0 [56].
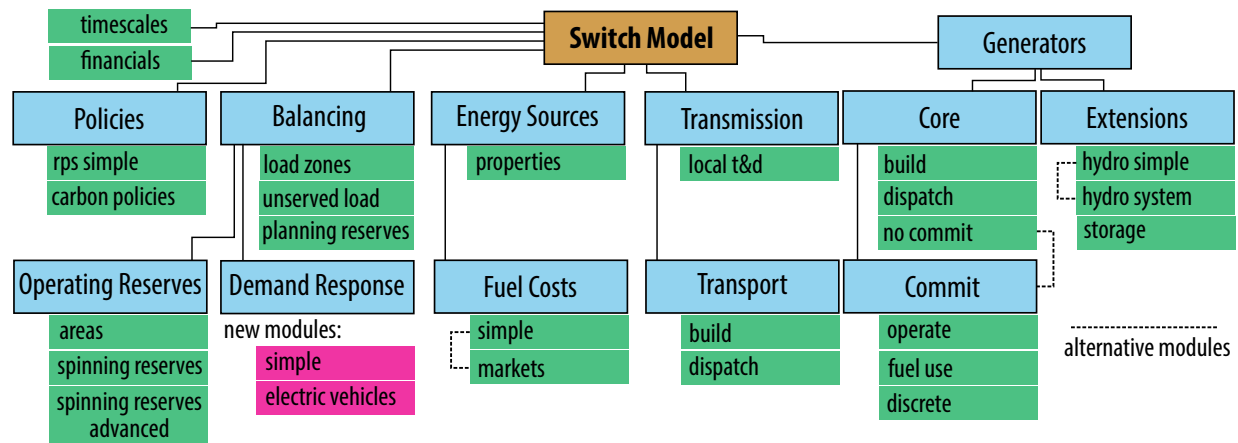
Figure 4.3: List of modules available in Switch. Figure adapted from [56].

Switch 2.0 is a Python package that is used to create and solve power system expansion planning models. Switch uses a modular framework that allows users to include specific components through a list of modules, allowing the possibility of choosing the appropriate level of detail depending on the complexity of the study. It uses the open-source Python Optimization Modeling Objects (Pyomo) package to define the mathematical models, read data and construct the optimization problem to solve it using commercial or open-source solvers. The list of modules available in Switch is depicted in Figure 4.3. The demand response modules associated with this dissertation that were implemented are highlighted in magenta color.

The detailed mathematical formulation of the Switch model is available in the supplementary information of [56], and its code implementation is available in the Github repository [122]. In the following subsection a brief summary of the Switch model is presented to highlight the fundamental aspects of operation and implementation details.

Brief mathematical and software implementation of Switch

Multiple timescales (from hours to decades) need to be mathematically represented in expansion planning models that includes high shares of RESs. In operational timescales, the model must have the possibility of reflecting annual, seasonal, daily and hourly variability of load and generation profiles, like wind, hydro and solar. For that purpose, Switch uses a three-level hierarchy of timescales to account for temporal aspects in multiple scales. These sets are:

- Periods $\mathcal{P}$: Set of multi-year timescales that describes when investment decisions are made. The duration of a period is typically on the order of one or more years, so cost associated with periods are specified in annualized costs. New infrastructure is added at the start of each period and is available to use throughout the period.

- Timeseries $\mathcal{S}$: Set that includes the blocks of consecutive time points within a period. Each individual time series can represent a single day, a week, a month or even an entire year. Each period p will have a subset of time series $\mathcal{S}_p$ that fall in that period p. This could be a single time series that capture the entire period, or a collection of representative days that represent seasonal effects in such period.

  Time series edge effects are addressed by treating them cyclically, such that the ending condition of the last time point of the series describe representative starting conditions of the first time point in the series.

- Timepoints $\mathcal{T}$: Set that describes unique time steps within a time series. Timepoints are the ones used to index operational variables, such as electricity demand and generation. The duration of a time point is typically on the order of one or more hours, so cost associated with time points, such as fuel cost usage, are specified in hourly units, e.g. \$/MWh.

With that, the fundamental problem in a expansion planning model is determining the investment decisions at each period, typically in transmission and generation, such that operational constraints in future timepoints can be satisfied at a minimum cost. The fundamental operational constraint is the power balance at each load zone $z \in \mathcal{Z}$, at each timepoint $t \in \mathcal{T}$:

$$\sum_{p^i \in \mathcal{P}^{\text{inject}}} p_{z,t}^i \quad = \sum_{p^w \in \mathcal{P}^{\text{withdraw}}} p_{z,t}^w, \qquad\qquad \forall z \in \mathcal{Z}, \forall t \in \mathcal{T} \qquad (4.1)$$

Here, the sets $\mathcal{P}^{\text{inject}}$ and $\mathcal{P}^{\text{withdraw}}$ are defined as:

- Components that inject power $\mathcal{P}^{\text{inject}}$: It is a set (defined as a Python list) of components p^i that contribute to a load zone balancing equation by injecting power. Each component in this list needs to be indexed by load zones z and time points t, and must have units in MW.

- Components that withdraw power $\mathcal{P}^{\text{withdraw}}$: It is a set (defined as a Python list) of components p^w that contribute to a load zone balancing equation by withdrawing power. Each component in this list needs to be indexed by load zones z and time points t, and must have units in MW.

Commonly, the list of injections $\mathcal{P}^{\text{inject}}$ includes power output $P_{g,t}$ for every generation project g located in load zone z, and inwards transmission flows into that load zone, $F_{\ell_z^{\text{in}},t}$, while the list of withdrawals $\mathcal{P}^{\text{withdraw}}$ typically includes customer loads $l_{z,t}$ and outwards transmission flows $F_{\ell_z^{\text{out}},t}$. However, the exact equation will depend on which modules are included, and electric vehicles and demand response modules will add additional variables into these lists.

For the objective function, the modular structure of Switch makes it impossible to know all of the cost components at the time the code is written, because different modules will

define different costs. To support a dynamic objective function that can be defined at runtime, two dynamic lists are created:

- Fixed cost components $\mathcal{C}^{\text{fixed}}$ is a set (defined as a Python list) of model components that contribute to overall system costs in each period. Each component c^{f} in this set is a Pyomo object that is indexed by period p and specified in units of annualized costs: non-discounted real dollars per year. Allowed Pyomo model components include parameters, decision variables, and expressions. Pyomo expressions are short calculations that are mathematically equivalent to fully constrained decision variables, except that expressions can be specified with fewer lines of code, appear to consume fewer computational resources and are completely factored out before sending the problem to the solver.

- Variable cost components $\mathcal{C}^{\text{var}}$ is a set (defined as a Python list) of model components that contribute to overall system costs on a timepoint basis. Each component c^{v} in this list is a Pyomo object that is indexed by timepoint t and specified in units of non-discounted real dollars per hour.

Thus, the objective function of the model can be written in an abstract form as:

$$\min \ \sum_{p \in \mathcal{P}} d_p \left\{ \sum_{c^{\text{f}} \in \mathcal{C}^{\text{fixed}}} c_p^{\text{f}} + \sum_{t \in \mathcal{T}_p} w_t^{\text{year}} \sum_{c^{\text{v}} \in \mathcal{C}^{\text{var}}} c_t^{v} \right\} \tag{4.2}$$

The objective function (4.2) minimizes the net present value of all investment and operation costs. The discount factor d_p includes two components, one to convert annual payments during each period to an equivalent lump sum at the beginning of a period, and another to convert that lump sum to a net present value:

$$d_p = \frac{1 - (1 + r)^{-\text{y}_p}}{r} \cdot (1 + r)^{-(\text{st}_p - \text{baseyear})}$$

Each fixed cost component c^{f} is a Pyomo object, indexed by period and specified in units of \$/year. This object may be a variable, parameter or expression (a calculation based on other components). The term c_p^{f} is the element with index p from component c^{f}. In the same way, variable cost components c^{v} are indexed by timepoint and specified in units of \$/hour.

Depending on which modules are being used for a case study, different components will be added to each set. For example, the *storage* module defines new investment variables for the energy portion of storage rated in MWh of energy capacity with an associated unit cost. In the code, it defines an expression *StorageEnergyInstallCosts*$_p$ to summarize the annualized capital costs, and adds this expression to the list of fixed costs $\mathcal{C}^{\text{fixed}}$. In this formulation, storage has no variable cost, so the module does not add any components to $\mathcal{C}^{\text{var}}$. Switch's modular architecture allows users to select modules relevant to their study

and keep other complexities out of the model and objective function. This can enable either faster execution, greater complexity, or greater time/spatial resolution elsewhere in the model. For example, in a single-bus study, investment and operational costs of transmission lines will not be included, and flow constraints will not even be defined. Removing those components can make the inclusion of discrete unit commitment or a larger time sample more practical.

One of the most important variable cost modules is the `generator.core.dispatch` module that defines the dispatch of the generation units at all time points. Here, the sum of all projects' dispatch at each timepoint t in each load zone z is added to the dynamic list $\mathcal{P}^{\text{inject}}$ in order to be included in the power balance equation (4.1). Variable O&M costs $c_g^{\text{om}} P_{g,t}$ are added to the list $\mathcal{C}^{\text{var}}$ to be included in the objective function (4.2).

The cost of operating fuel-powered generators also depends on the generators' heat rates (which may vary depending on operating level) and fuel prices (which may vary by period or have their own market structure). The fuel use rates $R_{g,t,f}$ are constrained to match the power output $P_{g,t}$ for each generator during each timepoint by the `generators.core.no_commit` or `generators.core.commit.fuel_use` module.

Detailed information of all modules available in Switch are available in the Supplementary Information in [56].

4.2 Mathematical Implementation of DR and EV Modules

For the purpose of studying the value of demand response and electric vehicle charging flexibility in 2050 energy scenarios for WECC and California, two modules were implemented in Switch, namely the `Demand Response - Simple` module and `Demand Response - Electric Vehicle` module. Both of these modules add new elements to the list of withdrawals $\mathcal{P}^{\text{withdraw}}$.

Demand Response – Simple module

This optional module describes a simple DR load-shifting service. Load in each load zone may be shifted between time points belonging to the same timeseries at no cost. This allows assessing the potential value of demand shifting. The constraints are:

$$-l_{z,t}^{\text{max,down}} \leq L_{z,t}^{\text{dr}} \leq l_{z,t}^{\text{max,up}}, \qquad \forall z \in \mathcal{Z}, \forall t \in \mathcal{T} \qquad (4.3)$$

$$\sum_{t \in \mathcal{T}_s} L_{z,t}^{\text{dr}} = 0, \qquad \forall z \in \mathcal{Z}, \forall s \in \mathcal{S} \qquad (4.4)$$

Equation (4.3) and parameters $l_{z,t}^{\text{max,down}}$ and $l_{z,t}^{\text{max,up}}$ represents the limits of how much power can be shifted at each load zone z at time point t. Typically, a percentage of the total load is used to define the limits. Equation (4.4) ensures that all the changes in demand balance out over the course of each time series (i.e. only shifting and no curtailment).

Code 4.1 DR module implementation in Python/Pyomo.

```python
def define_components(mod):

    mod.dr_shift_down_limit = Param(
        mod.LOAD_ZONES, mod.TIMEPOINTS,
        default= 0.0,
        within=NonNegativeReals,
        validate=lambda m, value, z, t: value <= m.zone_demand_mw[z, t])
    mod.dr_shift_up_limit = Param(
        mod.LOAD_ZONES, mod.TIMEPOINTS,
        default= float('inf'),
        within=NonNegativeReals)
    mod.ShiftDemand = Var(
        mod.LOAD_ZONES, mod.TIMEPOINTS,
        within=Reals,
        bounds=lambda m, z, t:
        (
            (-1.0) * m.dr_shift_down_limit[z,t],
            m.dr_shift_up_limit[z,t]
        ))

    mod.DR_Shift_Net_Zero = Constraint(
        mod.LOAD_ZONES, mod.TIMESERIES,
        rule=lambda m, z, ts:
        sum(m.ShiftDemand[z, t] for t in m.TPS_IN_TS[ts]) == 0.0)

    try:
        mod.Distributed_Power_Withdrawals.append('ShiftDemand')
    except AttributeError:
        mod.Zone_Power_Withdrawals.append('ShiftDemand')
```

The demand shift variable $L^{\text{dr}}_{z,t}$ is added to the set $\mathcal{P}^{\text{withdraw}}$ in order to be included in the balance equation (4.1). The core equations for the DR module implemented in Pyomo are presented in Code 4.1.

Demand Response – Electric Vehicle module

This optional module describes a DR flexible charging scheme for PEVs. A total amount of energy at each load zone must be delivered by the end of the time series, while satisfying specified energy bounds for each time point. These bounds represent an aggregated PEV availability for charging at specified hours. Figure 4.4 depicts an example of an PEV profile for charging availability. The region inside the min and max bounds is when it is only allowed to charge the PEV.
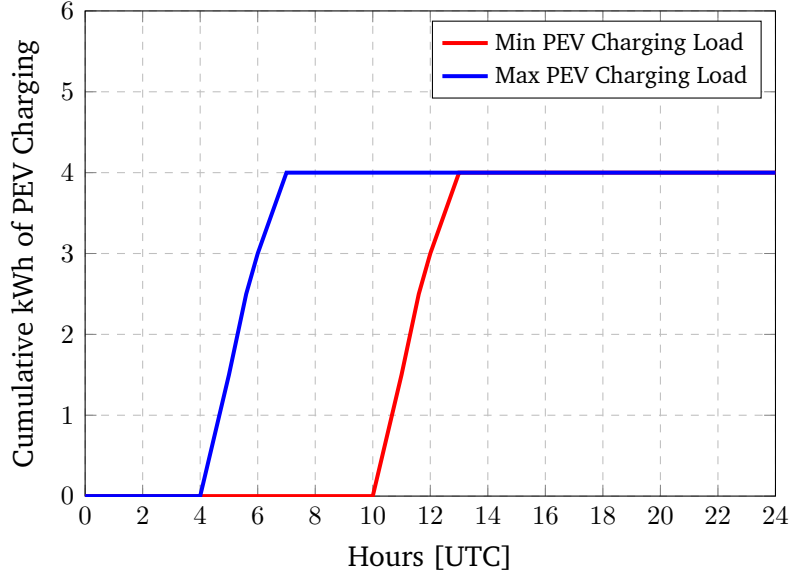
Figure 4.4: Example of PEV charging flexibility.

The mathematical formulation is as follows:

$$E_{z,t}^{\text{ev,min}} \leq E_{z,t}^{\text{ev}} \leq E_{z,t}^{\text{ev,max}}, \qquad\qquad \forall z \in \mathcal{Z}, \forall t \in \mathcal{T}_s, \forall s \in \mathcal{S} \qquad (4.5)$$

$$0 \leq P_{z,t}^{\text{ev}} \leq P_{z,t}^{\text{ev,lim}}, \qquad\qquad \forall z \in \mathcal{Z}, \forall t \in \mathcal{T}_s, \forall s \in \mathcal{S} \qquad (4.6)$$

$$E_{z,t}^{\text{ev}} = \sum_{\substack{k \in \mathcal{T}_s \\ k \leq t}} P_{z,k}^{\text{ev}} \Delta T, \qquad\qquad \forall z \in \mathcal{Z}, \forall t \in \mathcal{T}_s, \forall s \in \mathcal{S} \qquad (4.7)$$

Equation (4.5) ensures that the variable of cumulative charging energy $E_{z,t}^{\text{ev}}$ is between the specified bounds for each load zone z, time point t for every time series s. It is expected that the bounds match at the last time point of a time series, i.e., $E_{z,t_{\text{end}}}^{\text{ev,min}} = E_{z,t_{\text{end}}}^{\text{ev,max}}$, ensuring the delivery of the total charge energy. Equation (4.6) ensures that the variable that decides how much power is charged $P_{z,t}^{\text{ev}}$ is non-negative (i.e. does not allow discharge) and is limited by a maximum charge rate $P_{z,t}^{\text{ev,lim}}$. Finally, equation (4.7) adds up the charged energy at time points $k \leq t$ into the cumulative energy $E_{z,t}^{\text{ev}}$. The parameter ΔT, that defines how many hours are in each time point, is used to transform power into energy.

The power charge variable $P_{z,t}^{\text{ev}}$ is added to the set $\mathcal{P}^{\text{withdraw}}$ in order to be included in the balance equation (4.1). The core equations for the EV module implemented in Pyomo are presented in Code 4.2.

Code 4.2 EV module implementation in Python/Pyomo.

```python
def define_components(mod):
    mod.ev_charge_limit_mw = Param(
        mod.LOAD_ZONES, mod.TIMEPOINTS,
        default = float('inf'),
        within=NonNegativeReals)
    mod.ev_cumulative_charge_upper_mwh = Param(
        mod.LOAD_ZONES, mod.TIMEPOINTS,
        default = 0.0,
        within=NonNegativeReals)
    mod.ev_cumulative_charge_lower_mwh = Param(
        mod.LOAD_ZONES, mod.TIMEPOINTS,
        default = 0.0,
        within=NonNegativeReals)

    mod.EVCharge = Var(
        mod.LOAD_ZONES, mod.TIMEPOINTS,
        within=NonNegativeReals,
        bounds=lambda m, z, t:
        (0.0, m.ev_charge_limit_mw[z,t]))
    mod.EVCumulativeCharge = Expression(
        mod.LOAD_ZONES, mod.TIMEPOINTS,
        rule=lambda m, z, t: \
            sum(m.EVCharge[z,tau]*m.tp_duration_hrs[tau]
                for tau in m.TPS_IN_TS[m.tp_ts[t]]
                if tau <= t)
        )

    mod.EV_Cumulative_Charge_Upper_Limit = Constraint(
        mod.LOAD_ZONES, mod.TIMEPOINTS,
        rule=lambda m, z, t:
        m.EVCumulativeCharge[z,t] <= m.ev_cumulative_charge_upper_mwh[z,t])
    mod.EV_Cumulative_Charge_Lower_Limit = Constraint(
        mod.LOAD_ZONES, mod.TIMEPOINTS,
        rule=lambda m, z, t:
        m.EVCumulativeCharge[z,t] >= m.ev_cumulative_charge_lower_mwh[z,t])

    if 'Distributed_Power_Injections' in dir(mod):
        mod.Distributed_Power_Withdrawals.append('EVCharge')
    else:
        mod.Zone_Power_Withdrawals.append('EVCharge')

```

4.3   Scenarios in Long-term Power System Planning in Western North America

The work in this section is part of the work presented to the California Energy Commission via the technical report "Building a Healthier and More Robust Future: 2050 Low Carbon Energy Scenarios for California" by the primary authors Max Wei, Shuba Raghavan and Patricia Hidalgo-Gonzalez [137]. I, as a contributing author, lead the implementation of the effects demand response and electric vehicle flexibility in future energy scenarios.

System Model Description

In the aforementioned study [137], Switch is utilized to study the future power system of California and WECC under multiple scenarios of load growth, climate change effects and different policies from 2016 to 2055. In this section, we present a brief description of the Switch WECC model used in the studies, but for more details the reader is referred to the report [137].

Time-horizon Description

The Switch WECC model uses an optimization horizon divided in four investment periods $\mathcal{P}$ of 10 years length: 2016-2025 ("2020"), 2026-2035 ("2030"), 2036-2045 ("2040") and 2046-2055 ("2050"). Each period has a representative year with 24 time series. Each time series represent a sample of a day for every month of the representative year. We choose two days per month, median and peak load day ($2 \times 12 = 24$ time series $\mathcal{S}$), and each time series is represented by 6 time points of 4 hours duration. Thus, in total each period simulates 144 time points $\mathcal{T}$ of dispatch (12 months $\times$ 2 days/month $\times$ 6 time points/day = 144 time points).

   To consider the differences on occurrence of median and peak days, the weight on the objective function of peak days are set to one, while median days are set to $n - 1$, where n is the number of days of that month. Finally, the representative year is weighted by ten to represent the cost of the entire length of each period (10 years).

Spatial Description

Geographically, Switch WECC divides the region in 50 load zones $\mathcal{Z}$. The transmission system was obtained from Ventyx geolocated transmission line data via its EV Energy Map [24], while thermal limits are obtained from the Federal Energy Regulatory Commission (FERC). In total, there are 105 existing transmission lines connecting load zones. Switch will optimally decide to build more lines if required, using a continuous variable for installed capacity. A transport model is used to decide how much power will flow through the lines. In addition, de-rating and transmission losses are also considered in the transport model. Figure 4.5 depicts the spatial representation of the Switch WECC model. Non-existing lines
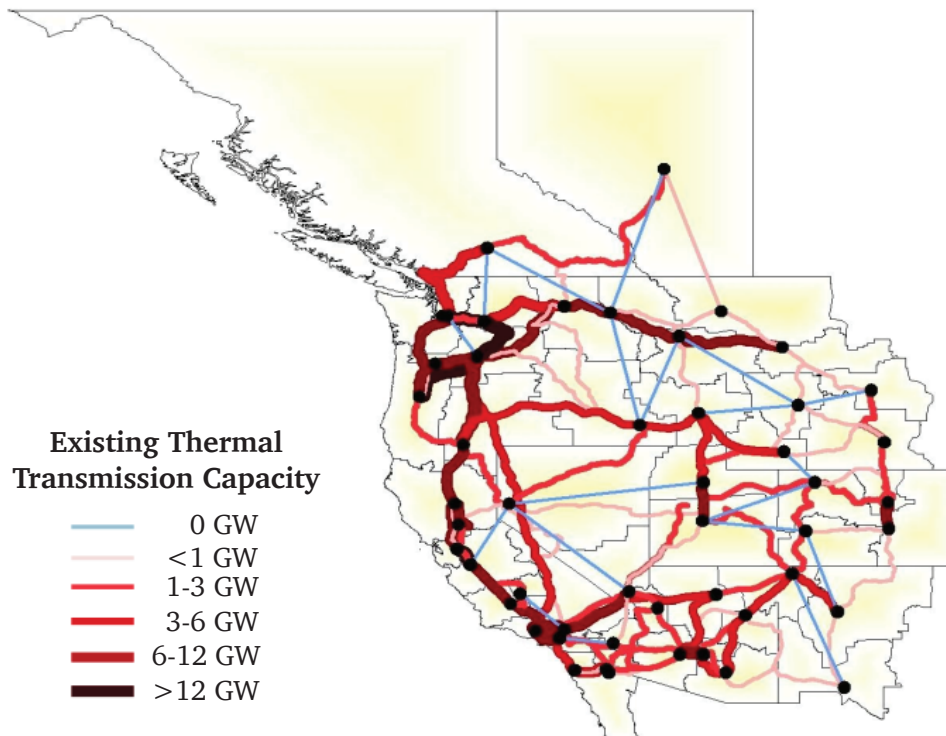
Figure 4.5: Spatial and transmission lines representation of Switch WECC [137].

that can be installed in the optimization problem are depicted in light blue, while black
dots represent the largest substation in the load zone.

Additional parameters

Electricity demand profiles were obtained from historical hourly loads profiles from 2006
[20, 23]. These profiles are scaled to future projections based on multiple scenarios (see
[137] for more details on scenarios). Existing wind power output is derived from the 3TIER
Western Wind and Solar Integration Study wind speed dataset using idealized turbine
power output curves [64, 66]. For solar energy, hourly capacity factors of each project in
2006 were simulated using the System Advisor Model (SAM) from National Renewable
Energy Laboratory (NREL) [65].

A WECC carbon cap was included to achieve 80% emissions from 1990 levels by the
2050 period. A California carbon cap was also modeled to attain 40% emissions by the 2030
period. Fuel prices projection were obtained from the U.S. Environmental Information
Agency (EIA) [2]. Capital costs and operation and maintenance costs were obtained from
[132, 31]. The pool of WECC plants were obtained from the U.S. EIA via EIA-860 and
EIA-923 2016 data. Finally, the hydropower historical generation was also obtained from
EIA-923 2016 data.
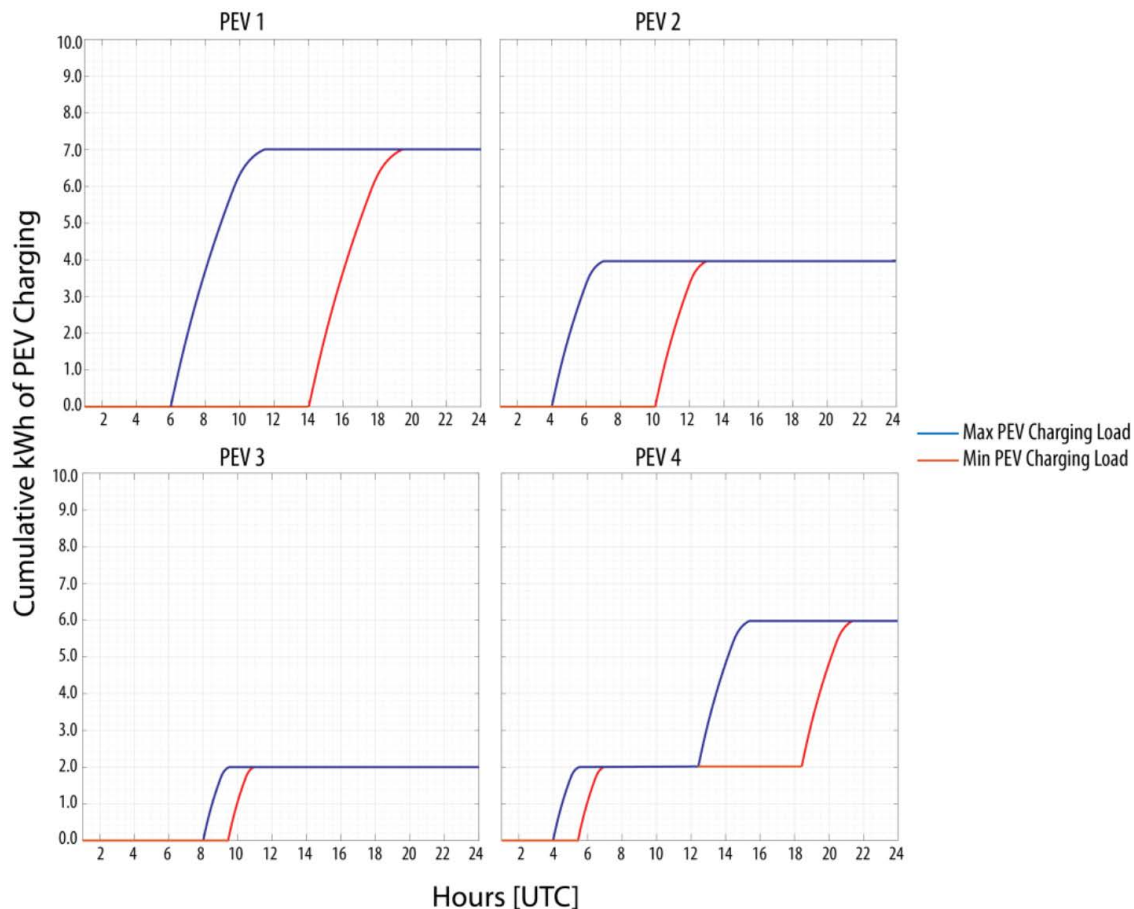
Figure 4.6: Example constraints on charging profiles for different PEVs.

Electric Vehicles and Demand Response Data Description

One of the scenarios that we explored for the 2050 study was `Aggressive Efficiency with Electrification` [137], that considers higher rate of energy efficiency retrofits with a high rate of building electrification and aggressive adoption of electrical vehicles in transportation. In particular, we were looking to explore the effects in investment portfolios when flexible charging of LDVs is available to be controlled by the system operator at no cost.

As described in section 4.2, the trajectory of charging must be between two bounds. Such bounds were obtained by the Behavior, Energy, Autonomy, and Mobility (BEAM) model, based on simulations on the mobility and charging behavior for representative days of the week and types of chargers [118]. Figure 4.6 presents examples of random PEVs with specified bounds depending on their charging profiles.

Based on the charging bounds provided by the BEAM model, an aggregated profile is constructed by weighting and adding all the available bounds. The result is then normalized
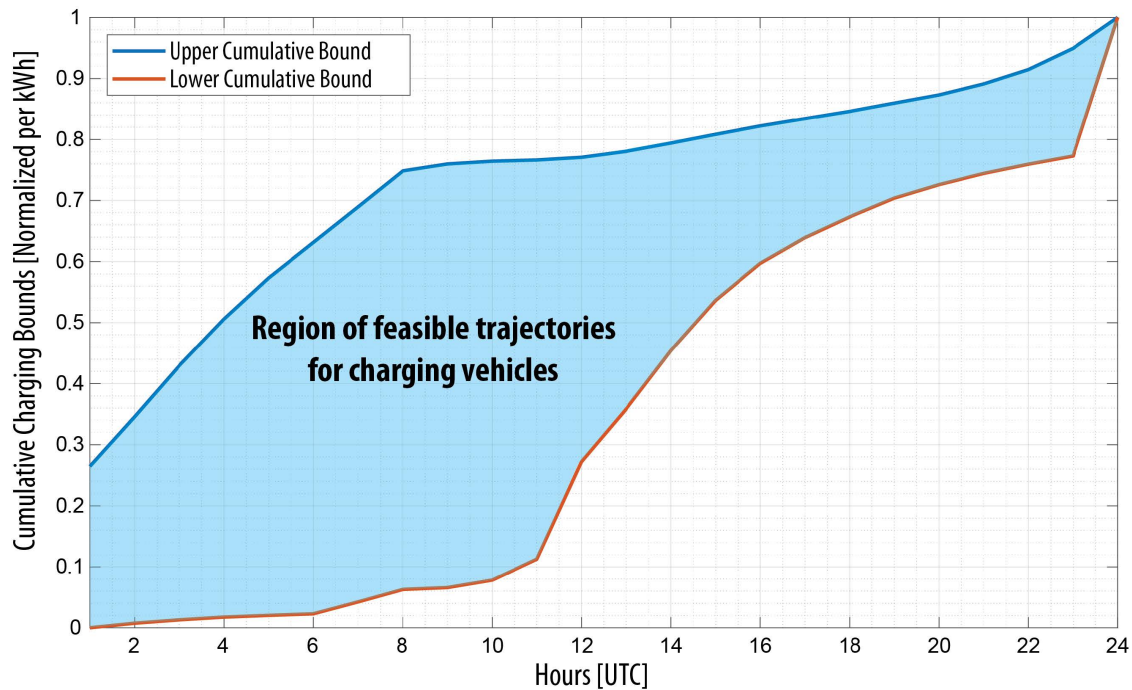
Figure 4.7: Normalized bounds for PEV charging in Switch WECC studies [137].

to then be scaled depending on the energy requirements at specified periods. Figure 4.7
presents the normalized aggregated profile used in the Switch WECC studies.

Table 4.1 provides the estimation of energy requirements for PEVs through the Switch
WECC periods. These are based on growth projection of PEVs and average expected
use, in particular using expected miles traveled per year and efficiency of the batteries
in kWh/miles. The data are presented for California (CA), Rocky Mountains, Arizona
and New Mexico (RM-AZNM), WECC-Canada (WECC-CAN) and Northwest Power Pool
(NWPP). The energy requirements is divided (weighted on population) if multiple load
zones are present in Switch WECC for each of the previous 4 zones. These requirements
will be enforced through scaling the normalized charging profile (Figure 4.7), depending
on each load zone and period. Finally, in the study case when the Switch DR-EV module
is not considered, the LDVs' energy requirements are added as regular load, uniformly for
each time point.

In addition, a simple load-shifting service of DR at no cost (as presented in section 4.2)
is included in the scenario with EV flexibility. This represents DR capability for homes and
businesses. The amount of energy available for load-shifting, with respect to the total load,
is presented in Table 4.2.

Table 4.1: Expected LDVs stock and energy required per zone and period [137].

Zone	LDVs stock [million]				Energy Required [GWh]			
	2020	2030	2040	2050	2020	2030	2040	2050
CA	0.85	6.59	19.98	31.67	2637	16363	46857	91494
RM-AZNM	0.007	0.41	3.09	9.77	200	1600	8292	24108
WECC-CAN	0.044	0.72	3.28	7.21	600	4223	12738	26123
NWPP	0.09	1.40	6.25	13.48	1200	8192	24215	48808

Table 4.2: Fraction of shiftable demand by period and zone.

Average Moveable % of Hourly Total Demand	Period			
	2020	2030	2040	2050
Total % California Zones [w.r.t. total load]	0.3%	2%	7%	10%
Total % non-California Zones [w.r.t. total load]	0%	0.3%	2%	7%

Results

To compare the impact of considering flexibility of EV and DR resources, two scenarios are compared, namely the `Aggressive Efficiency with Electrification` scenario, with and without resource flexibility.

   Switch WECC is run for these two scenarios and their optimal results are compared. Figure 4.8 summarizes the fraction of generation for all periods optimized for both WECC (all load zones) and California load zones.

   Results showcase how the increase in flexibility allows a higher usage of solar and wind resources. This is achieved by the opportunity to shift load to hours when higher RESs are available to be dispatched, reducing the curtailment of such resources. This is particularly effective in California at 2050, when there is the largest availability of flexible EV and DR resources. Solar energy usage is increased by 12 percent in that period, due to shifting of load into sunny hours, increasing the efficiency usage of the solar resource.

   A significant reduction of installed capacity is also observed due to the EV and DR flexibility. Figure 4.9 summarizes that result, on which is observed that more than 100 GW of capacity is reduced, while increasing the proportion for solar capacity in the system.

   As previously mentioned, this additional flexibility results in a more efficient usage of all available resources, mostly renewable ones, reducing the requirements to install additional capacity, particularly to cover high power requirements in peak days. The EV and DR flexibility yields savings of 5.2% of the total investment and operational costs through all the periods from 2020 to 2050. However, it is important to note that these results assume that smart EV charging and DR are free to dispatch and procure, and such load shifting is achieved by a system operator or third-party service provider without assuming any cost.
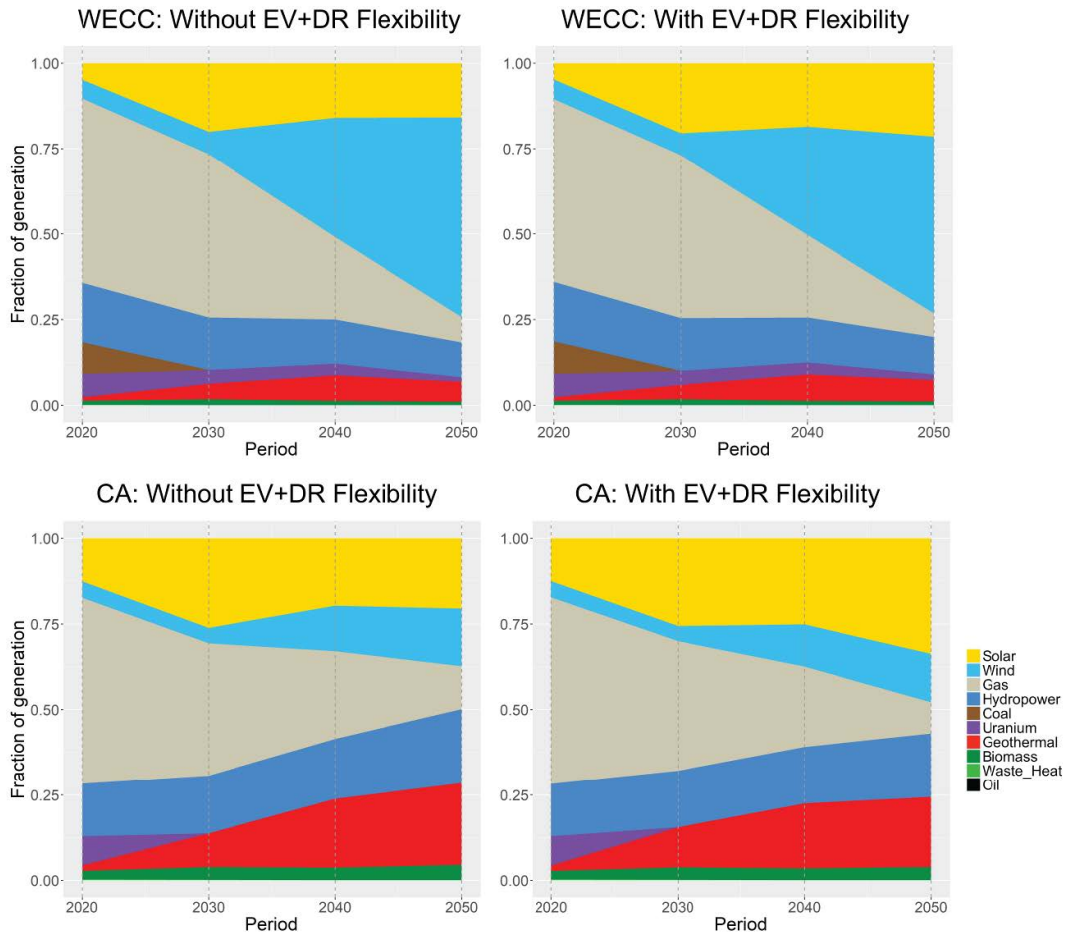
Figure 4.8: Fraction of generation in WECC and California with/without flexibility [137].
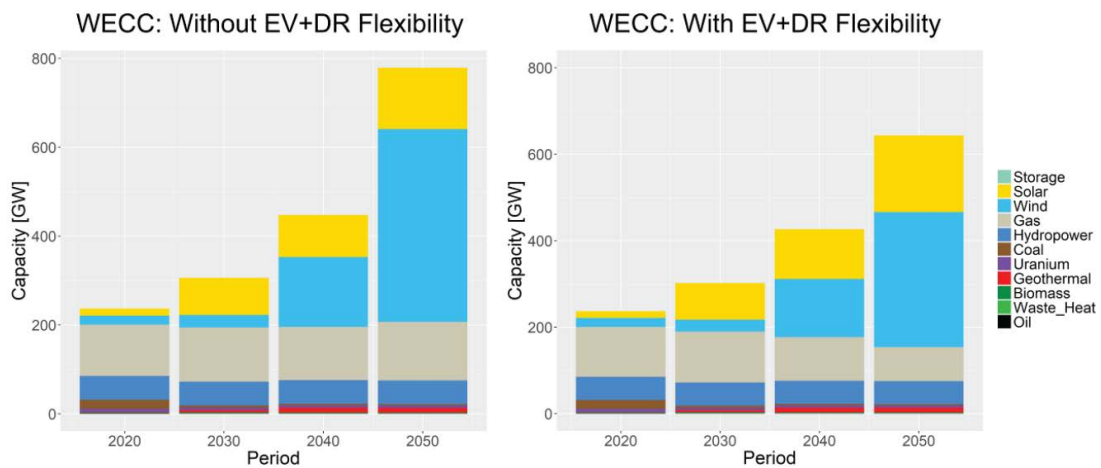

Figure 4.9: Installed capacity in WECC with/without EV and DR flexibility [137].

4.4 Conclusions

In this chapter we have presented the implementation, on the Switch model, of both EV and DR modules to capture the value of load flexibility in expansion planning models. The modular architecture of the Switch model reflects the modularity of actual power systems, where individual elements operate independently but contribute to the system's total costs and power balance. These modules interact with the overall optimization model by adding terms to the shared energy and reserve balances and the overall cost expression. This general flexibility allows users to enable case studies with different levels of model complexity to assess the effects of new technologies or a more detailed formulation.

Both DR and EV models were used in a large WECC and California study to understand 2050 low-carbon energy scenarios, and the effects of different policies on energy portfolio of the future. The Pyomo code implementation in the Switch model for both modules was presented and were used to study the value of such flexibility in thus future scenario.

Results showcase how leveraging demand flexibility can achieve significant savings in future energy systems, reducing the curtailment of renewable resources and reducing the requirements of overall required capacity to be installed in the system. Total savings over 5% were achieved due to the reduction of total infrastructure investment and less fuel usage. However, future work is still required to understand the limitations and real application of the untapped potential of vehicle charging flexibility, particularly in a future on where we expect further electrification of the transportation system. The work presented here only focused on LDV, but in a future when truck shipping become electric, we should expect even more savings, and maybe different energy portfolios, as long as we are able to capture the value of such charging flexibility.

Chapter 5

Conclusions and Future Directions

This thesis investigates how the inclusion of IBRs is challenging our understanding of power systems in multiple time and space scales. To do so, we use different optimization and control methods for studying how the future of our electric grid will operate and look like. This dissertation's most crucial result lies in showcasing that to move into a sustainable future requires addressing fundamental challenges in the operation and planning of power systems. For example, Chapter 2 highlights how more network and load modeling details will be crucial to obtain accurate stability regions in systems with large shares of renewable sources, while Chapter 4 depicts how demand flexibility have major effects on long-term planning of generation and transmission investments. As discussed throughout the dissertation, computational simulation and optimization must continue to evolve in a flexible manner to provide novel solutions to tackle these challenges. *Reproducibility* and *validity* is at the core of any scientific research, and the power system field should strive to improve these aspects as highlighted in this dissertation. Both tools presented in this dissertation, `PowerSimulationsDynamics.jl` and the Switch model, are examples on how scientific computing and open source software enable opportunities on performing new analyses and answering new research questions as we move towards decarbonized power systems.

The first part of the thesis focuses on modeling and time domain simulation of power systems with shares of IBRs. We review how grid-following and grid-forming control strategies can be used to enable a resilient and reliable future of low-inertia grids. In addition, we propose the Julia tool `PowerSimulationsDynamics.jl` to leverage Scientific Computing aspects and promote *replicability* in future power system analyses. Motivated by SPT approaches, we analyze how the effect of electromagnetic phenomena in voltage and line dynamics can significantly affect the stability regions of VSM resources by characterizing three different network models in numerical simulation and small signal stability analyses. Our results highlight how network electromagnetic transient phenomena must be considered to properly capture stability regions of GFM inverters. In addition, we extend this by focusing into how load modeling plays a major role in how stability of systems with IBR presence is affected. Our work identifies that traditional constant impedance load models,

do not capture system level phenomena and bifurcations that we need to address for a reliable operation. As mentioned, there is a necessity of capturing network EMT phenomena for GFM stability analyses, but our load analyses conclude that ideal CPLs are not suitable for EMT studies, and hence new CPL models, such as the 12-states active load model, are more relevant to properly study GFM inverter - CPL interactions.

The second part of the thesis studies how market structures and pricing schemes can significantly affect investment of distributed solar PV. In particular, we propose three different optimization models for studying the investment decisions and revenue of agents in these settings. These include a status-quo standalone net-metering case, a sharing model and a wholesale market approach. A game theoretical approach is used to study the sharing scheme, and theoretical guarantees are provided in competitive scenarios. Results showcase how peer-to-peer approaches promote PV investment, but high retail tariffs are fundamental for encouraging such investment. Indeed, wholesale market scenarios with lower prices cannot encourage PV at current costs. Demand charges can help on promoting PV in a wholesale market setup, but not enough given current PV costs.

Finally, the third part of the thesis provides a detailed discussion of long-term planning investment scenarios for California in 2050 under cases of large demand flexibility. To do so, the Switch model is introduced and two modules are used to capture demand flexibility, such as a simple DR model and an EV model are presented. Both of these modules allow shifting demand that can significantly reduce peak load, giving the possibility of deferring investment decisions. By enabling and disabling these modules, comparison of these effects can be assessed in investment decisions and operating costs.

The main conclusions and findings of this dissertation are summarized as follows:

- In a changing environment of new devices and controllers, our rooted assumptions of how we understand power systems are changing. For example, in this dissertation we noted that positive sequence tools that neglects network dynamics can overestimate stability regions on inverters. In addition, we showcased how using representative days are necessary to capture RESs variability, a requirement to decide optimal investment decisions in long-term planning studies. As we rely on computational tools to study power systems, *reproducibility* and *validity* must be encouraged in the community to ensure a common ground for future research. `PowerSimulationsDynamics.jl` and the Switch model, using version control in Github, showcase how open source tools help to achieve these goals.

- Future power systems will require detailed modeling of IBRs, their control schemes, network and load devices to properly capture the relevant timescales and stability regions of IBRs.

- Reduced-order model approaches based on SPT can be used in many scenarios to accelerate large-scale simulations. Theoretical approaches based on eigenvalues of linearized systems can be used to confirm the validity of such approximations.

- `PowerSimulationsDynamics.jl` is an open-source tool that can be used to numerically explore the effects of different approximations given its flexibility and modularity, while enabling scientific computing aspects for the power systems community. Indeed, all of the results presented using `PowerSimulationsDynamics.jl` in this dissertation are available in their own Github repository to ensure *reproducibility* of the results presented. We also made all of the models open source (as they are available `PowerSimulationsDynamics.jl`) and validated with other commercial and research tools, such as Siemens PSS®E or PSAT.

- Market structures and pricing schemes play a major role in how consumers invest in distributed solar PV in addition to the expected drivers such as electric consumption and solar irradiance. Indeed, results confirm that sharing economy approaches promote PV investment, but high retail tariffs are necessary for encouraging such investment.

- Demand flexibility, such as DR and EV flexibility, is a crucial aspect to consider when planning large-scale investments of power systems, since it can have major implications for generation and transmission investments.

- Future electrification scenarios for California showcase the importance of properly enabling flexibility at multiple levels, such as demand, generation and transmission, to deal with possible future climate change-driven uncertainties in a cost effective manner.

Regarding future work and moving forward in related topics addressed in this dissertation we highlight the following aspects that require additional research:

- All models for IBRs presented in Chapter 2 assume an ideal DC-side energy source that can provide enough power to address the changes occurring in the AC side. Additional modeling in energy technologies, such as wind, solar, battery storage, etc., and their DC-side controllers are necessary to capture the implications of power limits at the primary energy source side.

- In addition, the IBR models used in Chapter 2 do not consider physical limitations, such as maximum inverter currents, impose additional constraints on how much power an IBR can output in the presence of a fault. Exploring such control strategies, in particular for GFM converters, and the effects on stability, such as limit-induced bifurcations, is a relevant research direction.

- Considering a future grid with more IBRs than SMs with more current limits, protection coordination, that nowadays rely on high fault currents provided by SM, will be a significant relevant topic to be explored.

- Results for peer-to-peer schemes on 3 rely on perfect information and perfect competition to obtain the maximizing social welfare PV investment plan. Investigating

how imperfect information flow across agents affects PV investment decisions, which closely resembles what occurs in practice, is a relevant future direction to analyze.

- New policies such as the Inflation Reduction Act of 2022, and recent effects of climate change must be analyzed in long-term planning studies. With such changes we are likely to expect a different system for 2050 in California. Understanding the value of flexibility and mitigating strategies become more relevant to ensure a sustainable grid for a sustainable future.

Bibliography

[1] Jennifer C Adam, Alan F Hamlet, and Dennis P Lettenmaier. "Implications of global climate change for snowmelt hydrology in the twenty-first century". In: *Hydrological Processes: An International Journal* 23.7 (2009), pp. 962–972 (cit. on p. 1).

[2] U.S. Energy Information Administration. *Annual Energy Outlook 2017 with projections to 2050*. 2017. URL: http://large.stanford.edu/courses/2017/ph241/grace1/docs/0383-2017.pdf (visited on 08/20/2022) (cit. on p. 109).

[3] Paris Agreement. "Paris agreement". In: *Report of the Conference of the Parties to the United Nations Framework Convention on Climate Change (21st Session, 2015: Paris). Retrieved December*. Vol. 4. HeinOnline. 2015, p. 2017 (cit. on p. 1).

[4] Olaoluwapo Ajala et al. "Model reduction for inverters with current limiting and dispatchable virtual oscillator control". In: *IEEE Trans. on Energy Conversion* (2021) (cit. on pp. 61, 64).

[5] Eric H Allen and MD Ilic. "Interaction of transmission network and load phasor dynamics in electric power systems". In: *IEEE Trans. on Circuits and Systems I: Fundamental Theory and Applications* 47.11 (2000), pp. 1613–1620 (cit. on pp. 61, 69).

[6] Anmar Arif et al. "Load modeling—A review". In: *IEEE Transactions on Smart Grid* 9.6 (2017), pp. 5986–5999 (cit. on p. 60).

[7] Australian Energy Market Operator. *Application of Advanced Grid-scale Inverters in the NEM*. Tech. rep. Australian Energy Market Operator (AEMO), Australia, 2021 (cit. on pp. 17, 18, 19, 20).

[8] Galen L. Barbose. "Putting the Potential Rate Impacts of Distributed Solar into Context". In: *Lawrence Berkeley National Laboratory* (2017) (cit. on p. 73).

[9] Galen L. Barbose, Naïm R. Darghouth, Eric O'Shaughnessy, and Sydney Forrester. "Tracking the Sun: Pricing and Design Trends for Distributed Photovoltaic Systems in the United States (2021 Edition) [Slides]". In: *Lawrence Berkeley National Laboratory* (Sept. 2021) (cit. on p. 74).

[10]   Galen L. Barbose et al. "Tracking the sun: Installed price trends for distributed photovoltaic systems in the United States - 2018 edition". In: *Lawrence Berkeley National Laboratory* (2018) (cit. on p. 73).

[11]   Céline Bellard et al. "Impacts of climate change on the future of biodiversity". In: *Ecology letters* 15.4 (2012), pp. 365–377 (cit. on p. 1).

[12]   Jeff Bezanson, Alan Edelman, Stefan Karpinski, and Viral B Shah. "Julia: A fresh approach to numerical computing". In: *SIAM review* 59.1 (2017), pp. 65–98 (cit. on p. 29).

[13]   Janusz Bialek et al. *System Needs and Services for Systems with High IBR Penetration*. Tech. rep. Global Power System Transformation Consortium (GPST), CO, USA, 2021 (cit. on pp. 17, 20, 23).

[14]   Federico Bliman, Andres Ferragut, and Fernando Paganini. "Controlling aggregates of deferrable loads for power system regulation". In: *American Control Conference (ACC), 2015*. IEEE. 2015, pp. 2335–2340 (cit. on p. 75).

[15]   Severin Borenstein and James R. Bushnell. "Do Two Electricity Pricing Wrongs Make a Right? Cost Recovery, Externalities, and Efficiency". In: *Environmental Economics eJournal* (2018) (cit. on p. 94).

[16]   Martin Braun et al. "The Future of Power System Restoration: Using Distributed Energy Resources as a Force to Get Back Online". In: *IEEE Power and Energy Magazine* 16.6 (2018), pp. 30–41 (cit. on p. 21).

[17]   California Public Utilities Commission. *Virtual Net Metering*. URL: http://www.cpuc.ca.gov/General.aspx?id=5408 (cit. on p. 74).

[18]   Joe H Chow. *Time-scale modeling of dynamic networks with applications to power systems*. Springer, 1982 (cit. on pp. 27, 46, 47).

[19]   Joe H Chow, Petar V Kokotovic, and Robert J Thomas. *Systems and control theory for power systems*. Springer Science & Business Media, 1995 (cit. on p. 65).

[20]   Federal Energy Regulatory Comission. *Form 714: Annual Electric Balancing Authority Area and Planning Area Report*. 2006 (cit. on p. 109).

[21]   Charles Concordia and Susumu Ihara. "Load representation in power system stability studies". In: *IEEE Trans. on Power Apparatus and Systems* 4 (1982), pp. 969–977 (cit. on p. 59).

[22]   Jeffrey J. Cook, Kristen B. Ardani, Robert M. Margolis, and Ran Fu. *Cost-Reduction Roadmap for Residential Solar Photovoltaics (PV), 2017-2030*. Tech. rep. National Renewable Energy Lab.(NREL), Golden, CO (United States), 2018 (cit. on p. 73).

[23]   Platts Corporation. *POWERmap: Substation Layer*. 2009 (cit. on p. 109).

[24]   Ventyx Corporation. *Ventyx EV Energy Map*. 2009 (cit. on p. 108).

[25]   Hantao Cui, Fangxing Li, and Kevin Tomsovic. "Hybrid symbolic-numeric frame-work for power system modeling and analysis". In: *IEEE Transactions on Power Systems* 36.2 (2020), pp. 1373–1384 (cit. on p. 26).

[26]   Salvatore D'Arco, Jon Are Suul, and Olav B Fosso. "A Virtual Synchronous Machine implementation for distributed control of power converters in SmartGrids". In: *Electric Power Systems Research* 122 (2015), pp. 180–197 (cit. on pp. 43, 44, 54, 61, 63).

[27]   Guillaume Denis et al. "The Migrate project: the challenges of operating a transmission grid with only inverter-based generation. A grid-forming control improvement with transient current-limiting control". In: *IET Renewable Power Generation* 12.5 (2018), pp. 523–529 (cit. on p. 42).

[28]   Steven Diamond and Stephen Boyd. "CVXPY: A Python-embedded modeling language for convex optimization". In: *Journal of Machine Learning Research* 17.83 (2016), pp. 1–5 (cit. on p. 89).

[29]   Dong Dong et al. "Analysis of phase-locked loop low-frequency stability in three-phase grid-connected power converters considering impedance interactions". In: *IEEE Trans. on Industrial Electronics* 62.1 (2014), pp. 310–321 (cit. on p. 42).

[30]   Roger C Dugan and Thomas E McDermott. "An open source platform for collaborating on smart grid research". In: *2011 IEEE power and energy society general meeting*. IEEE. 2011, pp. 1–7 (cit. on p. 25).

[31]   Energy + Environmental Economics. *Decarbonizing Pipeline Gas to Meet California's 2050 Greenhouse Gas*. 2015. URL: https://www.ethree.com/wp-content/uploads/2017/02/E3_Decarbonizing_Pipeline_01-27-2015.pdf (visited on 08/20/2022) (cit. on p. 109).

[32]   Ali Emadi, Alireza Khaligh, Claudio H Rivetta, and Geoffrey A Williamson. "Constant power loads and negative impedance instability in automotive systems: definition, modeling, stability, and control of power electronic converters and motor drives". In: *IEEE Trans. on Vehicular Technology* 55.4 (2006), pp. 1112–1125 (cit. on p. 60).

[33]   Matthias Fripp. "Switch: a planning tool for power systems with large shares of intermittent renewable energy". In: *Environmental science & technology* 46.11 (2012), pp. 6371–6378 (cit. on p. 100).

[34]   Ran Fu et al. *US solar photovoltaic system cost benchmark: Q1 2017*. Tech. rep. NREL, Golden, CO (United States), 2017 (cit. on pp. 73, 89).

[35]   Leonardo Gacitua et al. "A comprehensive review on expansion planning: Models and tools for energy policy analysis". In: *Renewable and Sustainable Energy Reviews* 98 (2018), pp. 346–360 (cit. on pp. 4, 98, 99).

[36] Dominic Groß, Marcello Colombino, Jean-Sébastien Brouillon, and Florian Dörfler. "The effect of transmission-line dynamics on grid-forming dispatchable virtual oscillator control". In: *IEEE Transactions on Control of Network Systems* 6.3 (2019), pp. 1148–1160 (cit. on pp. 3, 42, 59).

[37] Gurobi Optimization, LLC. *Gurobi Optimizer Reference Manual*. 2022. URL: https://www.gurobi.com (cit. on p. 89).

[38] Mahmoud Pesaran HA, Phung Dang Huy, and Vigna K Ramachandaramurthy. "A review of the optimal allocation of distributed generation: Objectives, constraints, methods, and algorithms". In: *Renewable and Sustainable Energy Reviews* 75 (2017), pp. 293–312 (cit. on p. 75).

[39] He Hao and Wei Chen. "Characterizing flexibility of an aggregation of deferrable loads". In: *Decision and Control (CDC), 2014 IEEE 53rd Annual Conference on*. IEEE. 2014, pp. 4059–4064 (cit. on p. 75).

[40] Nikos Hatziargyriou et al. "Definition and classification of power system stability–revisited & extended". In: *IEEE Transactions on Power Systems* 36.4 (2020), pp. 3271–3281 (cit. on pp. 3, 4, 7, 19).

[41] Reza Hemmati, Rahmat-Allah Hooshmand, and Amin Khodabakhshian. "Comprehensive review of generation and transmission expansion planning". In: *IET Generation, Transmission & Distribution* 7.9 (2013), pp. 955–964 (cit. on p. 4).

[42] Rodrigo Henriquez-Auba, Jose D Lara, Ciaran Roberts, and Duncan S Callaway. "Grid forming inverter small signal stability: Examining role of line and voltage dynamics". In: *IECON 2020 The 46th Annual Conference of the IEEE Industrial Electronics Society*. IEEE. 2020, pp. 4063–4068 (cit. on pp. 42, 59).

[43] Rodrigo Henriquez-Auba, Jose Daniel Lara, Duncan S Callaway, and Clayton Barrows. "Transient simulations with a large penetration of converter-interfaced generation: scientific computing challenges and opportunities". In: *IEEE Electrification Magazine* 9.2 (2021), pp. 72–82 (cit. on pp. 3, 24, 25, 26, 31).

[44] Rodrigo Henriquez-Auba et al. "LITS. jl–An Open-Source Julia based Simulation Toolbox for Low-Inertia Power Systems". In: *arXiv preprint arXiv:2003.02957* (2020) (cit. on p. 32).

[45] Rodrigo Henriquez-Auba et al. "Sharing economy and optimal investment decisions for distributed solar generation". In: *Applied Energy* 294 (2021), p. 117029 (cit. on p. 74).

[46] Rodrigo Henriquez-Auba et al. "The Sharing Economy for Residential Solar Generation". In: *Decision and Control (CDC), 2018 IEEE 57nd Annual Conference on*. IEEE. 2018, pp. 7322–7329 (cit. on p. 74).

[47] High Share of Inverter-Based Generation Task Force. *Grid-Forming Technology in Energy Systems Integration*. Tech. rep. Energy Systems Integration Group (ESIG), Reston, VA, USA, 2021 (cit. on pp. 17, 23).

[48] Alan C Hindmarsh et al. "SUNDIALS: Suite of nonlinear and differential/algebraic equation solvers". In: *ACM Transactions on Mathematical Software (TOMS)* 31.3 (2005), pp. 363–396. DOI: 10.1145/1089014.1089020 (cit. on p. 36).

[49] Ove Hoegh-Guldberg et al. "Coral reefs under rapid climate change and ocean acidification". In: *science* 318.5857 (2007), pp. 1737–1742 (cit. on p. 1).

[50] "IEEE Guide for Synchronous Generator Modeling Practices and Parameter Verification with Applications in Power System Stability Analyses". In: *IEEE Std 1110-2019 (Revision of IEEE Std 1110-2002)* (2020), pp. 1–92 (cit. on p. 7).

[51] "IEEE Recommended Practice for Excitation System Models for Power System Stability Studies". In: *IEEE Std 421.5-2016 (Revision of IEEE Std 421.5-2005)* (2016), pp. 1–207 (cit. on p. 7).

[52] Institute for Local Self Reliance. *Virtual Net Metering*. Nov. 2016. URL: https://ilsr.org/virtual-net-metering/ (cit. on p. 74).

[53] IRENA. *Renewable Energy Statistics 2018*. Tech. rep. The International Renewable Energy Agency, Abu Dhabi, 2018 (cit. on p. 73).

[54] Himanshu Jain et al. "Blackstart of Power Grids with Inverter-Based Resources". In: *Proc. IEEE Power & Energy Society General Meeting (PESGM)*. 2020, pp. 1–5 (cit. on p. 21).

[55] Brian B Johnson et al. "A Generic Primary-control Model for Grid-forming Inverters: Towards Interoperable Operation & Control." In: *HICSS*. 2022, pp. 1–10 (cit. on pp. 61, 66).

[56] Josiah Johnston, Rodrigo Henriquez-Auba, Benjamin Maluenda, and Matthias Fripp. "Switch 2.0: A modern platform for planning high-renewable power systems". In: *SoftwareX* 10 (2019), p. 100251 (cit. on pp. 100, 101, 104).

[57] Andrew Keane and Mark O'Malley. "Optimal allocation of embedded generation on distribution networks". In: *IEEE Transactions on Power Systems* 20.3 (2005), pp. 1640–1646 (cit. on p. 75).

[58] Walid El-Khattam, Kankar Bhattacharya, Yasser Hegazy, and MMA Salama. "Optimal investment planning for distributed generation in a competitive electricity market". In: *IEEE Transactions on Power Systems* 19.3 (2004), pp. 1674–1684 (cit. on p. 75).

[59] Bernard Knueven, James Ostrowski, and Jean-Paul Watson. "On mixed-integer programming formulations for the unit commitment problem". In: *INFORMS Journal on Computing* 32.4 (2020), pp. 857–876 (cit. on p. 4).

[60] Petar Kokotović, Hassan K Khalil, and John O'reilly. *Singular perturbation methods in control: analysis and design*. SIAM, 1999 (cit. on pp. 47, 51, 52, 53, 57).

[61] Dmitry N Kosterev, Carson W Taylor, and William A Mittelstadt. "Model validation for the August 10, 1996 WSCC system outage". In: *IEEE Trans. on Power Systems* 14.3 (1999), pp. 967–979 (cit. on p. 59).

[62] Paul C Krause, Oleg Wasynczuk, Scott D Sudhoff, and Steven D Pekarek. *Analysis of electric machinery and drive systems*. John Wiley & Sons, 2013 (cit. on p. 66).

[63] Prabha S Kundur and Om P Malik. *Power system stability and control*. McGraw-Hill Education, 2022 (cit. on pp. 33, 46, 54).

[64] National Renewable Energy Laboratory. *3TIER. Development of regional wind resource and wind plant output datasets*. 2010 (cit. on p. 109).

[65] National Renewable Energy Laboratory. *System Advisor Model Version 2020.11.29*. 2022. URL: https://sam.nrel.gov (visited on 08/20/2022) (cit. on p. 109).

[66] National Renewable Energy Laboratory. *Western wind and solar integration study*. 2020. URL: https://www.nrel.gov/docs/fy10osti/47434.pdf (visited on 08/20/2022) (cit. on p. 109).

[67] Jose Daniel Lara, Jonathan T Lee, Duncan S Callaway, and Bri-Mathias Hodge. "Computational experiment design for operations model simulation". In: *Electric Power Systems Research* 189 (2020), p. 106680 (cit. on p. 25).

[68] Jose Daniel Lara et al. "Revisiting Power Systems Time-domain Simulation Methods and Models". In: *Submitted to IEEE Transactions on Power Systems* (2022), pp. 1–1 (cit. on pp. 8, 12).

[69] José Daniel Lara et al. "Powersystems. jl—a power system data management package for large scale modeling". In: *SoftwareX* 15 (2021), p. 100747 (cit. on pp. 31, 54).

[70] Jonathan T Lee, Rodrigo Henriquez-Auba, Bala Kameshwar Poolla, and Duncan S Callaway. "Pricing and Energy Trading in Peer-to-Peer Zero Marginal-Cost Microgrids". In: *IEEE Transactions on Smart Grid* 13.1 (2021), pp. 702–714 (cit. on p. 97).

[71] Woongsup Lee, Lin Xiang, Robert Schober, and Vincent WS Wong. "Direct electricity trading in smart grid: A coalitional game analysis". In: *IEEE Journal on Selected Areas in Communications* 32.7 (2014), pp. 1398–1411 (cit. on p. 75).

[72] Diego Ponce de Leon Barido et al. "Evidence and future scenarios of a low-carbon energy transition in Central America: a case study in Nicaragua". In: *Environmental Research Letters* 10.10 (2015), p. 104002 (cit. on p. 100).

[73] Yashen Lin et al. *Research roadmap on grid-forming inverters*. Tech. rep. National Renewable Energy Lab (NREL), Golden, CO, USA, 2020 (cit. on pp. 10, 17, 19, 20, 21, 22, 23).

[74] Yashen Lin et al. "Stability assessment of a system comprising a single machine and inverter with scalable ratings". In: *2017 North American Power Symposium (NAPS)*. IEEE. 2017, pp. 1–6 (cit. on pp. 12, 16, 45).

[75] Alvaro Lorca and Xu Andy Sun. "Adaptive robust optimization with dynamic uncertainty sets for multi-period economic dispatch under significant wind". In: *IEEE Transactions on Power Systems* 30.4 (2014), pp. 1702–1713 (cit. on p. 2).

[76] Yingbo Ma et al. *ModelingToolkit: A Composable Graph Transformation System For Equation-Based Modeling*. 2021. arXiv: 2103.05244 [cs.MS] (cit. on pp. 54, 59).

[77] Abdullah Mahmoudi, Seyed Hossein Hosseinian, Mojtaba Kosari, and Hassan Zarabadipour. "A new linear model for active loads in islanded inverter-based microgrids". In: *International Journal of Electrical Power & Energy Systems* 81 (2016), pp. 104–113 (cit. on p. 67).

[78] Uros Markovic et al. "Understanding small-signal stability of low-inertia systems". In: *IEEE Transactions on Power Systems* 36.5 (2021), pp. 3997–4017 (cit. on pp. 7, 44, 59, 61).

[79] Wieslaw Marszalek and Zdzislan W Trzaska. "Singularity-induced bifurcations in electrical power systems". In: *IEEE Trans. on Power Systems* 20.1 (2005), pp. 312–320 (cit. on pp. 65, 70).

[80] Gaëtan Masson and Mary Brunisholz. "Snapshot of global photovoltaic markets". In: *Report IEA PVPS T1–T292016* 1 (2015) (cit. on p. 73).

[81] Valérie Masson-Delmotte et al. "Climate change 2021: the physical science basis". In: *Contribution of working group I to the sixth assessment report of the intergovernmental panel on climate change* (2021), p. 2 (cit. on p. 1).

[82] Sara Matasci. *2018 Average Solar Panel Size and Weight | EnergySage*. Jan. 2018. URL: https://news.energysage.com/average-solar-panel-size-weight/ (cit. on p. 89).

[83] Esther Mengelkamp et al. "Designing microgrid energy markets: A case study: The Brooklyn Microgrid". In: *Applied Energy* 210 (2018) (cit. on p. 74).

[84] Federico Milano. "An open source power system analysis toolbox". In: *IEEE Transactions on Power systems* 20.3 (2005), pp. 1199–1206 (cit. on p. 26).

[85] Federico Milano. *Power system modelling and scripting*. Springer Science & Business Media, 2010 (cit. on pp. 48, 62).

[86] Federico Milano et al. "Foundations and challenges of low-inertia systems". In: *2018 power systems computation conference (PSCC)*. IEEE. 2018, pp. 1–25 (cit. on pp. 7, 41).

[87] Jovica V Milanovic et al. "International industry practice on power system load modeling". In: *IEEE Trans. on Power Systems* 28.3 (2012), pp. 3038–3046 (cit. on p. 59).

[88]   Daniel K. Molzahn, Ian A. Hiskens, et al. "A survey of relaxations and approximations of the power flow equations". In: *Foundations and Trends® in Electric Energy Systems* 4.1-2 (2019), pp. 1–221 (cit. on p. 4).

[89]   Wajid Muneer, Kankar Bhattacharya, and Claudio A Canizares. "Large-scale solar PV investment models, tools, and analysis: The Ontario case". In: *IEEE Transactions on Power Systems* 26.4 (2011), pp. 2547–2555 (cit. on p. 75).

[90]   Rossano Musca, Antony Vasile, and Gaetano Zizzo. "Grid-forming converters—A critical review of pilot projects and demonstrators". In: *Renewable and Sustainable Energy Reviews* 165 (2022), p. 112551 (cit. on p. 10).

[91]   Kashem M Muttaqi, An DT Le, Michael Negnevitsky, and Gerard Ledwich. "An algebraic approach for determination of DG parameters to support voltage profiles in radial distribution networks". In: *IEEE Transactions on Smart Grid* 5.3 (2014), pp. 1351–1360 (cit. on p. 75).

[92]   N.C. Clean Energy Technology Center. *Residential Renewable Energy Tax Credit*. Mar. 2018 (cit. on p. 73).

[93]   Engineering National Academies of Sciences, Medicine, et al. *The Future of Electric Power in the United States*. 2021 (cit. on p. 7).

[94]   National Conference of State Legislatures. *State Net Metering Policies*. Nov. 2017. URL: http://www.ncsl.org/research/energy/net-metering-policy-overview-and-state-legislative-updates.aspx (cit. on p. 73).

[95]   National Grid Electricity System Operator. *GC0137: Minimum Specification Required for Provision of GB Grid Forming Capability*. Tech. rep. National Grid Electricity System Operator (NGESO), London, GB, 2021 (cit. on pp. 18, 19, 20, 21).

[96]   Ashutosh Nayyar, Kameshwar Poolla, and Pravin Varaiya. "A statistically robust payment sharing mechanism for an aggregate of renewable energy producers". In: *Control Conference , 2013 European*. IEEE. 2013, pp. 3025–3031 (cit. on p. 75).

[97]   James Nelson et al. "High-resolution modeling of the western North American power system demonstrates low-cost and low-carbon futures". In: *Energy Policy* 43 (2012), pp. 436–447 (cit. on p. 100).

[98]   NERC. *1,200 MW Fault Induced Solar Photovoltaic Resource Interruption Disturbance Report*. Tech. rep. Version 1.1. June 2017 (cit. on p. 42).

[99]   NERC. *Grid Forming Technology Bulk Power System Reliability Considerations*. Tech. rep. North American Electric Reliability Corporation (NERC), Atlanta, GA, USA, 2021 (cit. on pp. 19, 20, 23).

[100] NERC. *Integrating Inverter-Based Resources into Low Short Circuit Strength Systems — Reliability Guideline*. Tech. rep. Dec. 2017 (cit. on p. 42).

[101] Alvaro Ortega and Federico Milano. "Comparison of different PLL implementations for frequency estimation and control". In: *2018 18th International Conference on Harmonics and Quality of Power (ICHQP)*. IEEE. 2018, pp. 1–6 (cit. on p. 13).

[102] Mario Paolone et al. "Fundamentals of power systems modelling in the presence of converter-interfaced generation". In: *Electric Power Systems Research* 189 (2020), p. 106811 (cit. on p. 7).

[103] Sangdon Park et al. "Contribution-based energy-trading mechanism in microgrids for future smart grid: A game theoretic approach". In: *IEEE Transactions on Industrial Electronics* 63.7 (2016), pp. 4255–4265 (cit. on p. 75).

[104] Pecan Street Inc. *Dataport*. https://www.dataport.cloud. 2019 (cit. on p. 89).

[105] Les Pereira et al. "An interim dynamic induction motor model for stability studies in the WSCC". In: *IEEE Trans. on Power Systems* 17.4 (2002), pp. 1108–1115 (cit. on p. 59).

[106] Stefan Pfenninger, Adam Hawkes, and James Keirstead. "Energy systems modeling for twenty-first century energy challenges". In: *Renewable and Sustainable Energy Reviews* 33 (2014), pp. 74–86 (cit. on p. 99).

[107] Salvador Pineda, Ricardo Fernández-Blanco, and Juan Miguel Morales. "Time-adaptive unit commitment". In: *IEEE Transactions on Power Systems* 34.5 (2019), pp. 3869–3878 (cit. on p. 2).

[108] Kris Poncelet et al. "Selecting representative days for capturing the implications of integrating intermittent renewables in generation expansion planning problems". In: *IEEE Transactions on Power Systems* 32.3 (2016), pp. 1936–1948 (cit. on p. 2).

[109] WW Price et al. "Load representation for dynamic performance analysis". In: *IEEE Trans. on Power Systems* 8.2 (1993) (cit. on p. 59).

[110] Christopher Rackauckas and Qing Nie. "Differentialequations.jl–a performant and feature-rich ecosystem for solving differential equations in julia". In: *Journal of Open Research Software* 5.1 (2017) (cit. on p. 36).

[111] Deepak Ramasubramanian et al. "Parameterization of generic positive sequence models to represent behavior of inverter based resources in low short circuit scenarios". In: *Electric Power Systems Research* 213 (2022), p. 108616 (cit. on p. 24).

[112] Narayan S Rau and Yih-heui Wan. "Optimum location of resources in distributed planning". In: *IEEE Transactions on Power systems* 9.4 (1994), pp. 2014–2020 (cit. on p. 75).

[113] J. Revels, M. Lubin, and T. Papamarkou. "Forward-Mode Automatic Differentiation in Julia". In: *arXiv:1607.07892 [cs.MS]* (2016). URL: https://arxiv.org/abs/1607.07892 (cit. on p. 36).

[114] Joan Rocabert, Alvaro Luna, Frede Blaabjerg, and Pedro Rodriguez. "Control of power converters in AC microgrids". In: *IEEE transactions on power electronics* 27.11 (2012), pp. 4734–4749 (cit. on pp. 9, 14).

[115] Roberto Rosso et al. "Grid-forming converters: control approaches, grid-synchronization, and future trends-A review". In: *IEEE Open Journal of Industry Applications* (2021) (cit. on pp. 9, 10, 11).

[116] Peter W Sauer, Mangalore A Pai, and Joe H Chow. *Power system dynamics and stability: with synchrophasor measurement and power system toolbox*. John Wiley & Sons, 2017 (cit. on p. 46).

[117] Peter W. Sauer, Said Ahmed-Zaid, and Petar V. Kokotovic. "An integral manifold approach to reduced order dynamic modeling of synchronous machines". In: *IEEE transactions on Power Systems* 3.1 (1988), pp. 17–23 (cit. on pp. 27, 46, 47, 57).

[118] Colin Sheppard et al. "Modeling plug-in electric vehicle charging demand with BEAM: the framework for behavior energy autonomy mobility". In: (2017). DOI: 10.2172/1398472. URL: https://www.osti.gov/biblio/1398472 (cit. on p. 110).

[119] S Solomon et al. "Climate change 2007: Synthesis Report. Contribution of Working Group I, II and III to the Fourth Assessment Report of the Intergovernmental Panel on Climate Change. Summary for Policymakers." In: *Climate change 2007: Synthesis Report. Contribution of Working Group I, II and III to the Fourth Assessment Report of the Intergovernmental Panel on Climate Change. Summary for Policymakers.* (2007) (cit. on p. 1).

[120] Tiago Sousa et al. "Peer-to-peer and community-based markets: A comprehensive review". In: *Renew. and Sustainable Energy Reviews* 104 (2019), pp. 367–378 (cit. on p. 74).

[121] Dominick V Spracklen et al. "Impacts of climate change from 2000 to 2050 on wildfire activity and carbonaceous aerosol concentrations in the western United States". In: *Journal of Geophysical Research: Atmospheres* 114.D20 (2009) (cit. on p. 1).

[122] *Switch Model: A modern platform for planning high-renewable power systems*. Aug. 2022. URL: https://github.com/switch-model/switch (visited on 08/20/2022) (cit. on p. 101).

[123] Josh A Taylor, Sairaj V Dhople, and Duncan S Callaway. "Power systems without fuel". In: *Renewable and Sustainable Energy Reviews* 57 (2016), pp. 1322–1336 (cit. on p. 1).

[124] Ali Tayyebi et al. "Grid-forming converters–inevitability, control strategies and challenges in future grids application". In: (2018) (cit. on p. 9).

[125] The Solar Foundation. *Solar Jobs Census*. Mar. 2018. URL: https://www.thesolar-foundation.org/national/ (cit. on p. 73).

[126] European Network of Transmission System Operators for Electricity. *High Penetration of Power Electronic Interfaced Power Sources and the Potential Contribution of Grid Forming Converters*. Tech. rep. European Network of Transmission System Operators for Electricity (ENTSO-E), Brussels, Belgium, 2020 (cit. on pp. 18, 19, 20, 21, 23).

[127] Wayes Tushar et al. "Peer-to-peer energy systems for connected communities: A review of recent advances and emerging challenges". In: *Applied Energy* 282 (2021), p. 116131 (cit. on p. 74).

[128] Wayes Tushar et al. "Peer-to-peer trading in electricity networks: An overview". In: *IEEE Transactions on Smart Grid* 11.4 (2020), pp. 3185–3200 (cit. on p. 74).

[129] Wayes Tushar et al. "Transforming Energy Networks via Peer-to-Peer Energy Trading: The Potential of Game-Theoretic Approaches". In: *IEEE Signal Processing Magazine* 35.4 (July 2018), pp. 90–111 (cit. on p. 75).

[130] U.S. Energy Information Administration (EIA). *Electric Power Monthly. Data for February 2022*. Feb. 2022. URL: https://www.eia.gov/electricity/monthly/ (cit. on p. 7).

[131] Andreas Ulbig, Theodor S Borsche, and Göran Andersson. "Impact of low rotational inertia on power system stability and operation". In: *IFAC Proceedings Volumes* 47.3 (2014), pp. 7290–7297 (cit. on pp. 3, 7, 41).

[132] Black & Veatch. *Cost and performance data for power generation technologies*. 2012. URL: https://refman.energytransitionmodel.com/publications/1921 (visited on 08/20/2022) (cit. on p. 109).

[133] D Venkatramanan et al. "Integrated System Models for Networks with Generators & Inverters". In: *arXiv preprint arXiv:2203.08253* (2022) (cit. on p. 10).

[134] D. Venkatramanan et al. *Grid-forming Inverter Technology Specifications: A Review of Research Reports & Roadmaps*. Tech. rep. UNIFI-2022-1. UNIFI Consortium, 2022 (cit. on p. 10).

[135] *Virtual Net Metering Policy Background and Tariff Summary Report*. Tech. rep. Center for Sustainable Energy, 2015 (cit. on p. 74).

[136] Petr Vorobev et al. "High-fidelity model order reduction for microgrids stability assessment". In: *IEEE Trans. on Power Systems* 33.1 (2017), pp. 874–887 (cit. on pp. 42, 55).

[137] Max Wei et al. *Building a Healthier and More Robust Future: 2050 Low-carbon Energy Scenarios for California: Final Project Report*. California Energy Commission, 2019 (cit. on pp. 108, 109, 110, 111, 112, 113).

[138] Tim Wheeler and Joachim Von Braun. "Climate change impacts on global food security". In: *Science* 341.6145 (2013), pp. 508–513 (cit. on p. 1).

[139] Amirnaser Yazdani and Reza Iravani. *Voltage-sourced converters in power systems: modeling, control, and applications*. John Wiley & Sons, 2010 (cit. on p. 15).

[140] Baosen Zhang, Ramesh Johari, and Ram Rajagopal. "Competition and coalition formation of renewable power producers". In: *IEEE Transactions on Power Systems* 30.3 (2015), pp. 1624–1632 (cit. on p. 75).

[141] Ray Daniel Zimmerman, Carlos Edmundo Murillo-Sánchez, and Robert John Thomas. "MATPOWER: Steady-state operations, planning, and analysis tools for power systems research and education". In: *IEEE Transactions on power systems* 26.1 (2010), pp. 12–19 (cit. on p. 25).